Louisiana State University
LSU Digital Commons

LSU Master's Theses | Graduate School

2016

Tropospheric Ozone Prediction with Land Cover Regression in Baton Rouge, Louisiana

Mallory Nance Thomas
Louisiana State University and Agricultural and Mechanical College, mtho121@lsu.edu

Follow this and additional works at: https://digitalcommons.lsu.edu/gradschool_theses

Part of the Social and Behavioral Sciences Commons

Recommended Citation

Thomas, Mallory Nance, "Tropospheric Ozone Prediction with Land Cover Regression in Baton Rouge, Louisiana" (2016). *LSU Master's Theses*. 794.
https://digitalcommons.lsu.edu/gradschool_theses/794

This Thesis is brought to you for free and open access by the Graduate School at LSU Digital Commons. It has been accepted for inclusion in LSU Master's Theses by an authorized graduate school editor of LSU Digital Commons. For more information, please contact gradetd@lsu.edu.

TROPOSPHERIC OZONE PREDICTION WITH LAND COVER REGRESSION IN BATON ROUGE, LOUISIANA

A Thesis

Submitted to the Graduate Faculty of the
Louisiana State University and
Agricultural and Mechanical College
in partial fulfillment of the
requirements for the degree of
Master of Science

in

The Department of Geography and Anthropology

by
Mallory Nance Thomas
B.S., Louisiana State University, 2013
May 2016

Table of Contents

List of Tables

List of Figures

Abstract

Ground level ozone (O_3) is a pollutant of great public health concern. Spatial interpolation techniques provide powerful tools in estimating O_3 exposure, but many fall short when predicting O_3 on complex surfaces, especially given the high local variability typically associated with O_3 data. Like most other locations, the Baton Rouge, Louisiana, O_3 non-attainment zone (BRNZ) is plagued by a sparse density of O_3 monitoring stations. This research explores land use regression (LUR) as an alternative spatial prediction method in and around the BRNZ. Multiple years of data are used to partially compensate for the small sample of spatial points. To better associate O_3 measurements with the localized land cover, deviations-from-the-regional mean (devRM) are utilized rather than direct observations (DO).

Land cover data used did not perform well in predicting the daily maximum O_3 but performed moderately well for longer averaging periods. A model using the monthly mean O_3 maxima averaged over a three-year period was able to explain 42.04% of the variance in devRM data. Predicted devRM using this model accounts for 4.55% of the variance in DO, the regional mean accounts for 88.65% of the variance, and when summed, the regional mean and modeled devRM account for 93.50% of variance in DO O_3 data. These results are useful for future refinement of LUR models and will be useful to environmental planners and epidemiologists as they evaluate and mitigate the effects of O_3 in Louisiana.

Chapter 1. Introduction

Tropospheric ozone (O_3) is a triatomic oxygen molecule with detrimental oxidizing effects on living tissues and human-made materials. This pollutant is also characteristic of photochemical smog, a mixture of gases and particulate matter, all of which have health implications. Because of its potential for harm, the United States Environmental Protection Agency (USEPA) identifies O_3 as a criteria air pollutant. Networks of air sampling stations monitor mixing ratios of O_3, along with lead (Pb), particulate matter (PM), carbon monoxide (CO), nitrogen oxides (NO_x), and sulfur dioxide (SO_2). Measurements taken at these stations are used to determine whether an area is in attainment of National Ambient Air Quality Standards (NAAQS), and subsequently whether or not an area is subject to sanctions, including loss of funding from the Federal Highway Administration, caps on industrial growth, and the requirements for the sale of cleaner gasoline. As of July 2014, 227 U.S. counties aggregated in 46 nonattainment areas experienced O_3 pollution above the current 8-hr mean design value of 75 ppb, exposing approximately 123 million people to potentially hazardous amounts of O_3. For all of these reasons, it is important to monitor O_3 mixing ratios.

To assess exposure of different populations and characterize the spatial distribution of O_3 more accurately, high-resolution maps of O_3 pollution are required. Maps are an information prerequisite for epidemiologists to link air pollution to human health and for public health officials to develop health risk assessments. Spatial characterization of pollutant concentrations may assist in establishing and evaluating air quality policies and in assessing impacts of land-use and the urban metabolism on air quality sustainability.

Chapter 2. Background and Research Questions

2.1 O_3 Exposure

Clinical studies and animal autopsies have confirmed that O_3 exposure induces adverse structural, functional, and biochemical alterations to biological tissues. Flecking, stippling, bronzing, and reddening on plant leaves are classical exposure responses of crops and forests that uptake O_3 via stomatal gas exchange (Krupa and Manning 1988, Feng et al. 2014). Inhalation of O_3 by humans can produce immediate breathing problems such as wheezing and coughing, asthma attacks, increased risks of respiratory infections and pulmonary inflammation, and increased hospital admissions for people with existing lung diseases (e.g. asthma, chronic pulmonary disease (Beckett 1991). O_3 exposure can damage the ocular surface (Lee et al. 2013) and increase the risk of a perforated appendix (Kaplan et al. 2013). In a review of O_3 research published between 2006 and 2012, the USEPA (2013) concluded that O_3 exposure is likely to cause cardiovascular harm (e.g. heart attacks, strokes, heart disease, congestive heart failure), damage to the central nervous system, reproductive and developmental harm, and early death. Children and the elderly are identified as sensitive populations.

From lost crop yields (Krupa and Manning 1988, Fuhrer et al. 1997, Avnery et al. 2011) to lost worker productivity (Zivin and Neidell 2013), O_3 pollution is costly. School absenteeism from O_3-induced illnesses (Romieu et al. 1992, Gilliland et al. 2001) has an annual cost of $245 million in the South Coast Air Basin of California (Hall et al. 2003). Elsewhere, a school may lose as much as $50 per unexcused absence (Currie et al. 2009). These figures are predicted to increase because of worsening O_3 from climatic change despite successful efforts to mitigate precursors (Lei et al. 2012). By 2020, O_3 increases could result in 2.8 million additional serious respiratory illnesses, 5,100 additional infants and seniors hospitalized with serious breathing problems, and 944,000 additional missed school days in the U.S. (Perara and Sanford 2011). These and other health-related impacts could cost approximately $5.4 billion (Perara and Sanford 2011).

2.2 Tropospheric O_3 Chemistry

To understand more about spatial variability in O_3 mixing ratios, it is pertinent here to review the chemical formation of O_3 from precursor pollutants, albeit simplistically. O_3 forms via photochemical reactions of precursor pollutants, primarily nitrogen oxides (NO_x = $NO + NO_2$) and volatile organic compounds (VOCs); this classifies it as a secondary pollutant. Primary pollutants are emitted directly, while chemical reactions of primary pollutants produce secondary pollutants.

O_3 production involves complicated series of non-linear photochemical transformations, but begins with the photolysis of nitrogen dioxide (NO_2) into nitrogen oxide (NO) and atomic oxygen (O):

$$NO_2 + UV \rightarrow NO + O$$

$$O + O_2 \rightarrow O_3$$

The O atom reacts with atmospheric oxygen (O_2) to form O_3. The unstable O_3 molecule rapidly reverts to the more stable O_2 yielding NO_2 and O_2.

$$NO + O_3 \rightarrow NO_2 + O_2$$

The two processes taken together result in no net production of O_3. The presence of VOCs and excess NO complicate the process because O_3 production depends on the NO_x-VOC ratio. NO_x loading events may be small scale and short-lived, such as vehicular emissions from rush hour traffic, or it may have a regional effect such as a freshly emitted plume of NO from a power plant scavenging and acting as an O_3 sink within 80 km of the source (Sillman 1999). Beyond being a source of O atoms for O_3 production, VOCs can disrupt the NO_x-O_3 exchange by reacting with NO, and orphaning O atoms that go on to produce O_3 rather than NO_2:

$$VOC + NO \rightarrow NO_2 + \text{other products}$$

Anthropogenic contributions of NO_x and VOCs alter the efficiency of O_3 production by augmenting natural emissions of precursor pollutants. Fossil fuel combustion, such as that used to power vehicles and generate electricity, emits NO_x. For the entire U.S., as of 2011, NO_x emissions from transportation accounted for 57.48% of NO_x emissions, while electric utilities and industrial processes were responsible for 13.09% and 8.41%, respectively. VOCs originate from an array of sources; however, biogenic emissions far surpass anthropogenic emissions, and highly reactive VOCs such as isoprene are emitted in large quantities by biogenic sources (Wagner and Kuttler 2014). According to the National Emissions Inventory (2011), biogenic sources accounted for 68.65% of all VOC emissions in the United States. Vegetation, especially evergreen forests and citrus groves, is the largest source of biogenic VOCs, in the form of isoprene. Anthropogenic sources of VOCs include fossil fuel combustion, direct evaporation of fuel and solvents, and chemical manufacturing.

2.3 Changing Surface O_3 Behavior

Surface cover properties influence temperature, dispersion efficiency, and ratios of precursor emissions, all of which govern O_3 formation and concentration in an air mass. Changes in the surface energy balance induced by urbanization illustrate the interaction of the land cover (LC) on atmospheric quality in the planetary boundary layer. Supplantation of vegetative material with non-transpiring impervious material such as concrete and asphalt in urbanized areas skews the partitioning of incoming solar radiation in favor of sensible heat over latent heat, increasing surface temperatures and air temperatures to create a microclimate (e.g. urban heat island). Warm air temperatures energize photochemical reactions and can create steep pressure gradients as the rising warm air lowers surface atmospheric pressure.

Urban centers and rural landscapes typically represent two different O_3 regimes because of the emission properties associated with different LCs. Net O_3 production depends on the ratio of NO_x and VOCs, and is suppressed when either is present in large enough excess relative to the other (Sillman 1999). VOC-sensitivity refers to the situation in which NO_x-related O_3 production is at a maximum, and a lack of VOCs limits further production. In a VOC-sensitive regime, where NO_x-related O_3 production has reached a maximum, the addition of more NO may destroy O_3 via NO-titration.

$$NO + O_3 \rightarrow NO_2 + O_2$$

Urban centers typically exhibit VOC-sensitivity, where NO_x-related O_3 production is at a maximum, and a lack of VOCs limits further production. This is due in part to characteristically high densities of NO_x-releasing activities (e.g. vehicular traffic, power generation, and manufacturing) and the relative paucity of vegetation. By contrast, NO_x-sensitivity is characteristic of rural areas, where the relative paucity of industrial and transportation activity reduces NO_x loadings. This is especially true in forested areas, where trees contribute largely to increasing biogenic VOC load relative to the NO_x load. Emissions of isoprene and monoterpenes from trees – two highly reactive VOCs – are considered highly important with respect to tropospheric photochemistry and O_3 formation (Guenther 1997, Isebrands et al. 1999, Staudt and Kesselmeier 1999), particularly in rural areas. In such situations, VOC-related O_3 production is stalled because of a lack of NO_x. Chemistry inside an air mass moving away from an urban area evolves from VOC-sensitive conditions to NO_x-sensitive conditions. In this manner, urban centers as sources of NO_x can influence regional O_3 concentrations. Sillman (1999) generalizes, ". . .NO_x emissions from within an urban area determine the total amount of ozone that is formed after the air moves downwind and chemistry has run to completion, while VOC emissions control the rate of initial build-up of O_3." Photochemical aging, meteorological processes, and fresh emissions add spatial heterogeneity to this downtown-to-downwind pattern.

2.4 Spatial Interpolation Techniques

Frequently, the spatial sampling distribution for air quality data, especially for long-term data, is limited by the density and spatial configuration of the routine monitoring network. The sites for these stations, chosen for regulatory compliance, are often sparse and unevenly distributed. Linear extrapolation from these sites to the surrounding region masks much of the variability and creates artificial breaks in the surface. Several spatial interpolation techniques have been developed, and each have advantages and disadvantages.

Inverse distance weighting (IDW), a deterministic spatial interpolation technique, assigns values at an unknown point as a weighted average of observed points. Weights are an inverse function of distance from the point of interest. The inherent assumptions of IDW introduce two important weaknesses: (1) clustering of sample points biases an interpolation, 'pulling' the surface toward the cluster, and (2) spatial non-stationarity, or uncontrolled variance, is problematic.

Kriging, the most common geostatistical technique used in the air pollution field (Jerrett et al. 2005), addresses both of these concerns. Originally developed by Georges Matheron for application in geologic mining, kriging has since evolved into a suite of techniques utilized by an array of fields including water resources, environmental sciences, agriculture and soil sciences, ecology, and limnology (Li and Heap 2011). Like all other spatial interpolation methods, kriging is based on the first law of geography (Tobler 1970), which states that phenomena that are geographically nearer to one another are more alike than those that are farther apart. All kriging techniques exploit spatial dependence in data to develop continuous surfaces and operate by estimating three components of variation: a broad-scale trend (or drift), local spatially-structured variation, and random variation. Like IDW, kriging is a weighted average technique. While IDW uses only distance between sampled points, kriging measures distances and direction between all possible pairs of observed points and uses these values to compute variability and probability. When interpolating using a kriging method, an estimation variance data set is produced along with the interpolated data set, allowing for the generation of a best-fit surface and an error surface.

The basic kriging model is as follows:

$$Z(\mathbf{s}) = \mu(\mathbf{s}) + \varepsilon(\mathbf{s}),$$

where $Z(\mathbf{s})$ is the target variable, decomposed into a deterministic trend $\mu(\mathbf{s})$ and random, spatially autocorrelated errors $\varepsilon(\mathbf{s})$. Ordinary kriging (OK) uses a stationary trend, that is $\mu(\mathbf{s}) = m$. This is an acceptable condition when the phenomenon of interest exists in a uniform space or under uniform processes, which is rarely the case. To account for a trend (a non-uniform space) in the data, universal kriging (UK) models the trend as a linear function of point coordinates. Kriging with an external drift (KED) is the same procedure but models the trend as linear function of exogenous variables. Both procedures extend the covariance matrix and simultaneously fit the deterministic and stochastic components of the basic kriging model (Hengl et al. 2003).

Regression-kriging (RK) fits the deterministic component ($\mu(\mathbf{s})$) separately from the stochastic component. RK has been called residual kriging (Alsamamra et al. 2009), kriging with a guess field (Ahmed and De Marsily 1987), simple kriging with varying local means (Goovaerts 1997), and kriging after detrending (Goovaerts 1999). RK allows for more complex regression analysis, rather than simple linear regressions used in KED, and it allows the separate interpretations of two estimated components: the global parameter estimates from regression and the local relationships incorporated through the covariance structure of the residuals (Fotheringham and Brunsdon 1999, Hengl et al. 2007).

IDW and OK are among the most frequently used interpolation techniques in environmental sciences (Li and Heap 2011), but depending on the size and distribution of the sampled dataset, distance-based interpolation and kriging may "over-smooth" a surface and fail to capture spatial heterogeneity. Hybrid interpolation techniques such as RK that combine regression with geostatistical interpolation (Knotters et al. 1995, Hengl et al. 2007) potentially rectify the smoothing of short-range variation, creating better agreement between estimated and actual values, and decreasing misclassification of sampled locations (Goovaerts 1997).

2.5 Predictive Mapping with Land Use Regression

Land use regression (LUR) is the pure regression form of RK. LUR models $\mu(\mathbf{s})$ by constructing multiple regression equations describing the relationship between environmental variables, such as LC, population density, and road networks as independent variables, and monitored pollutant concentrations as the dependent variable. If the residuals ($\varepsilon(\mathbf{s})$) produced by the regression are spatially autocorrelated, kriging can be performed. If the $\varepsilon(\mathbf{s})$ are not spatially autocorrelated, no kriging is performed. Briggs et al. (1997) calls this technique regression mapping, and as Hoek et al. (2008) acknowledges, the term is more descriptive of the methodology because variables other than land use are included in the models. However, the term LUR is most prevalent in the literature and will be used subsequently herein.

LUR is based on the principle that the dependent variable (pollutant concentrations, in this case) at any location depends on the environmental characteristics of the surrounding environment, particularly those that influence or are influenced by emission intensity and dispersion efficiency. For example, excessive O_3 mixing ratios might be expected to be predicted spatially by considering the distribution of built-up LCs (which are linked with higher NO_x concentrations), forests (which may emit VOCs but very little NO_x), and water bodies (which would support little NO_x or VOC production).

LUR models have been applied to numerous air quality studies in the United Kingdom (Briggs et al. 1997, Briggs et al. 2000, Gulliver et al. 2011), Germany (Morgenstern et al. 2007), the Netherlands (Beelen et al. 2007), Italy (Rosenlund et al. 2008), and Spain (Aguilera et al. 2013), among other European locations. In Canada, LUR models have been applied to map NO_2 in Toronto (Kanaroglou et al. 2005, Jerrett et al. 2007), Montreal (Gilbert et al. 2005), and Vancouver (Henderson et al. 2007). Large U.S. metropolitan areas such as New York City (Ross et al. 2007) and Los Angeles (Moore et al. 2007) have made use of routine monitoring stations to develop LUR models for assessing the spatial distribution of particulate matter exposure.

LUR studies frequently collect and assess a large number of potential predictor variables, or variations of the predictor variables, but retain only a few in the final model. To build a LUR model for predicting ambient concentrations of NO_2 in Ontario, Sahsuvaroglu et al. (2006) tested more than 110 variables. Only seven were found to contribute significantly to the prediction. The more than 110 variables tested could be grouped into five categories: land use, physical geography, meteorology, roads and traffic, and population.

Retained predictors often represent population, road traffic, and land use/land cover (LU/LC); however, they are defined in different ways primarily because of data availability. As part of the Small Area Variations In Air quality and Health (SAVIAH) study, Briggs et al. (1997) developed unique LUR models for three European cities: Amsterdam, Huddersfield (UK), and Prague. Traffic volume was found to be a significant predictor of NO_2 in Huddersfield and Prague, but in Amsterdam, where traffic count data were unavailable, length of major roads was used as a traffic indicator (Briggs et al. 1997). Population count (Beelen et al. 2007), housing density (Morgenstern et al. 2007), and population density (Gilbert et al. 2005) have been used to represent population. LULC has been defined as the area of built-up land (Briggs et al. 1997), industrial land use and open space use (Sahsuvaroglu et al. 2006), and urban LC (Beelen et al. 2007).

2.6 Tropospheric O_3 in Baton Rouge

Baton Rouge, Louisiana (30º27'29"N, 91º8'25"W), is an area that historically has struggled to comply with the O_3 NAAQS of a daily maximum 8-hour rolling average concentration of 75 ppb, indicating a persistent O_3 problem. The NAAQS is established by the USEPA under the authority of the Clean Air Act (CAA), and is subject to revision in consideration of new research. An area not meeting the NAAQS is deemed a nonattainment area and is classified as marginal, moderate, serious, or severe.

At the time of 1990 Clean Air Act Amendments (CAAA), the NAAQS for O_3 was a daily maximum one-hourly average concentration of 120 parts per billion (ppb). In recognition that prolonged exposure to O_3 can have more severe health consequences than short-term exposure even at higher mixing ratios, the O_3 standard was revised in 1997 from the maximum 1-hour concentration-based standard (120 ppb) to a daily maximum 8-hour rolling average concentration of 80 ppb. In 2008, the standard was again revised to an 8-hour rolling average concentration of 75 ppb, despite evidence suggesting that an even lower design value would be necessary to protect life and property effectively.

In the early 1990s, the Baton Rouge area was classified as having a "serious" O_3 problem following the 1990 CAAA criteria. By April 2014, USEPA determined the Baton Rouge area to be in attainment of the 2008 8-hour O_3 NAAQS based on air quality data obtained by ten monitoring stations from 2011 to 2013. USEPA scientific advisors continue to advocate for a stricter standard somewhere in the range of 60 ppb to 70 ppb. Adoption of a stricter standard would once again put the Baton Rouge area into nonattainment because two of the ten stations monitoring O_3 in the Baton Rouge metropolitan area have design-values at 75 ppb.

2.7 Research Questions

Given the severe consequences of excessive O_3 exposure and the shortcomings of conventional interpolation methods to produce a spatially-resolved surface with only sparse data points, a regression-based approach is tested. Two questions are posed:

1) Which, if any, LC types are correlated with the O_3 mixing ratios?

Given that NO_x and VOC emissions are associated with different LC types, correlation analysis of the proportions of different land types within buffers of varying radii will provide information regarding the strength and direction of correlation with O_3 response variables.

2) Can LC be used to improve (downscale) spatial predictions of O_3 mixing ratios?

Multivariate regression models informed by the results of correlation analysis will be evaluated. Residuals produced by the final models will be tested for spatial relationships and the appropriate combinations of regression and interpolation techniques will be applied to produce a prediction surface.

Chapter 3. Data and Methods

3.1 Study Area

The study area boundaries match those of the Louisiana Department of Environmental Quality (LDEQ) Capital Region. This area includes the five-parish Baton Rouge non-attainment zone (BRNZ), comprised of Ascension, East Baton Rouge (EBR), Iberville, Livingston, and West Baton Rouge (WBR) parishes (Figure 3.1). The population of the BRNZ is approximately 732,607 as of 2010, or about 16.16 percent of the population of Louisiana (United States Census Bureau 2010) . The heavy dependence on the automobile along with a dense network of industrial plants along the Mississippi River corridor contributes to the NO_x precursor.

3.2 Data

3.2.1 Land Cover

Classified Landsat imagery obtained from the National Land Cover Database (NLCD) was used to generate the field of candidate potential predictors in model development. The Multi-Resolution Land Characteristics Consortium (MRLC), a collaboration of federal agencies including the United States Forest Service (USFS), National Oceanic and Atmospheric Administration (NOAA), and USEPA, maintains the NLCD (Homer et al. 2007, Fry et al. 2011, Homer et al. 2015). NLCD products provide consistent, nationwide LC information at a 30 m resolution for scientific, economic, and governmental applications. The first NLCD product (NLCD 1992) is based primarily on the unsupervised classification of Landsat Thematic Mapper (TM) imagery. Subsequent editions (NLCD 2001, NLCD 2006, NLCD 2011) use a decision-tree algorithm to classify Landsat imagery following a 16-class scheme (Table 3.1). Figure 3.2 displays NLCD 2011 within and near the study area.

Figure 3.1 Study area including the five-parish BRNZ.

Table 3.1 Land cover classes and assigned codes.

Value	Class	Code	Value	Class	Code
11	Open water	WA	42	Evergreen forest	EV
12	Perennial ice/snow**	--	43	Mixed forest	MI
21	Developed, open space	OS	52	Shrub/scrub	SH
22	Developed, low intensity	LO	71	Grassland/herbaceous	HE
23	Developed, medium intensity	ME	81	Hay/pasture	HA
24	Developed, high intensity	HI	82	Cultivated crops	CR
31	Barren land (rock/sand/clay)	BA	90	Woody wetlands	WW
41	Deciduous forest	DE	95	Emergent herbaceous wetlands	EH

**Perennial ice/snow does not appear in study area.

The stations represent a variety of local environments. Figures 3.3 through 3.12 show the distribution of LC classes in a 2000 m buffer around each of the ten stations used in this study. Some stations are dominated by a single LC type, with the abbreviations in the discussion below denoted in Table 3.1. Woody wetlands (WW) comprises 83.24% of the 2000 m buffer surrounding the Bayou Plaquemine monitor (Figure 3.3). Two sites — Capitol (Figure 3.4) and LSU (Figure 3.9) are largely developed, either in the low (LO), medium (ME), or high (HI) intensity category. French Settlement is also largely WW (Figure 3.8). Other stations indicate a more agricultural setting with high percentages of developed — open space (OS) and LO combined with hay/pasture (HA) and cultivated crops (CR).

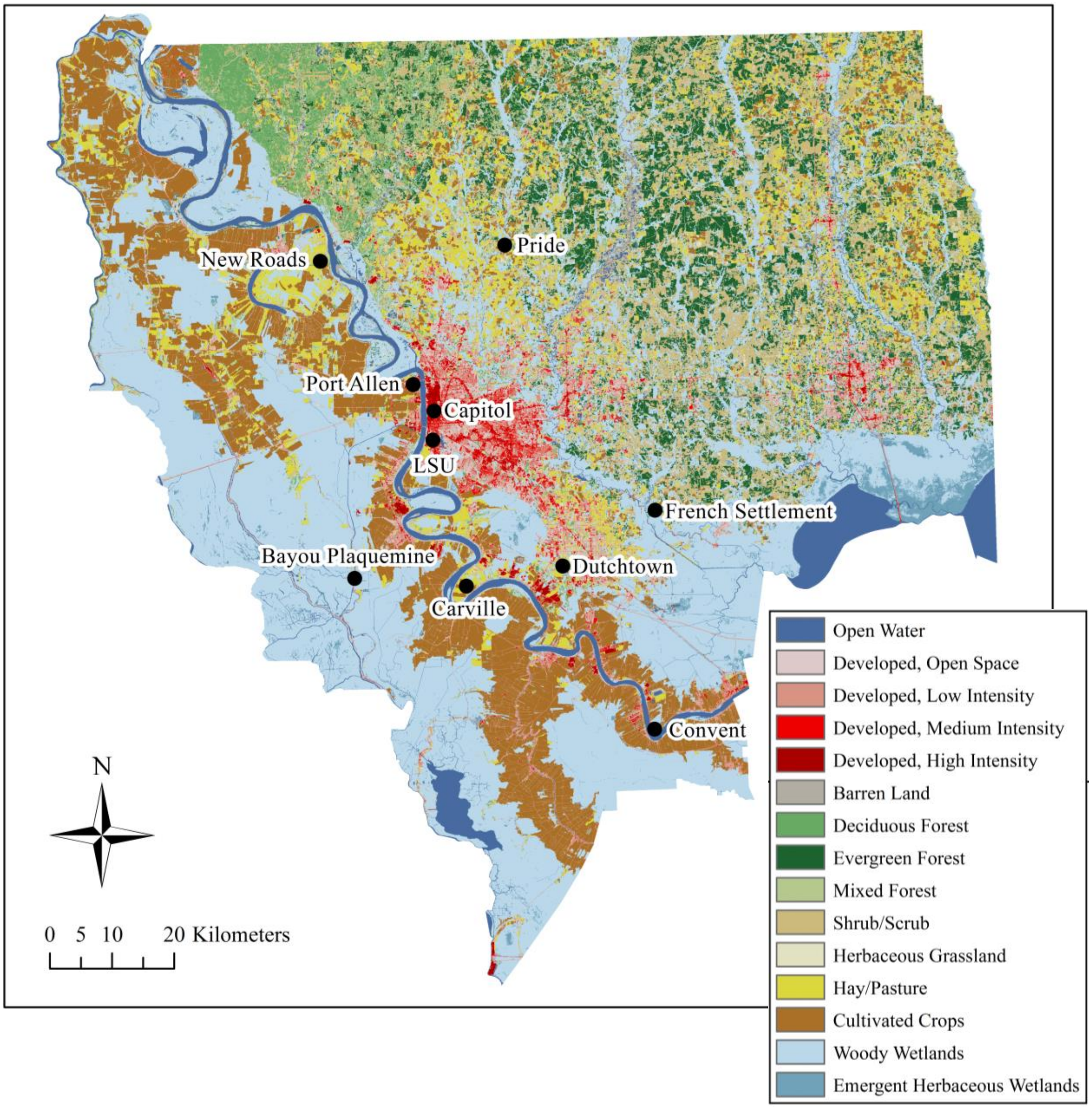

Figure 3.2 Distribution of NLCD 2011 classified land cover in and near the study area.

3.2.2 Ozone

Daily maximum 8-h mean O_3 mixing ratios recorded by ten air quality monitoring stations (Figure 3.1; Table 3.2) operating within or near the study area were collected from the USEPA for the years 2000–2002, 2005–2007, and 2010–2012. Convent and New Roads are used in this study along with the eight monitoring stations within the BRNZ. The three-year windows are centered on NLCD edition years.

The network of air quality monitoring station in the Baton Rouge area is known as a state and local air monitoring (SLAMS) network. SLAMS are used to determine concentrations maximum, background, and typical concentrations in an area; the impact of significant pollutant sources and source categories on ambient pollution level; the extent of pollutant transport; and the welfare impacts of air pollution. Included in the SLAMS are photochemical assessment monitoring stations (PAMS) used by the EPA to provide data for photochemical models. The placement of monitors in a PAMS network is informed by wind direction and locations of precursor emission sources. PAMS stations are given type classifications. Based on the predominant morning wind, a Type 1 site is placed upwind of the local area of maximum precursor emissions. Type 3 sites are typically located 10 to 30 miles from the fringe of an urban area, and are intended to monitor ozone concentrations occurring downwind of areas with large precursor emissions. A site may be dually classified as a Type 1 and Type 3, depending on wind conditions. Bayou Plaquemine, Pride, and Dutchtown are Type 1/Type 3 sites. Capitol and LSU are Type 2 sites. These sites are located downwind of the area with maximum precursor emissions and near the boundary of central business district. Carville, Convent, French Settlement, New Roads, and Port Allen do not have PAMS designations; these sites are in the SLAMS network.

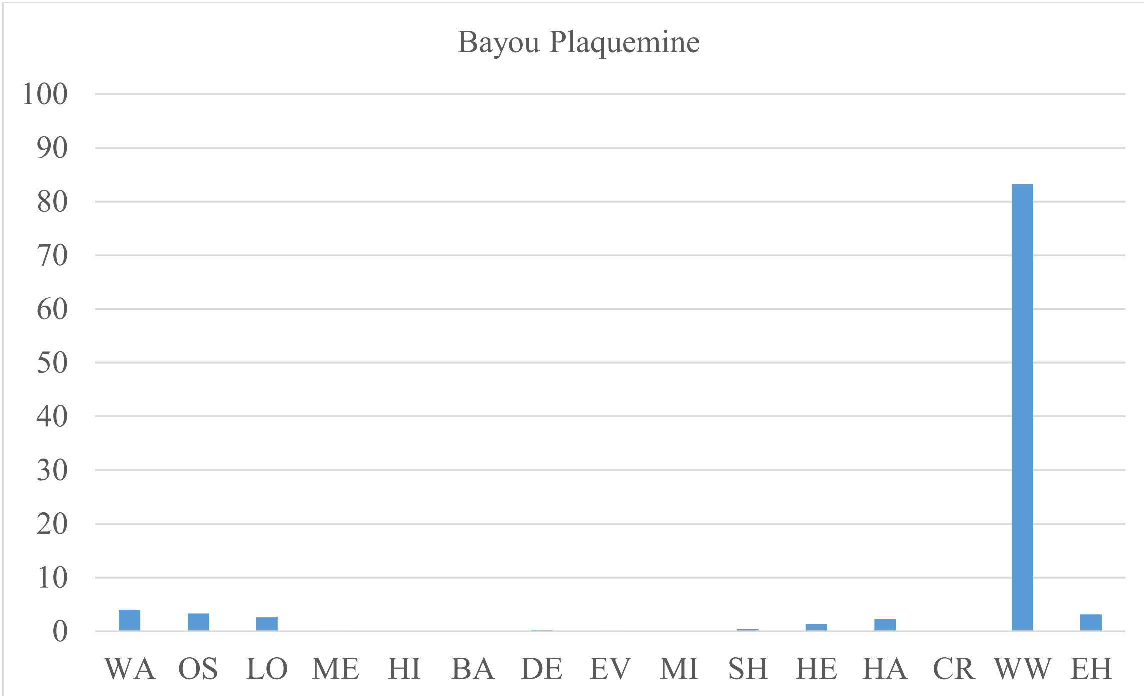

Figure 3.3 Percentages of NLCD classes within a 2000 m buffer around the Bayou Plaquemine air quality monitor in the BRNZ.

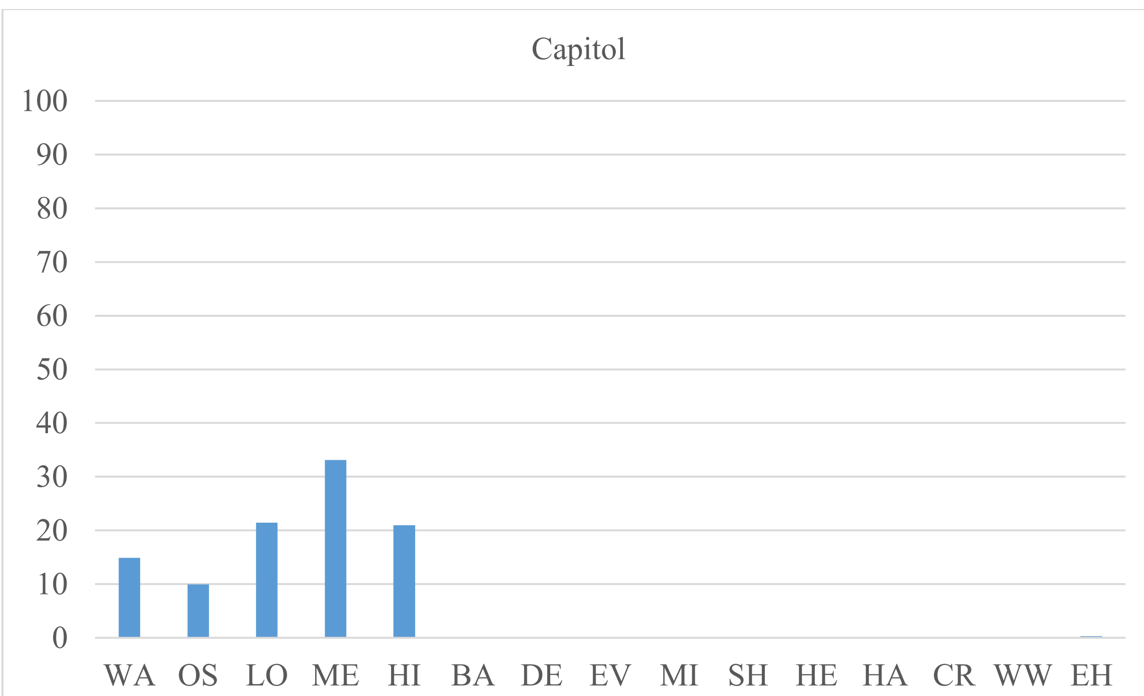

Figure 3.4 Percentages of NLCD classes within a 2000 m buffer around the Capitol air quality monitor in the BRNZ.

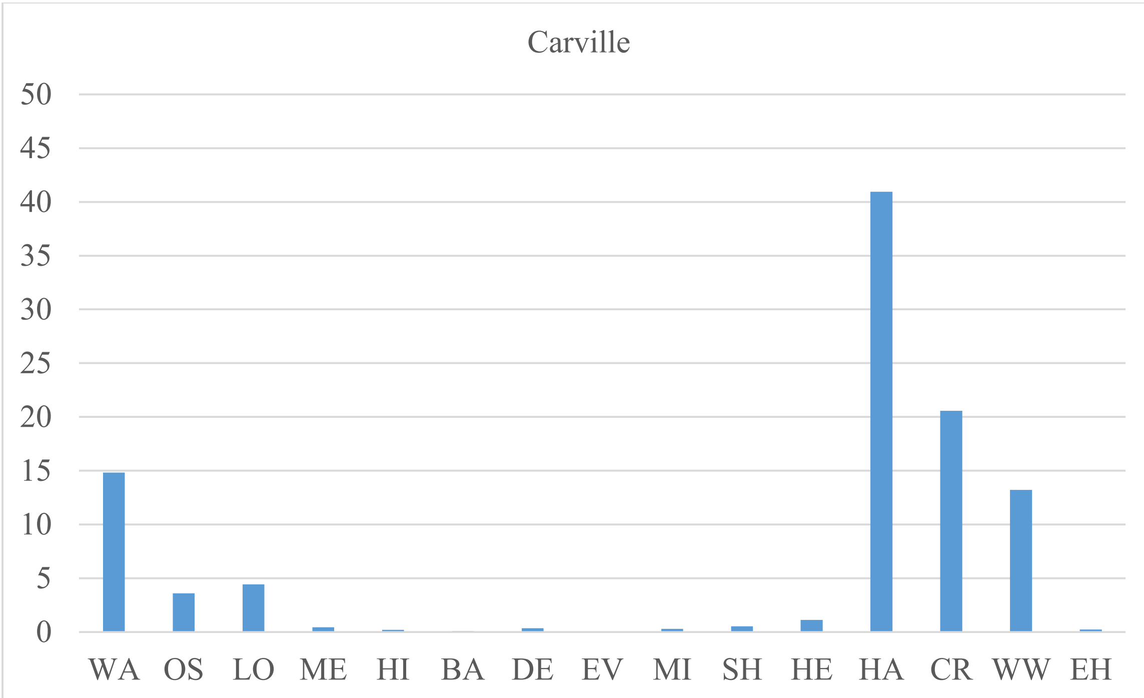

Figure 3.5 Percentages of NLCD classes within a 2000 m buffer around the Carville air quality monitor in the BRNZ.

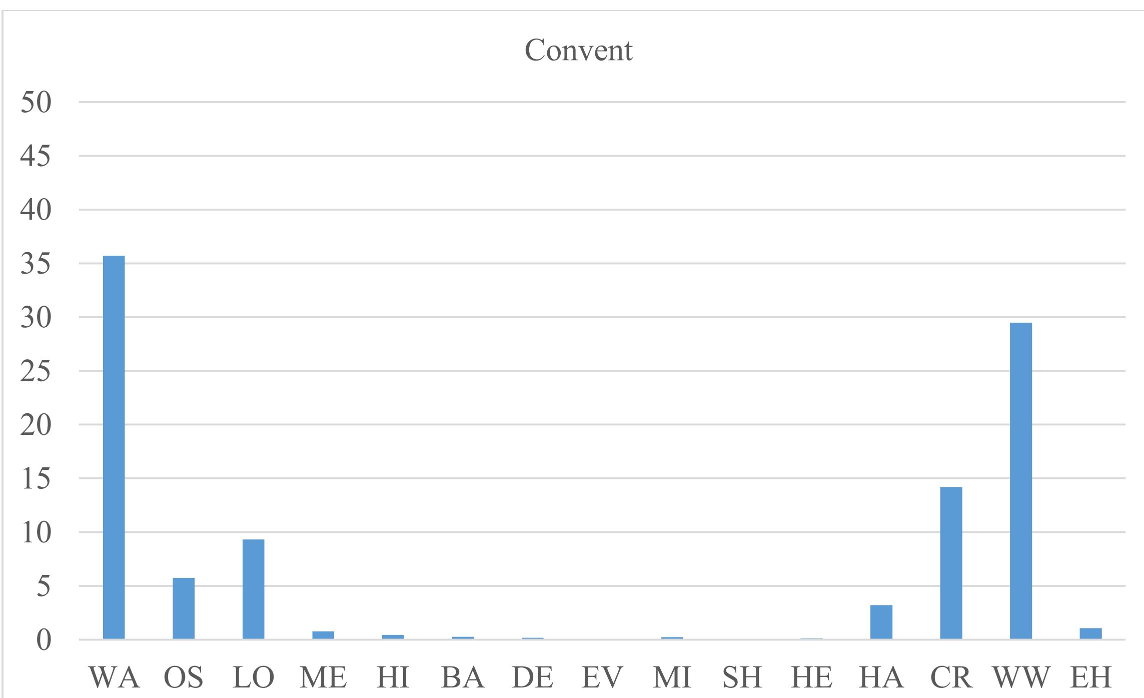

Figure 3.6 Percentages of NLCD classes within a 2000 m buffer around the Convent air quality monitor near the BRNZ.

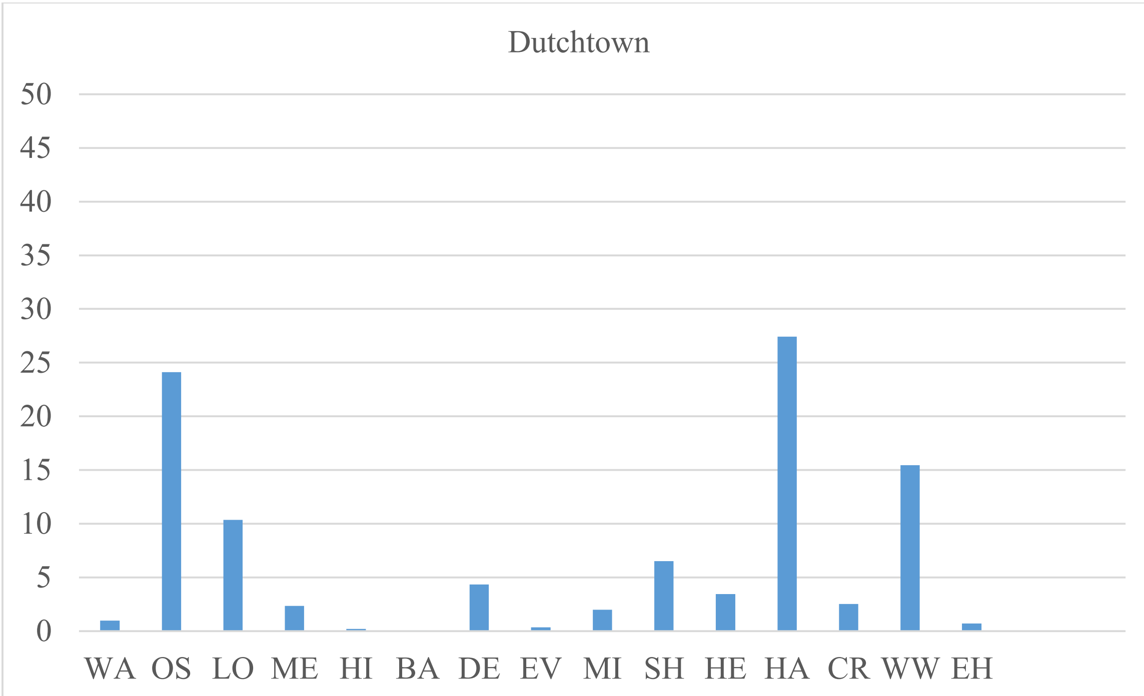

Figure 3.7 Percentages of NLCD classes within a 2000 m buffer around the Dutchtown air quality monitor in the BRNZ.

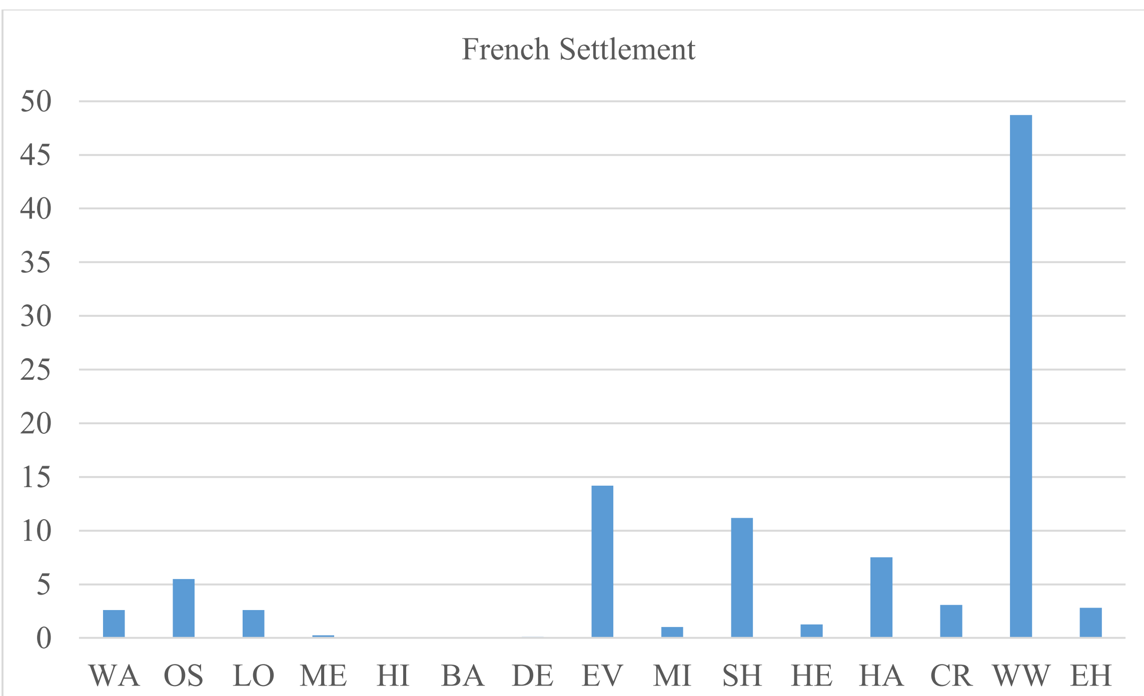

Figure 3.8 Percentages of NLCD classes within a 2000 m buffer around the French Settlement air quality monitor in the BRNZ.

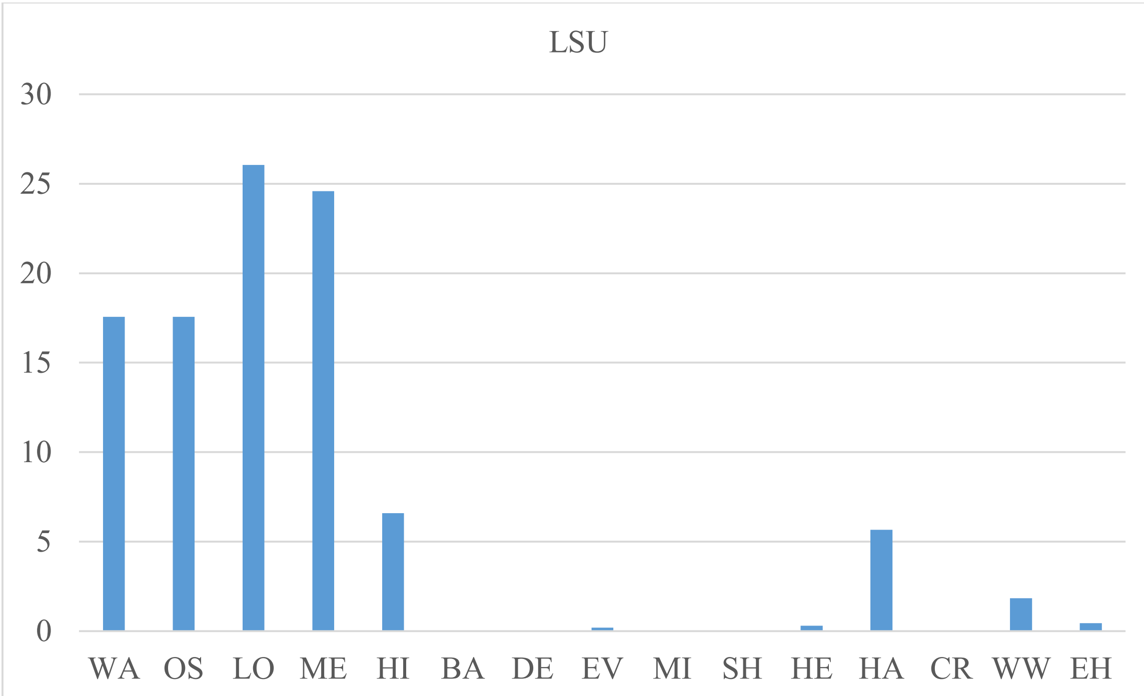

Figure 3.9 Percentages of NLCD classes within a 2000 m buffer around the LSU air quality monitor in the BRNZ.

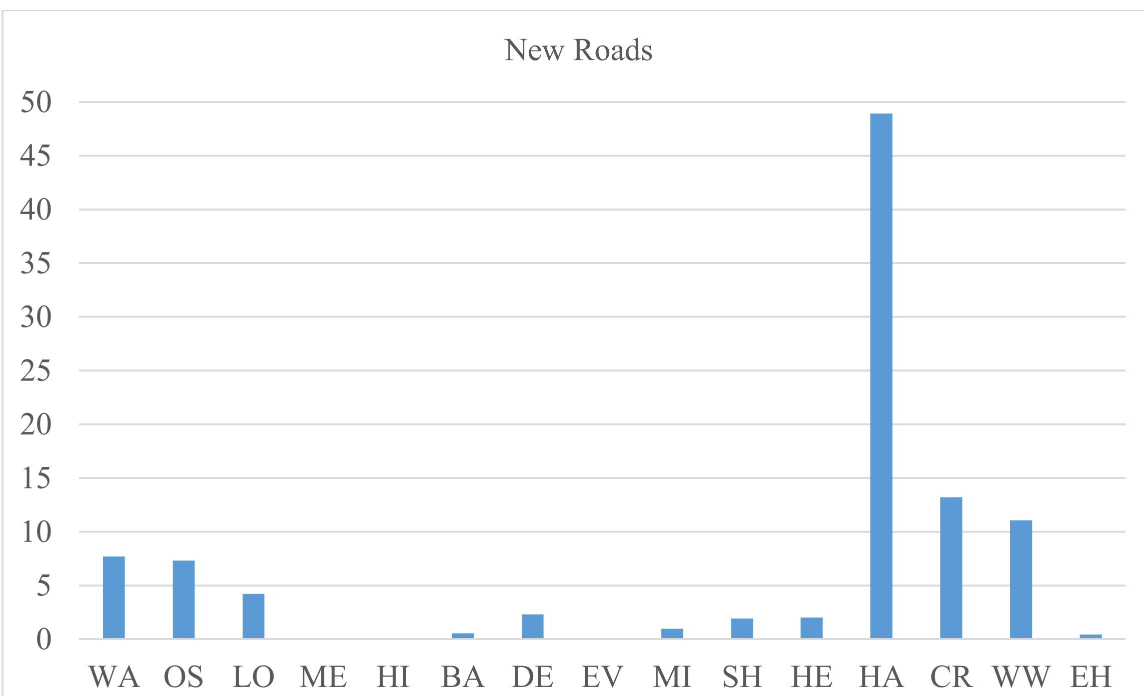

Figure 3.10 Percentages of NLCD classes within a 2000 m buffer around the New Roads air quality monitor near the BRNZ.

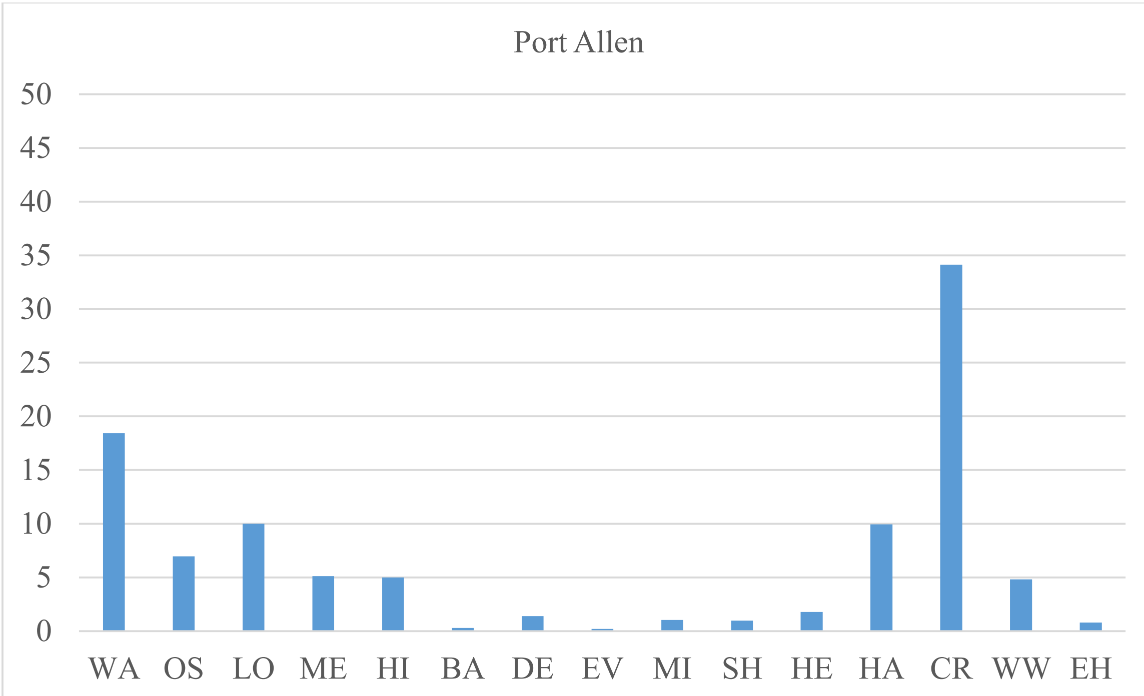

Figure 3.11 Percentages of NLCD classes within a 2000 m buffer around the Port Allen air quality monitor in the BRNZ.

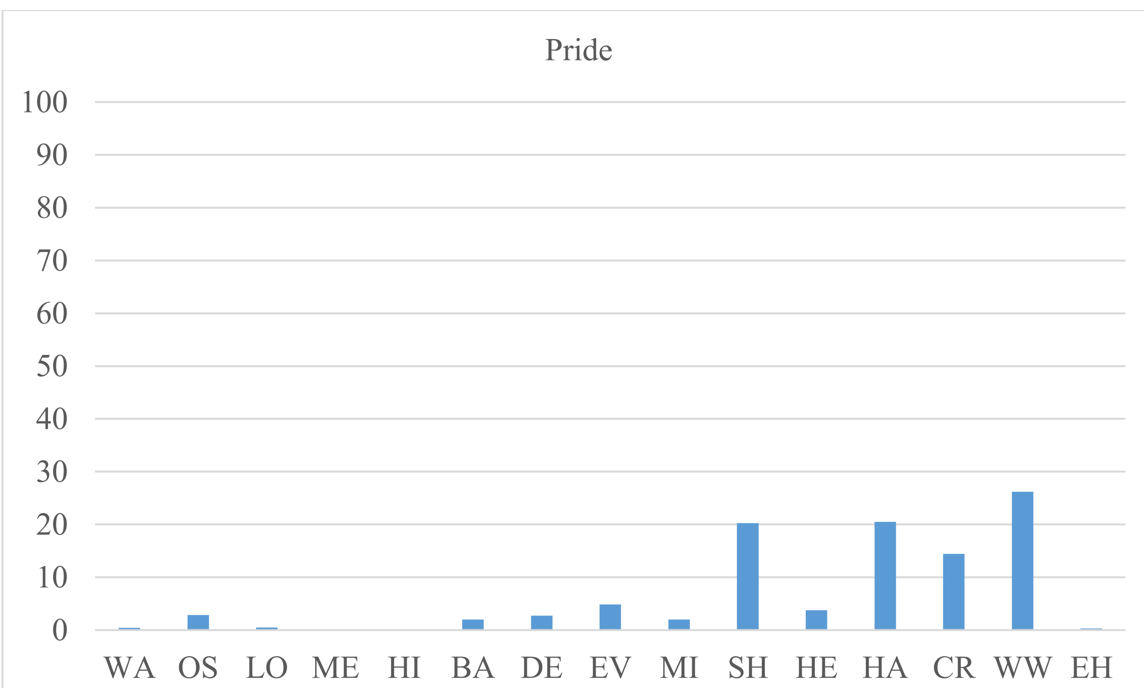

Figure 3.12 Percentages of NLCD classes within a 2000 m buffer around the Pride air quality monitor in the BRNZ.

Table 3.2 Ozone monitoring sites in study area.

Name	Lat.	Lon.
Bayou Plaquemine	30.220556	-91.316111
Capitol	30.46198	-91.17922
Carville	30.206985	-91.129948
Convent	29.994444	-90.82
Dutchtown	30.233889	-90.968333
French Settlement	30.3125	-90.8125
LSU	30.419763	-91.181996
New Roads	30.681736	-91.366172
Port Allen	30.500643	-91.213556
Pride	30.700921	-91.056135

Algorithms for counting a day as having complete data mirror those used by USEPA. The specific algorithm is described as follows. The daily maximum 8-hour concentration for a given day is the highest of the 24 possible 8-hour mean mixing ratios computed for that calendar day. Running 8-hour averages are computed from the hourly O_3 mixing ratio data and the result is stored in the first hour of the 8-hour period. An 8-hour average is considered valid if at least 6 of 8 hourly averages for the 8-hour period are available. An O_3 monitoring day is counted as a valid day if valid 8-hour averages are available for at least 18 of 24 possible hours in the day. If fewer than 18 of the 8-hour averages are available, a day is counted as a valid day if the daily maximum 8-hour average mixing ratio for that day exceeds the ambient standard.

3.2.3 Ozone Seasonality in Baton Rouge

O_3 maxima in BRNZ have a clear seasonal trend with more spread and greater extremes in the late spring and summer than in winter months. Observations from each station exhibit this pattern (Figures 3.13 to Figure 3.22), although the some stations have more intermonthly spread than others, and extremes vary. The number of exceedances of the 75 ppb design value ranges from 42 occurrences at Convent to 121 occurrences at LSU.

3.3. Predictor Variables Creation

To investigate the potential explanatory ability of different LCs, univariate regression analysis was conducted whereby a proportion for a LC type within a buffer radius was regressed against O_3. Around each of the ten air quality monitors buffers of radii 100, 200, 300, 400, 500, 1000, 1500, 2000, 2500, 3000, 3500, 4000, 4500, 5000, 7500, and 10000 m were computed. Within each buffer, the proportion of each of the 15 LC classes that appear in the study area was computed. This was repeated for NLCD 2001, NLCD 2006, and NLCD 2011.

3.4. Response Variables

3.4.1 O_3 Means

Daily maximum 8-hr O_3 for ten air quality monitors yield up to n=3650 for a given year if all observations are valid. In the BRNZ, all stations were operational for all years considered in this study, and data completeness at the ten sites averages 97.5%. Daily maximum 8-hr O_3 observations from 2001, 2006, and 2011—years corresponding to the NLCD editions—were n=10714. LUR models were evaluated for two averaged O_3 predictands in addition to the daily O_3. The daily O_3 (n=10714) and monthly mean (n=360) are referred to as Metric A and Metric B respectively. The second averaged O_3 predictand is a triennial monthly mean (n=360) based on three 3-year windows (2000–2002, 2005–2007, and 2010–2012) centered on the NLCD edition years. This is Metric C.

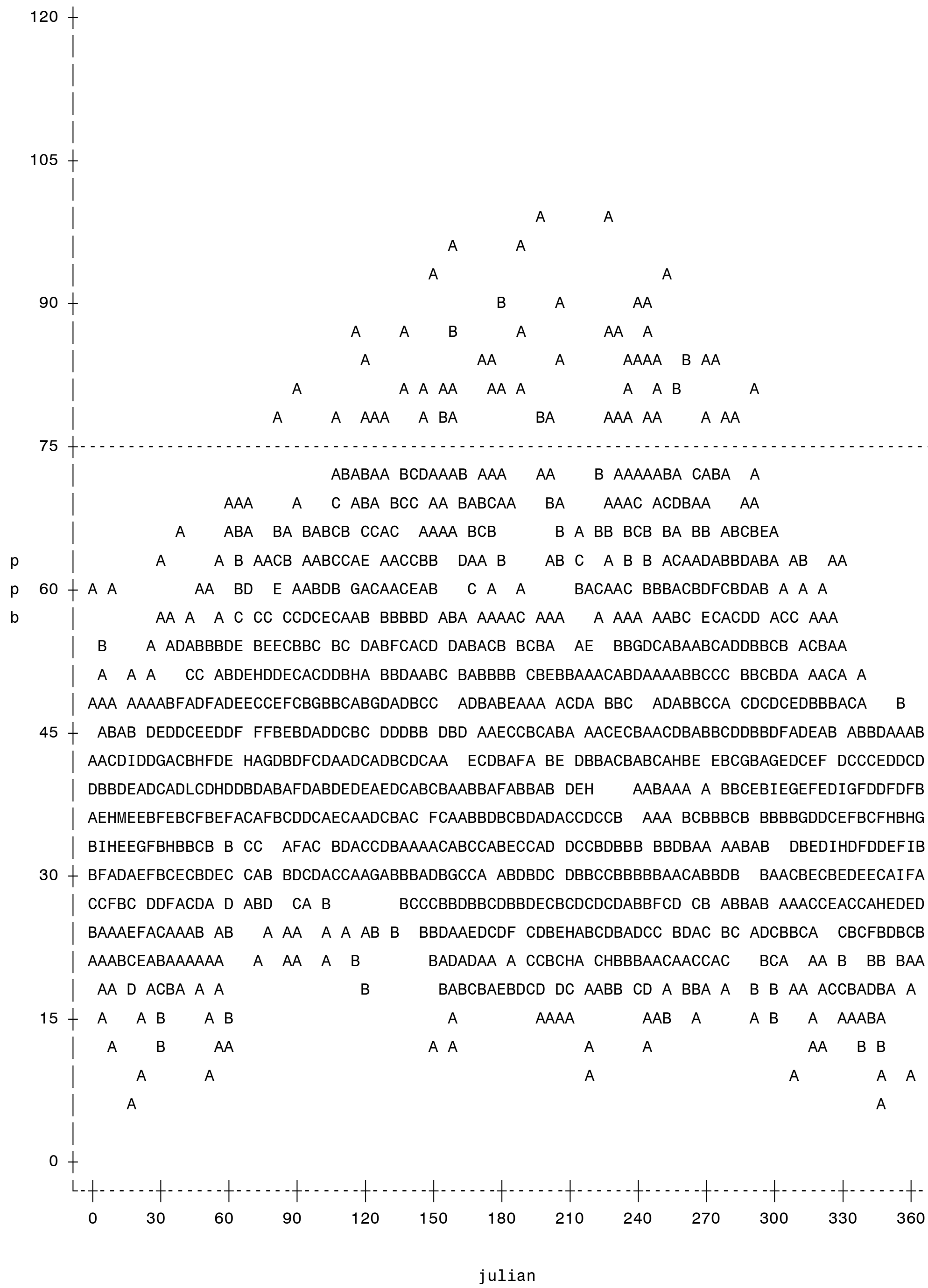

Figure 3.13 Daily O_3 maxima for Bayou Plaquemine from the years 2000–2012 plotted against the Julian day with a reference line at the 75 ppb design value.

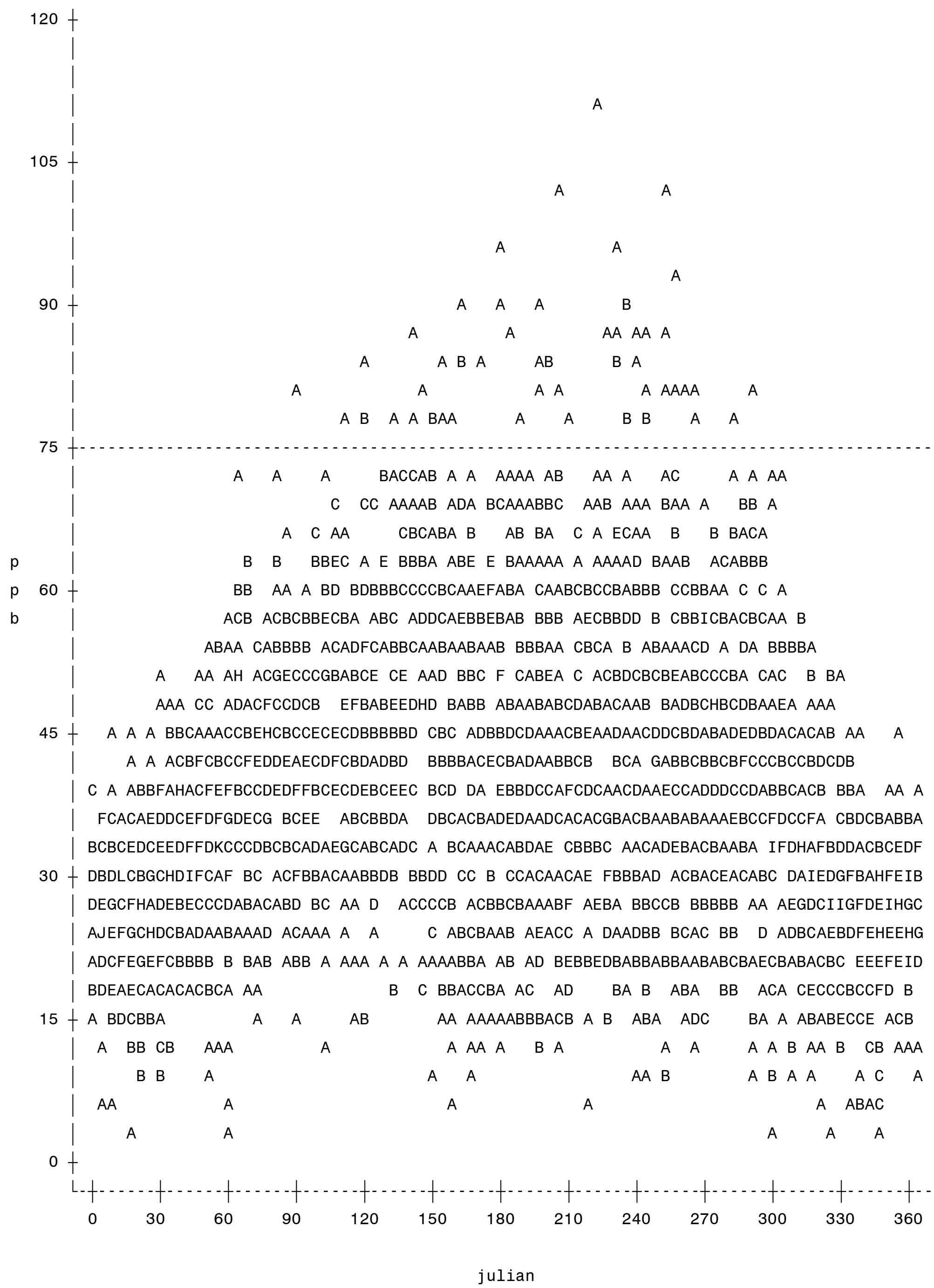

Figure 3.14 Daily O_3 maxima for Capitol from the years 2000–2012 plotted against the Julian day with a reference line at the 75 ppb design value.

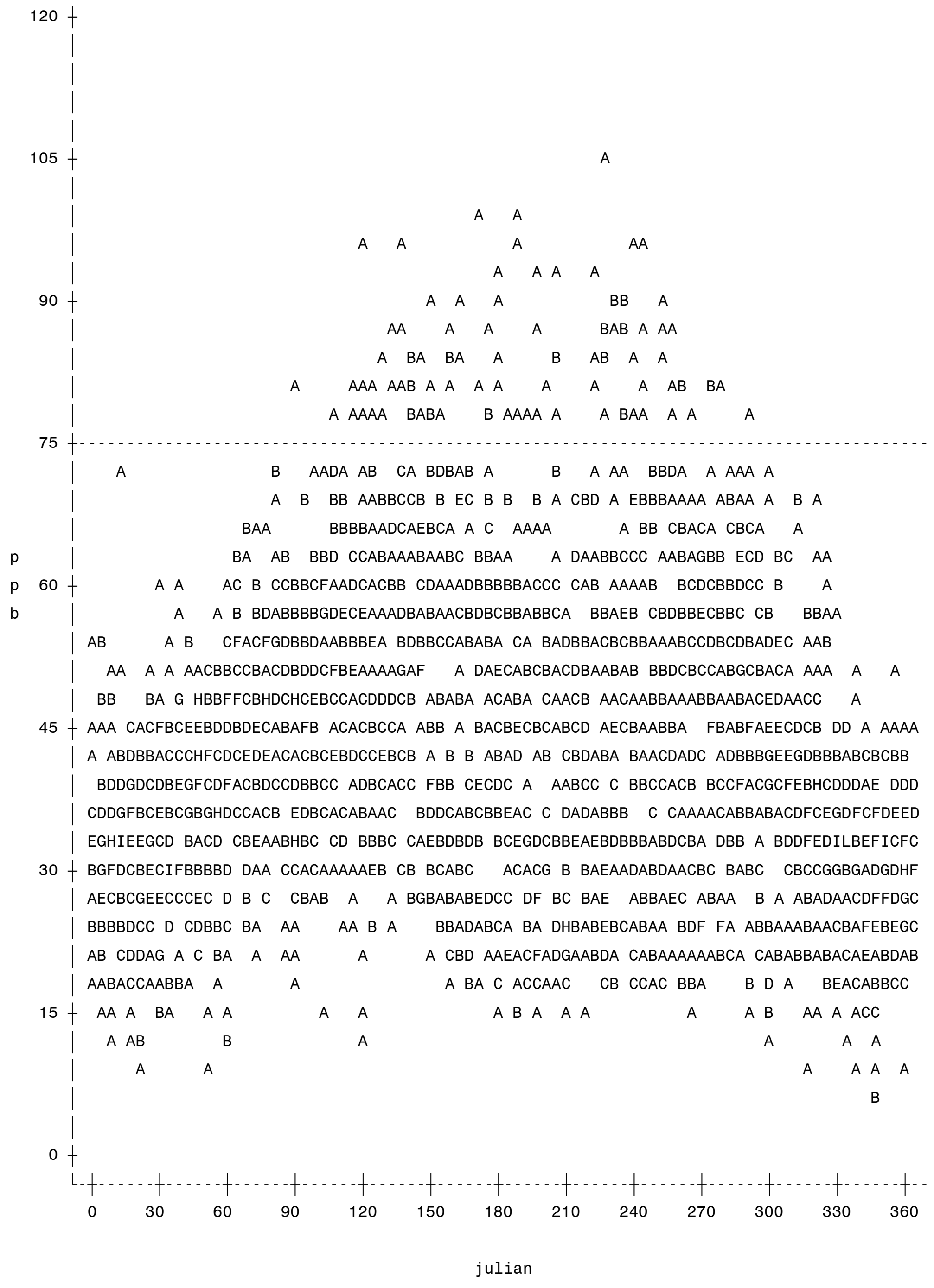

Figure 3.15 Daily O_3 maxima for Carville from the years 2000─2012 plotted against the Julian day with a reference line at the 75 ppb design value.

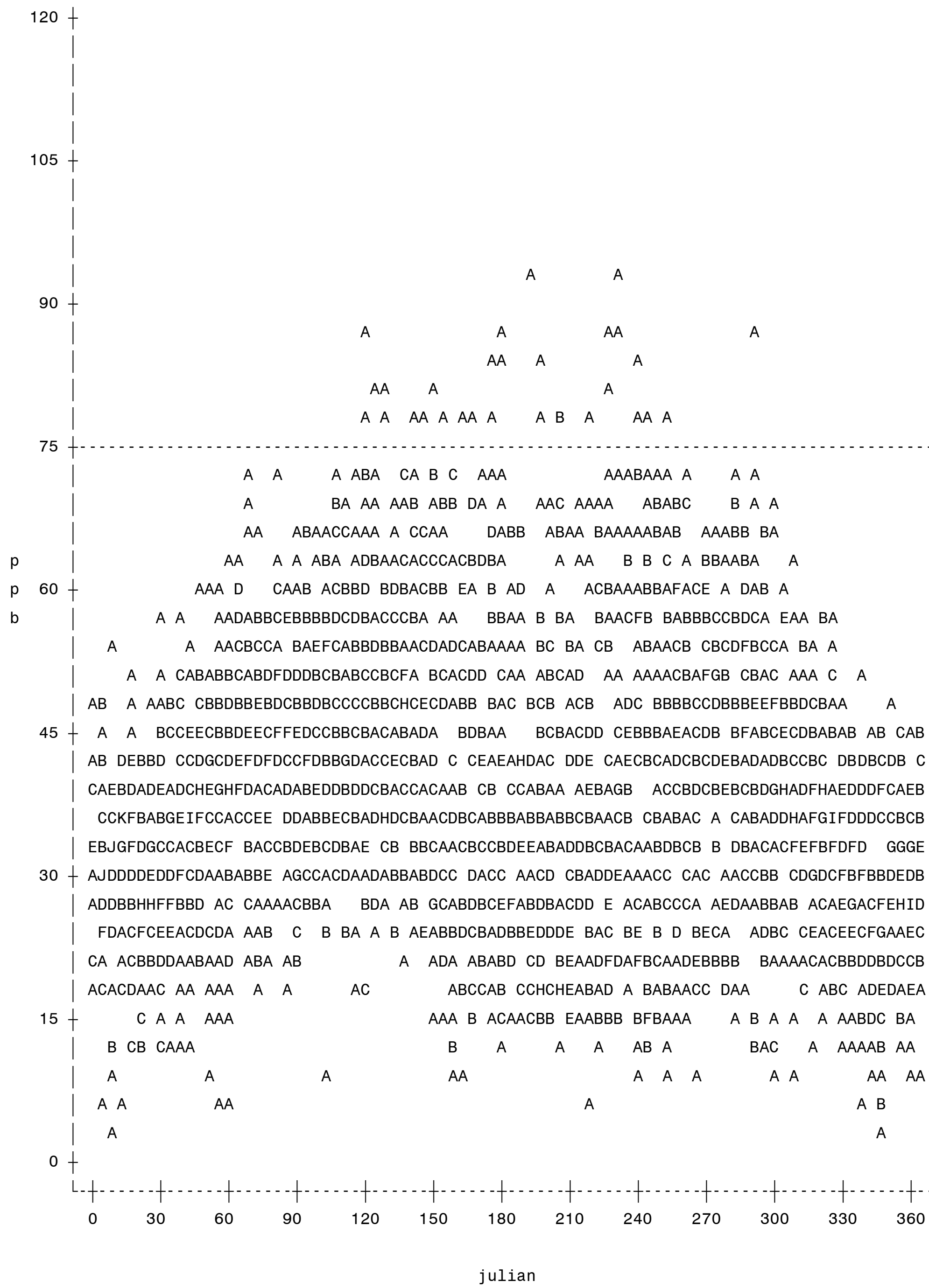

Figure 3.16 Daily O_3 maxima for Convent from the years 2000─2012 plotted against the Julian day with a reference line at the 75 ppb design value.

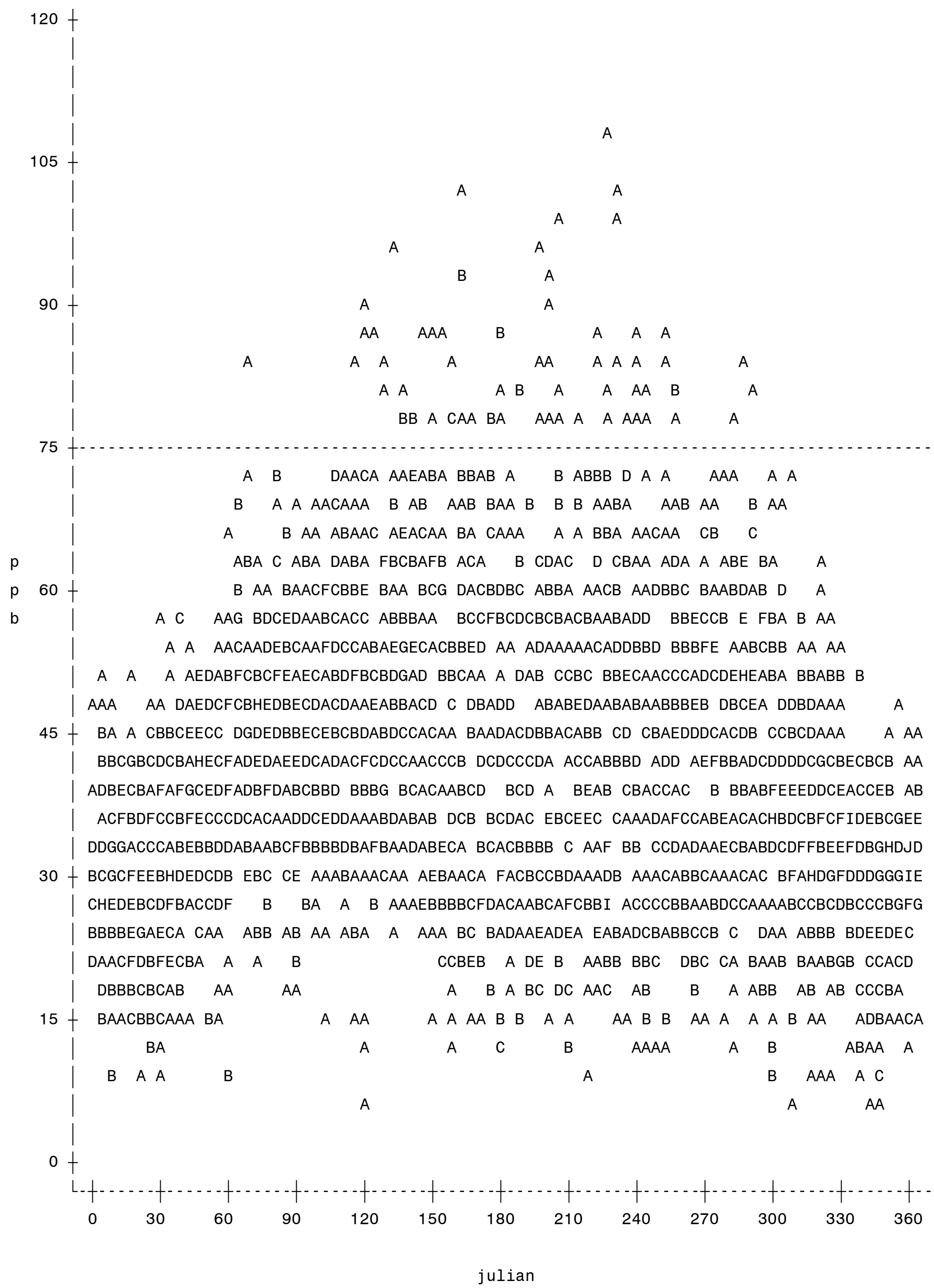

Figure 3.17 Daily O_3 maxima for Dutchtown from the years 2000–2012 plotted against the Julian day with a reference line at the 75 ppb design value.

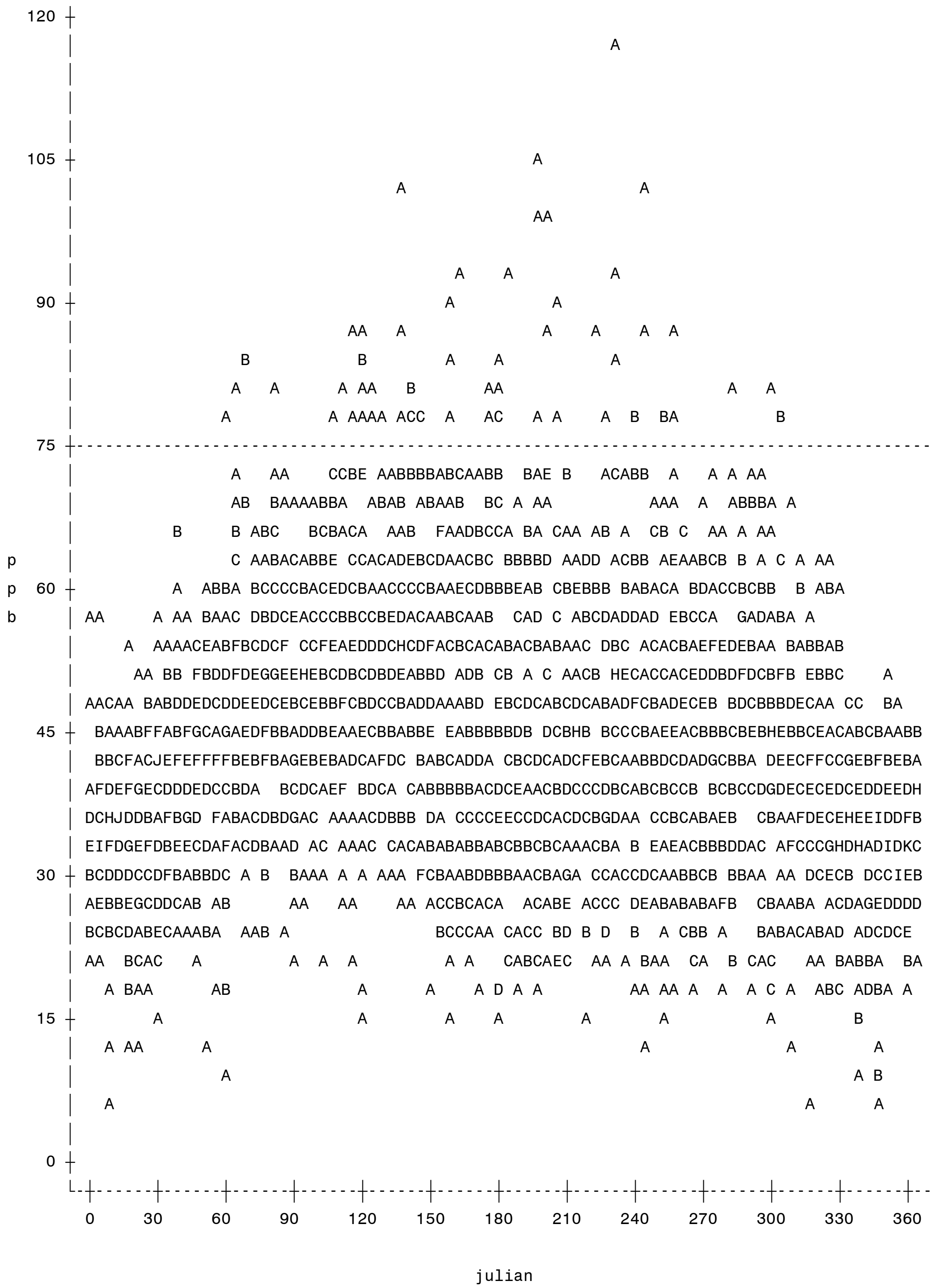

Figure 3.18 Daily O_3 maxima for French Settlement from the years 2000–2012 plotted against the Julian day with a reference line at the 75 ppb design value.

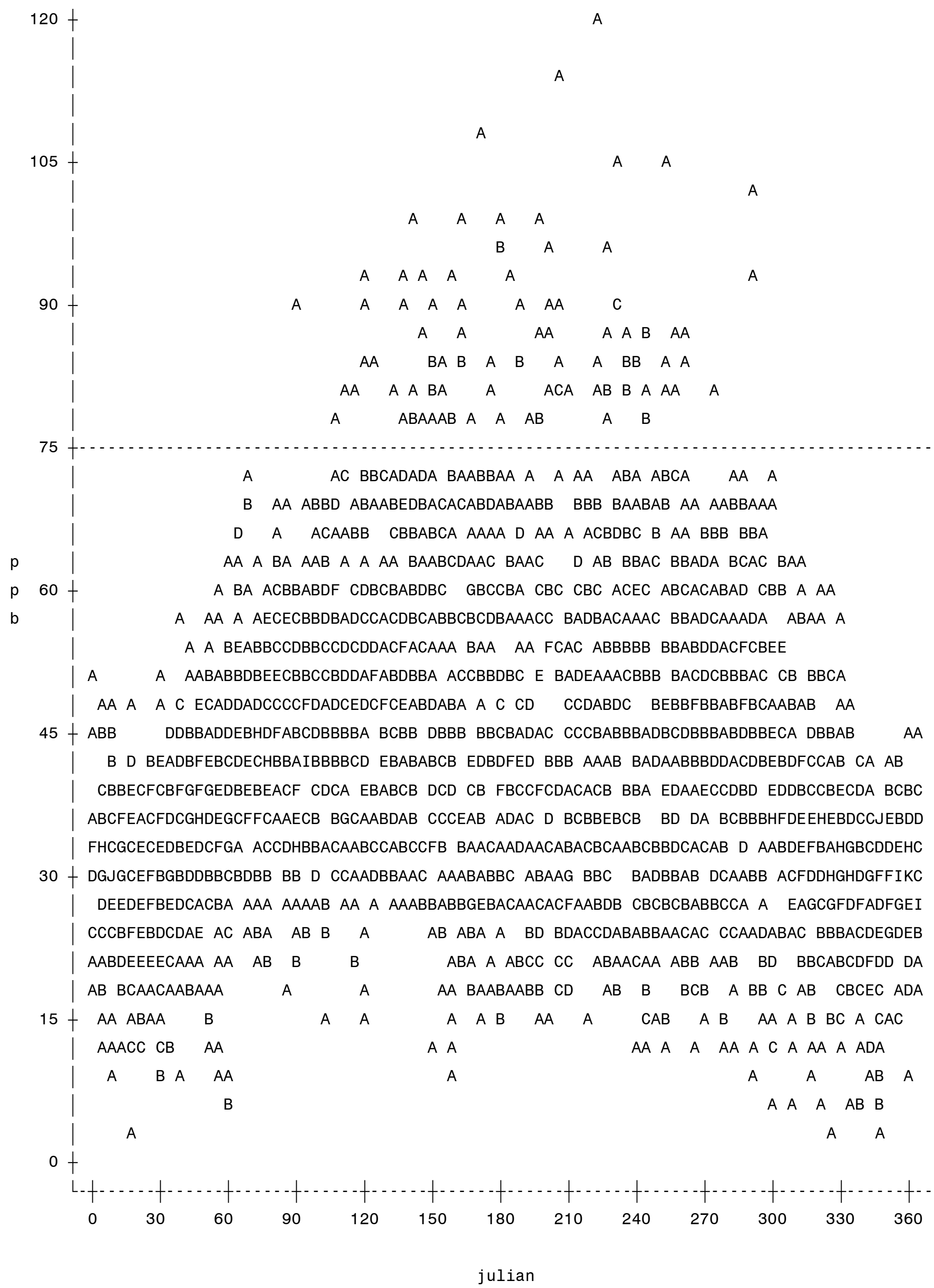

Figure 3.19 Daily O_3 maxima for LSU from the years 2000─2012 plotted against the Julian day with a reference line at the 75 ppb design value.

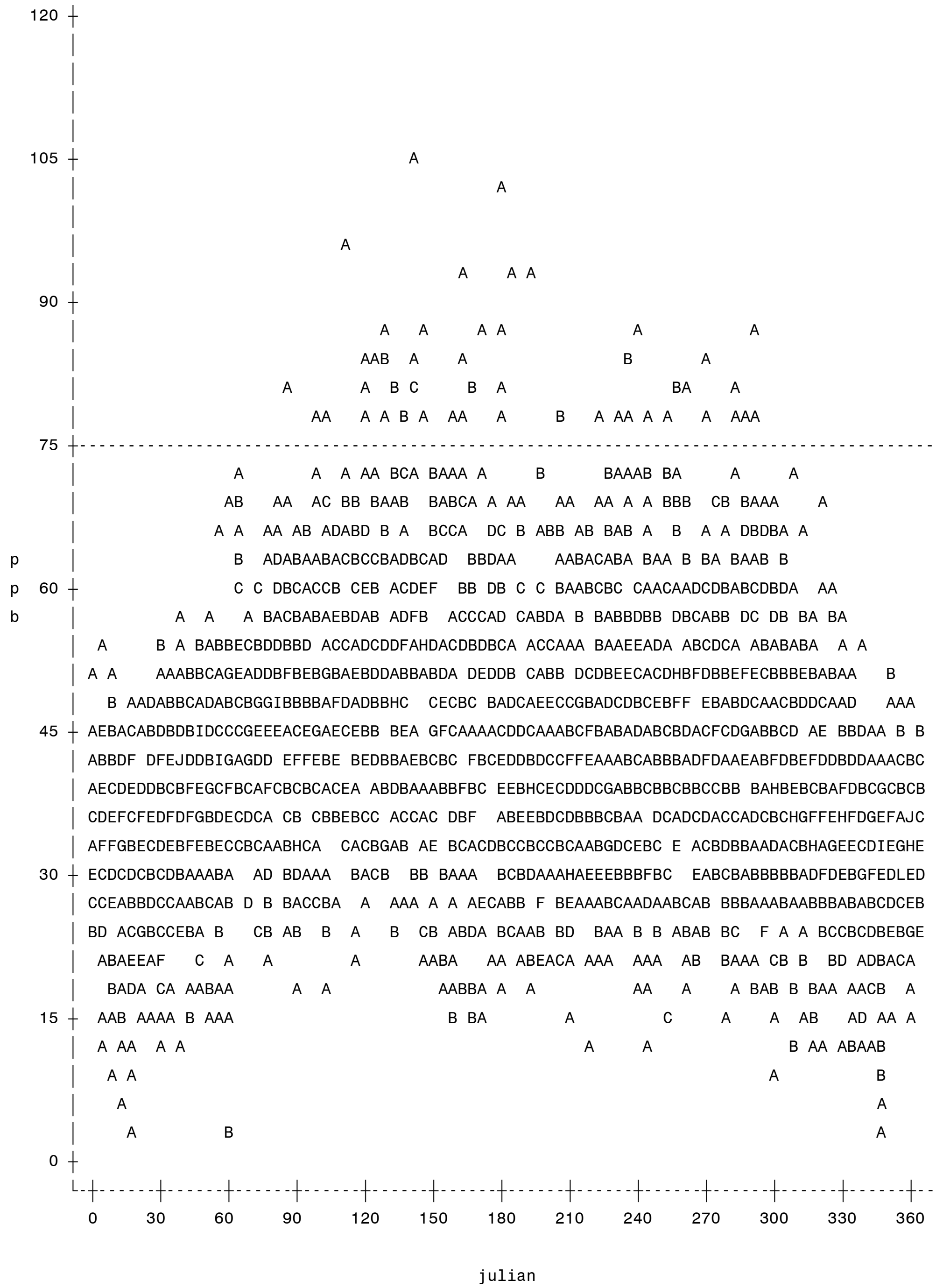

Figure 3.20 Daily O_3 maxima for New Roads from the years 2000–2012 plotted against the Julian day with a reference line at the 75 ppb design value.

Figure 3.21 Daily O_3 maxima for Port Allen from the years 2000–2012 plotted against the Julian day with a reference line at the 75 ppb design value.

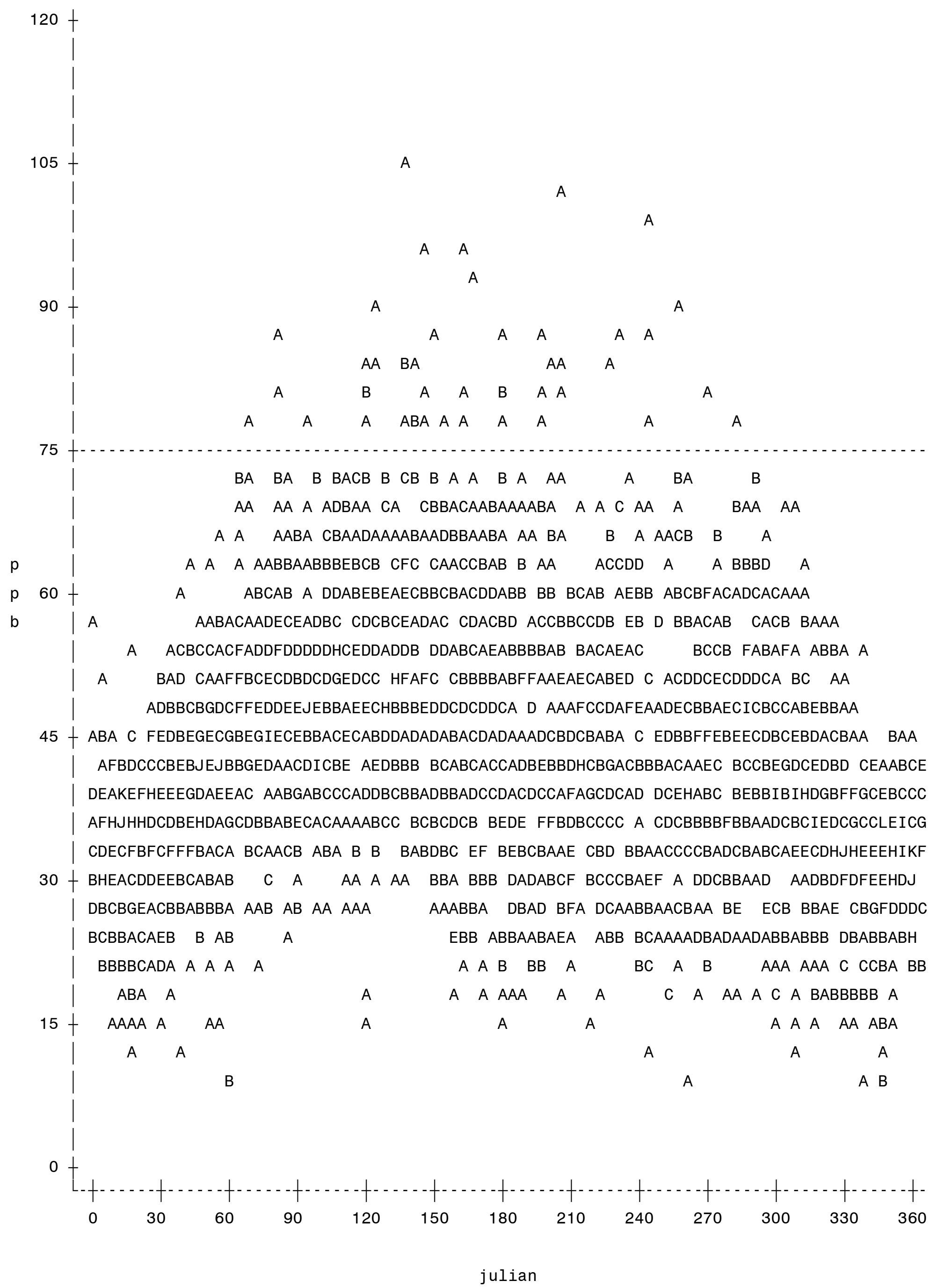

Figure 3.22 Daily O_3 maxima for Pride from the years 2000–2012 plotted against the Julian day with a reference line at the 75 ppb design value.

3.4.2 Deviations-from-the-Regional-Means

Synoptic-scale meteorology may confound local-scale variability in O_3 mixing ratios. Rather than risk modelling the contribution of synoptic-scale meteorology incompletely, Abraham and Comrie (2004) removed the regional mean prior to modelling. Since official meteorological data for the BRNZ is recorded only at the airport which is displaced from any air quality monitor, this study follows the example of Abraham and Comrie (2004) in using deviations-form-the-regional-mean (devRM) rather than direct observations (DO). By doing so, meteorological data limitations are overcome, and site-specific variability is emphasized.

Figure 3.23 displays the ppb data published by USEPA. A clear seasonal trend is visible with the daily maximum 8-hr mean O_3 mixing ratio during northern hemisphere summer months exceeding the maxima reached in early spring and winter. Interestingly, the data for 2001 dips around Julian day 160. Observed decreases in O_3 mixing ratios within a few hundred km of an intensifying storm (Zou and Wu 2005) combined with the development of Tropical Storm Allison in the northwestern Gulf of Mexico on 5 June 2001 provides a possible explanation for 2001 O_3 mixing ratios. Figure 3.24 shows the observations after removal of the daily regional mean, with data centered on zero. The effect of detrending on O_3 distribution by monitoring site is shown in Figures 3.25 to 3.44. Figures 3.25 to 3.34 are histograms of DO, and Figures 3.35 to 3.44 are histograms of devRM. Boxplots show the distributions of daily maxima of DO (Figures 3.45 to 3.53) and devRM (Figures 3.54 to 3.62) by year.

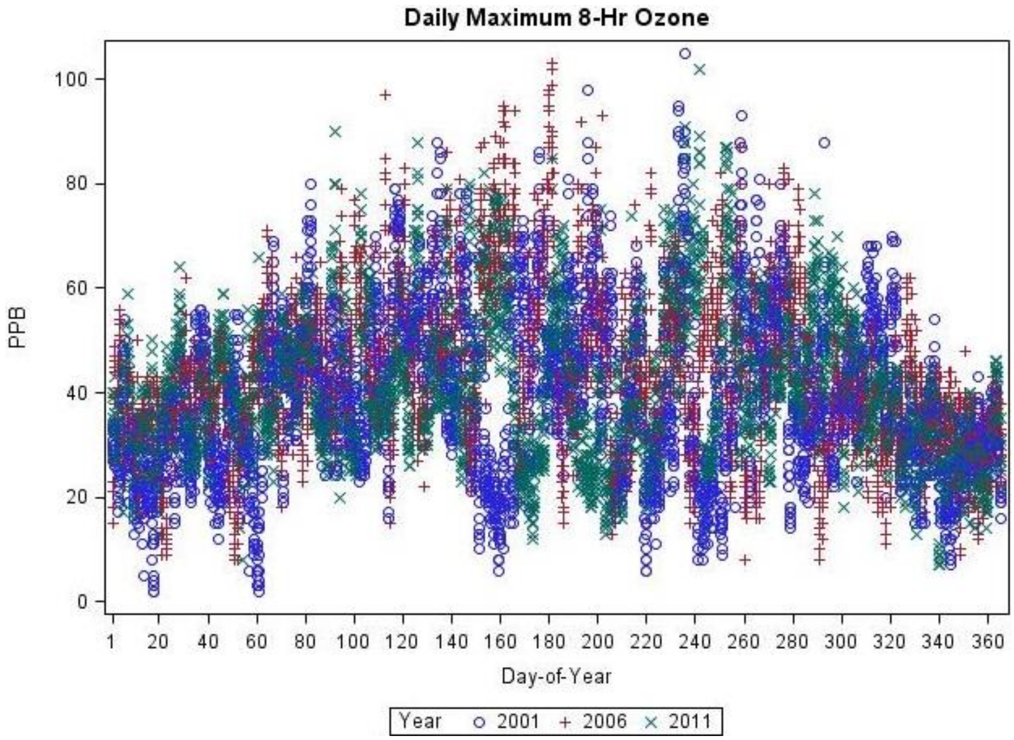

Figure 3.23 Daily maximum 8-hr mean O_3 for 2001, 2006, 2011.

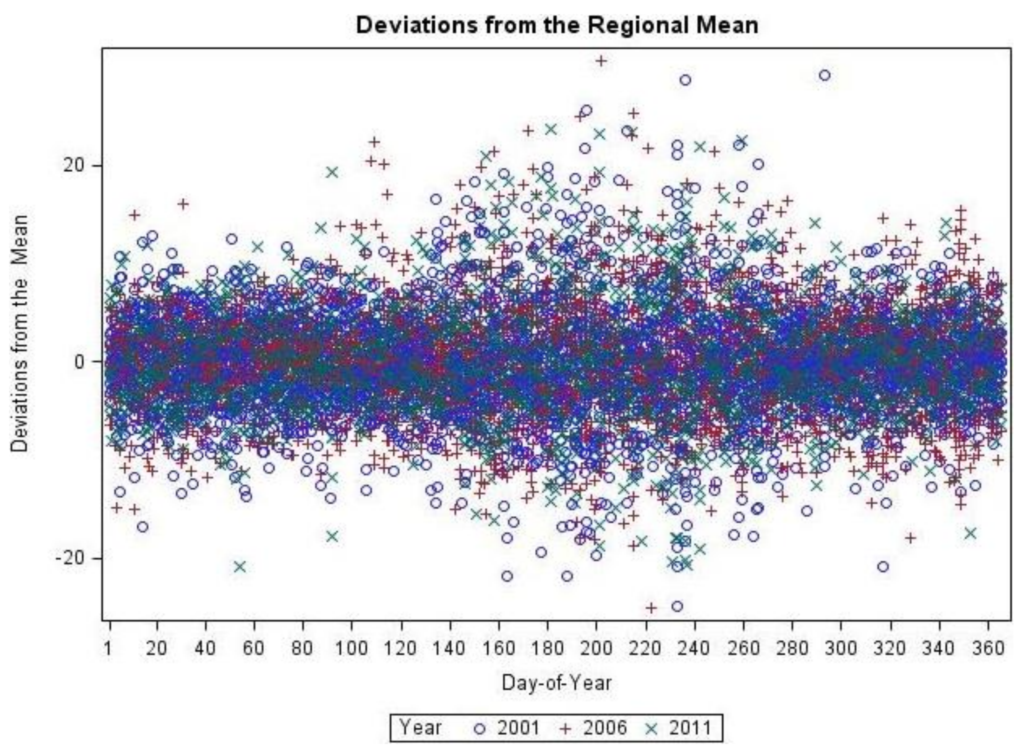

Figure 3.24 DevRM for daily maximum 8-hr mean O_3 for 2001, 2006, and 2011.

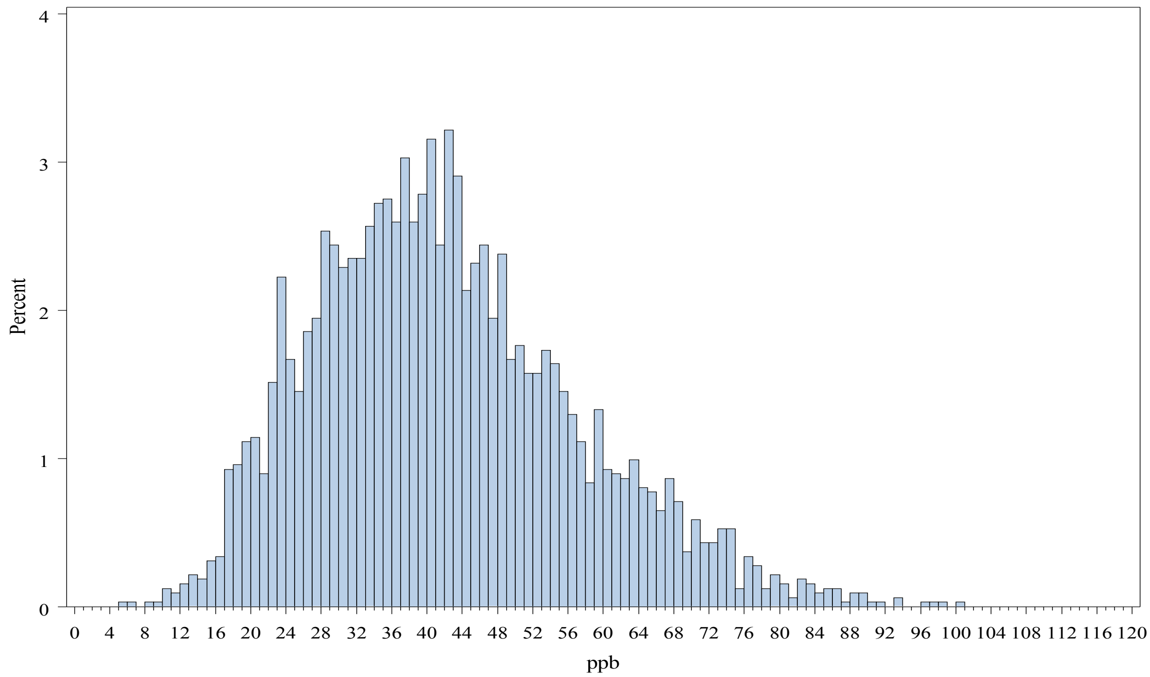

Figure 3.25 Histogram of DO for Bayou Plaquemine, with a mean of 41.65 ppb and a median of 40.

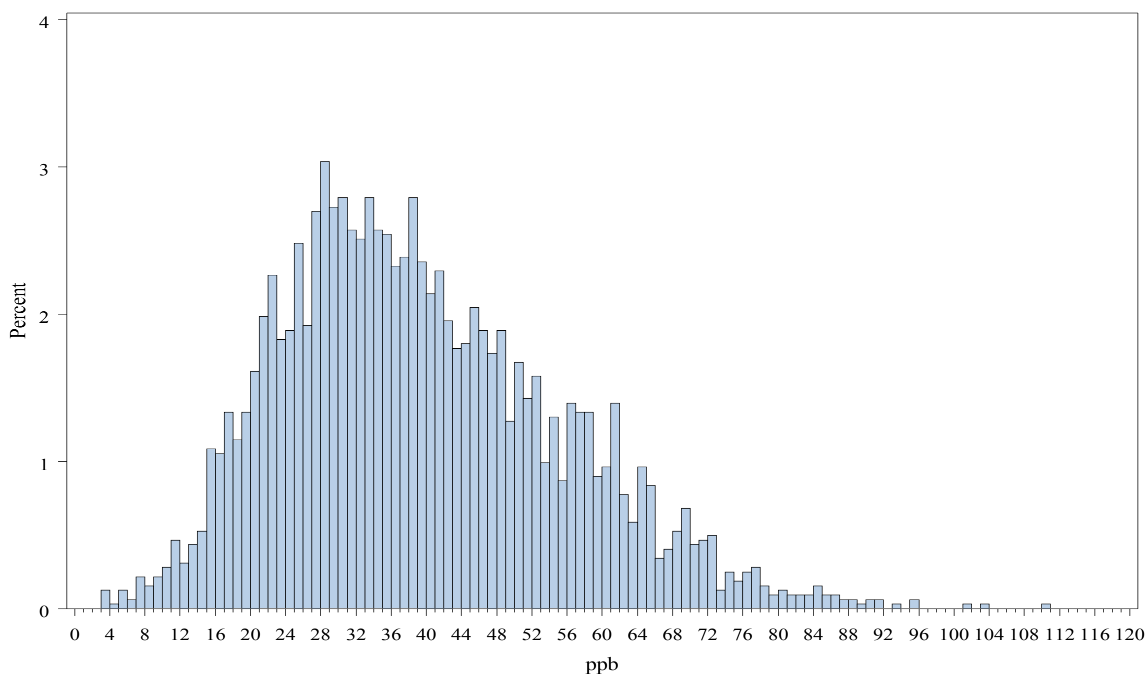

Figure 3.26 Histogram of DO for Capitol, with a mean of 38.82 ppb and a median of 37.

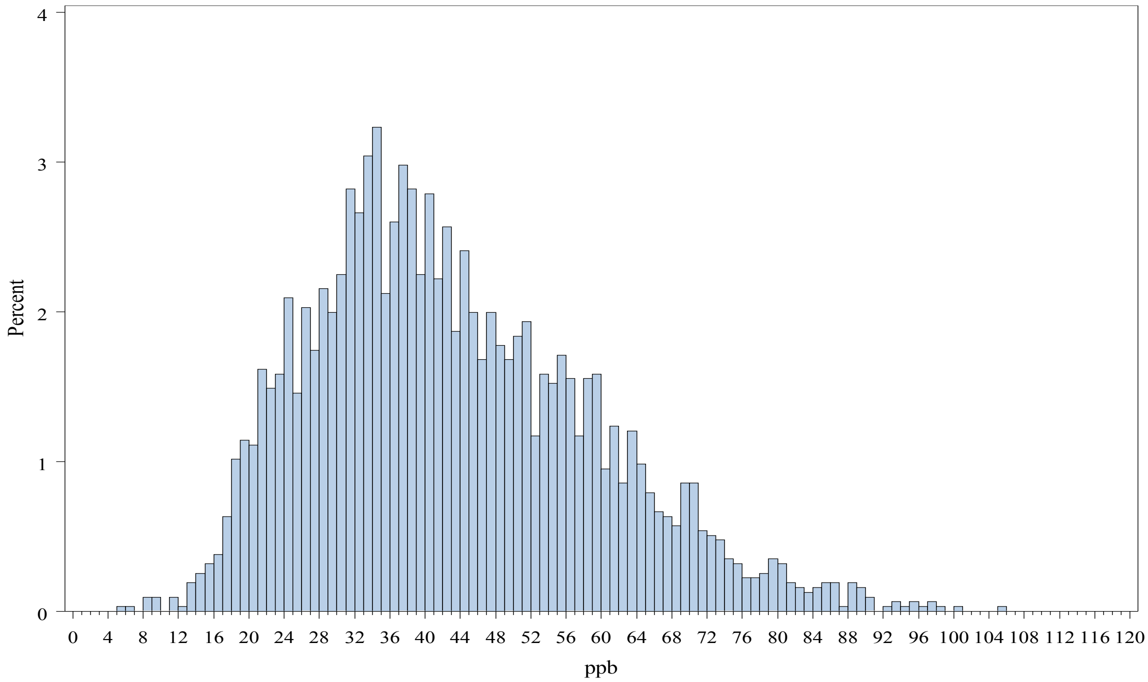

Figure 3.27 Histogram of DO for Carville, with a mean of 42.48 ppb and a median of 40.

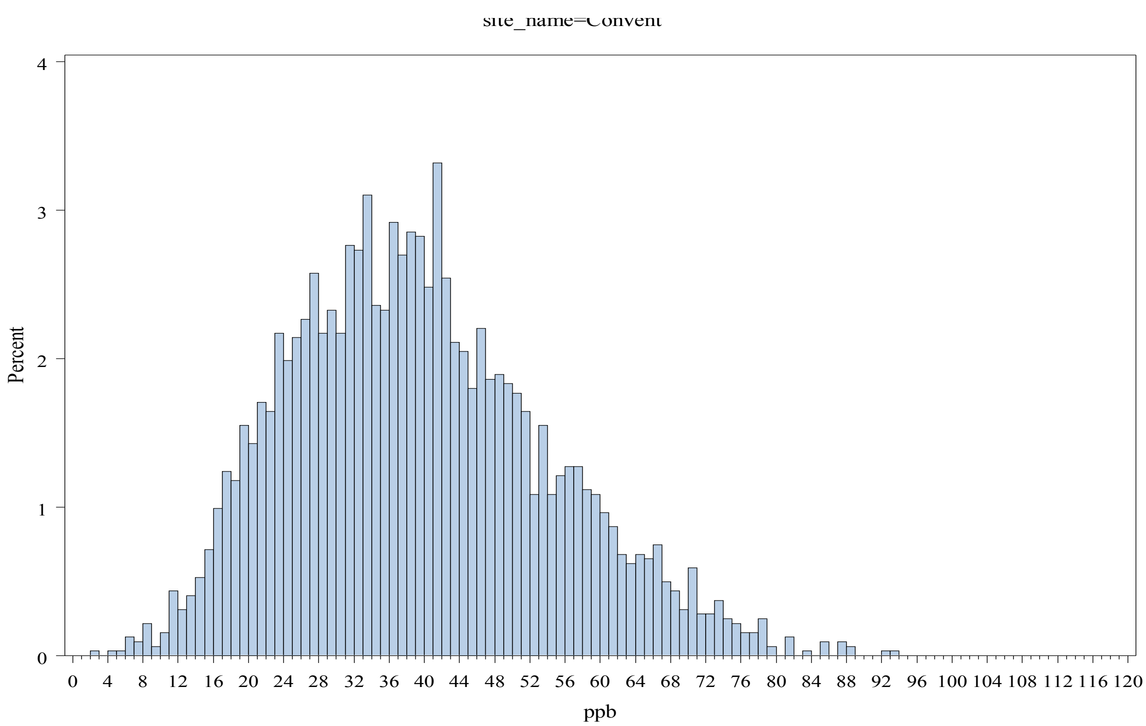

Figure 3.28 Histogram of DO for Convent, with a mean of 38.85 ppb and a median of 38.

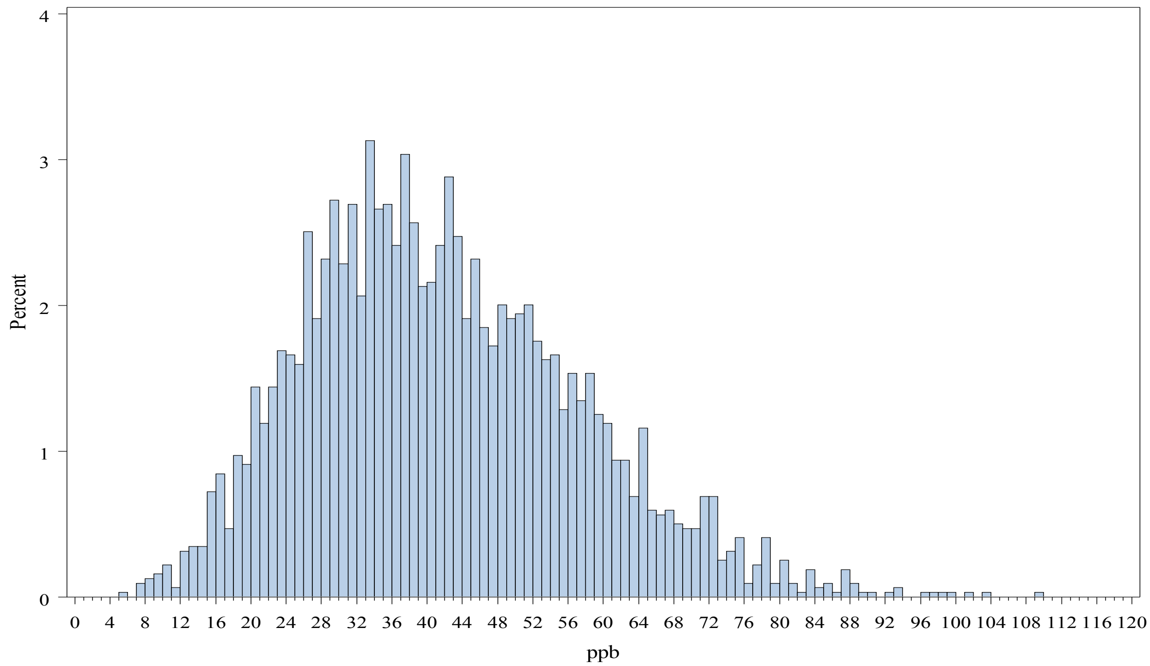

Figure 3.29 Histogram of DO for Dutchtown, with a mean of 41.32 ppb and a median of 40.

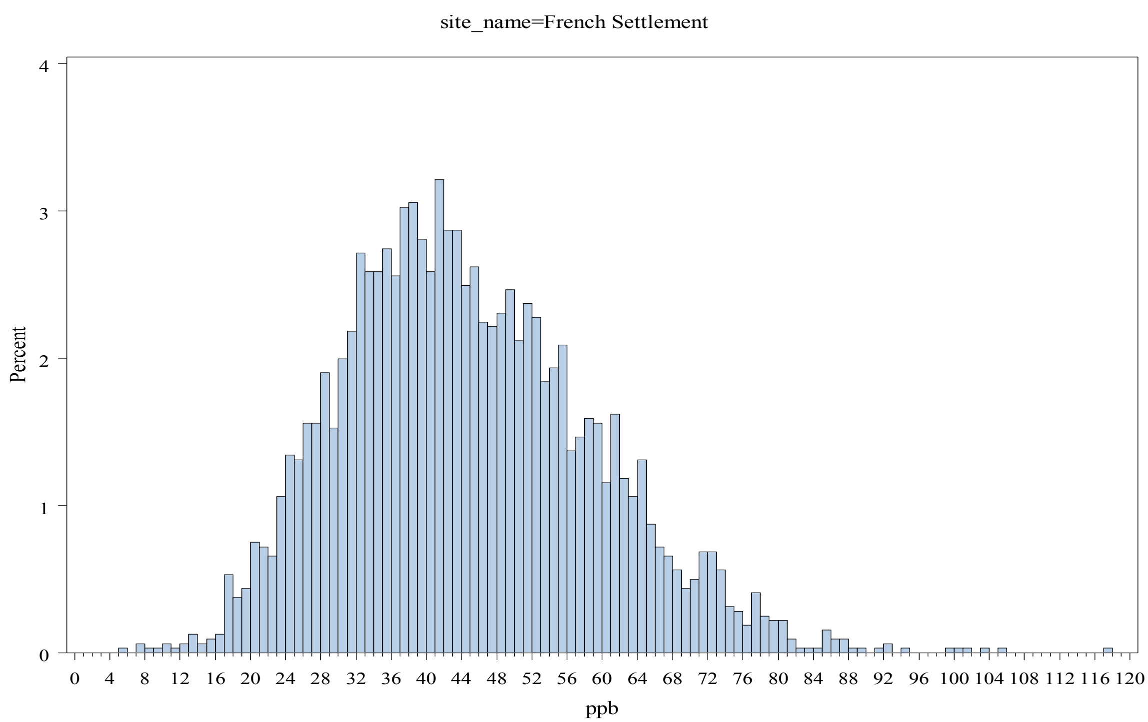

Figure 3.30 Histogram of DO for French Settlement, with a mean of 44.21 ppb and a median of 43.

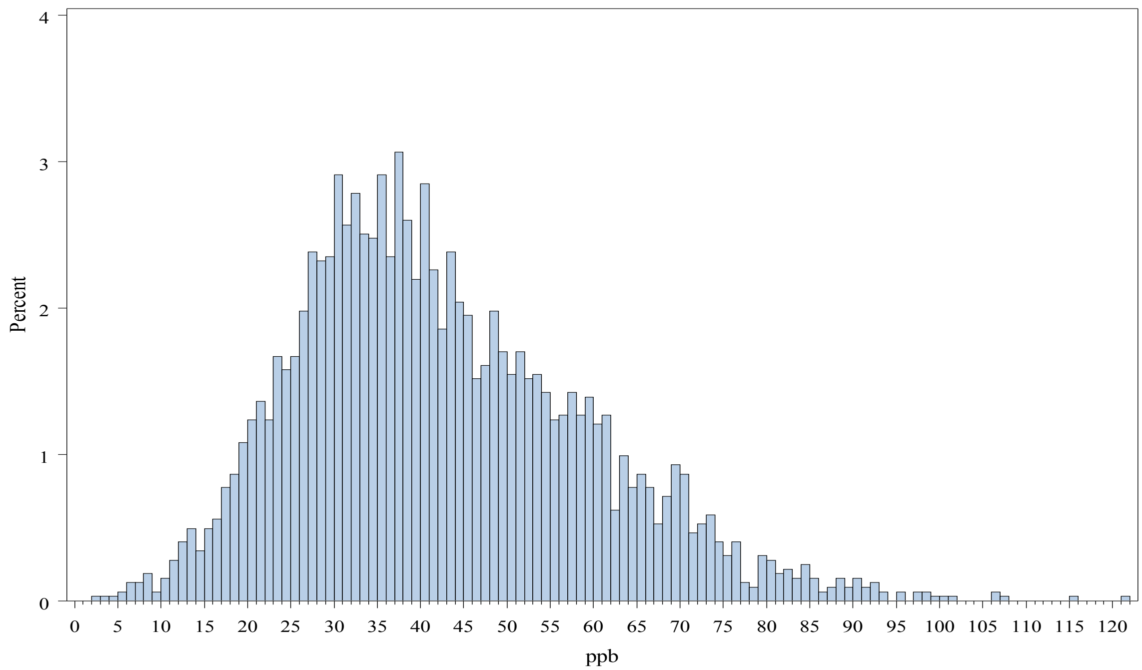

Figure 3.31 Histogram of DO for LSU, with a mean of 41.88 ppb and a median of 39.

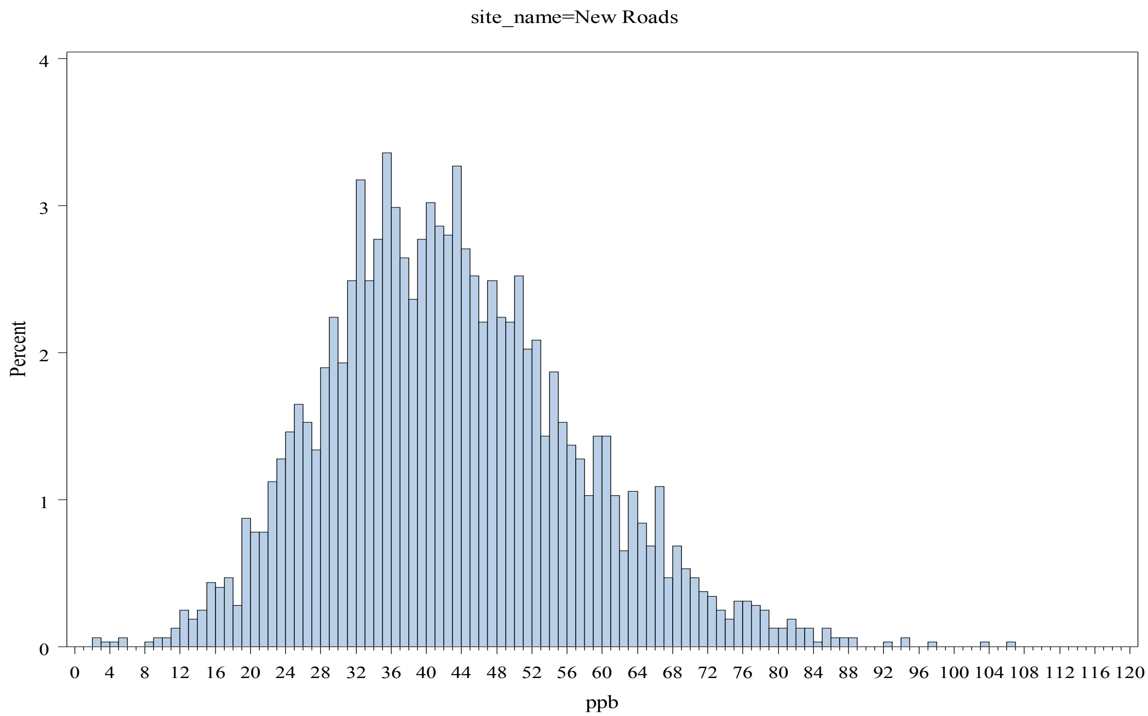

Figure 3.32 Histogram of DO for New Roads, with a mean of 42.47 ppb and a median of 41.

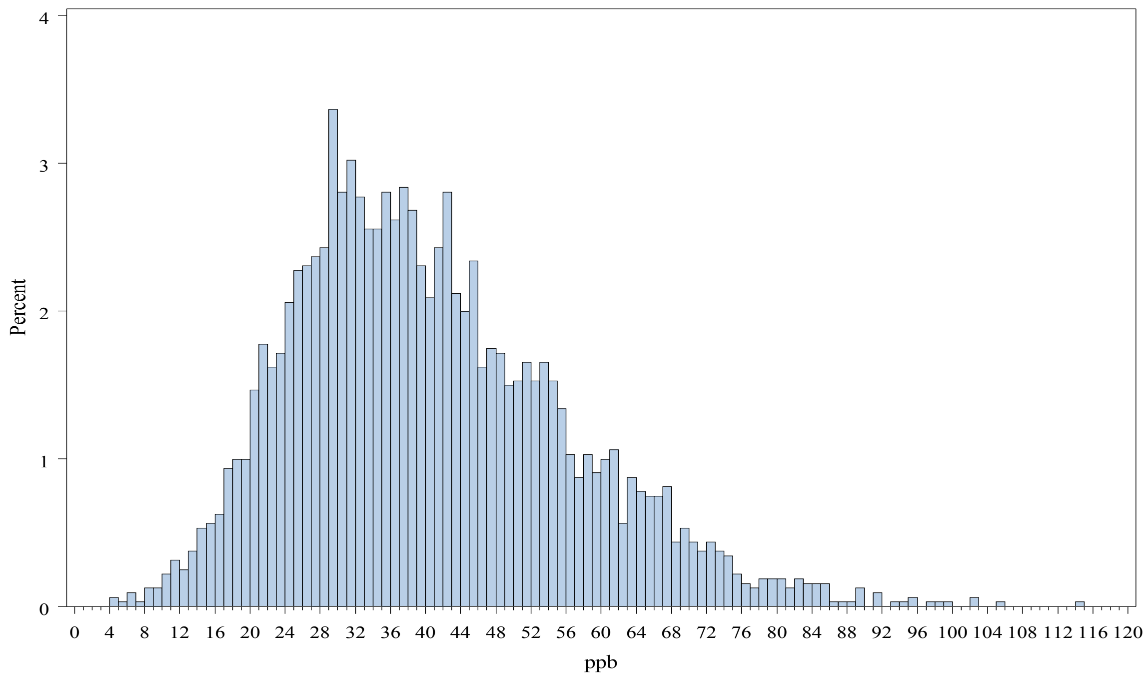

Figure 3.33 Histogram of DO for Port Allen, with a mean of 39.93 ppb and a median of 38.

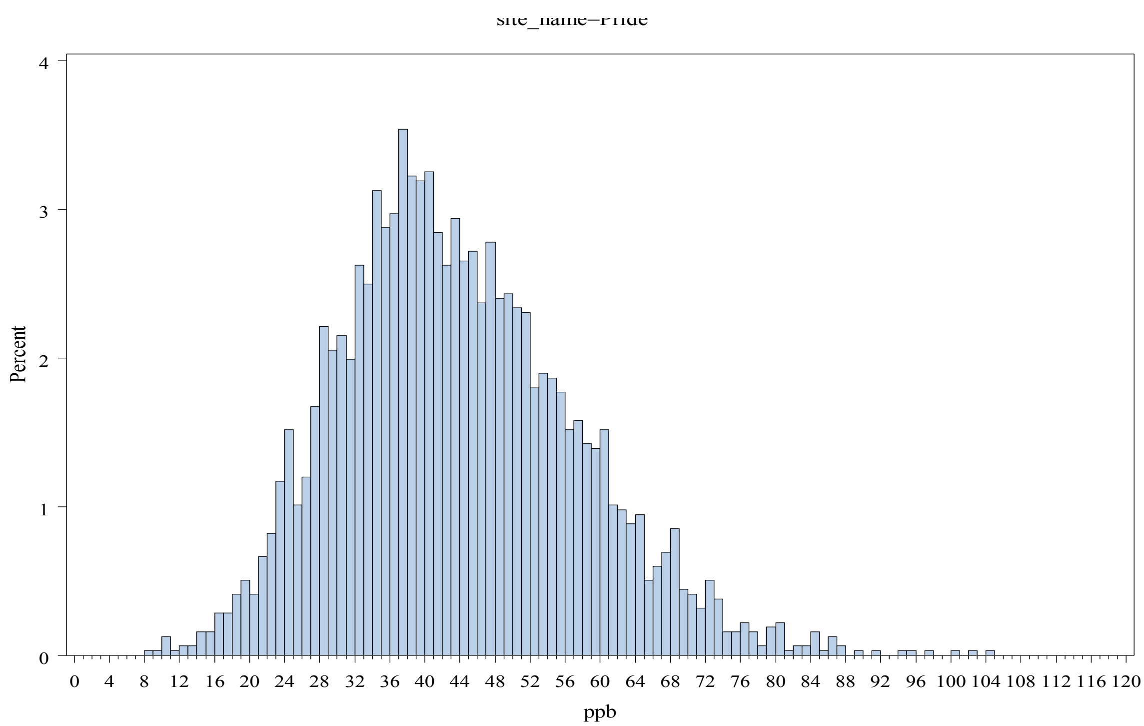

Figure 3.34 Histogram of DO for Pride, with a mean of 43.22 ppb and a median of 42.

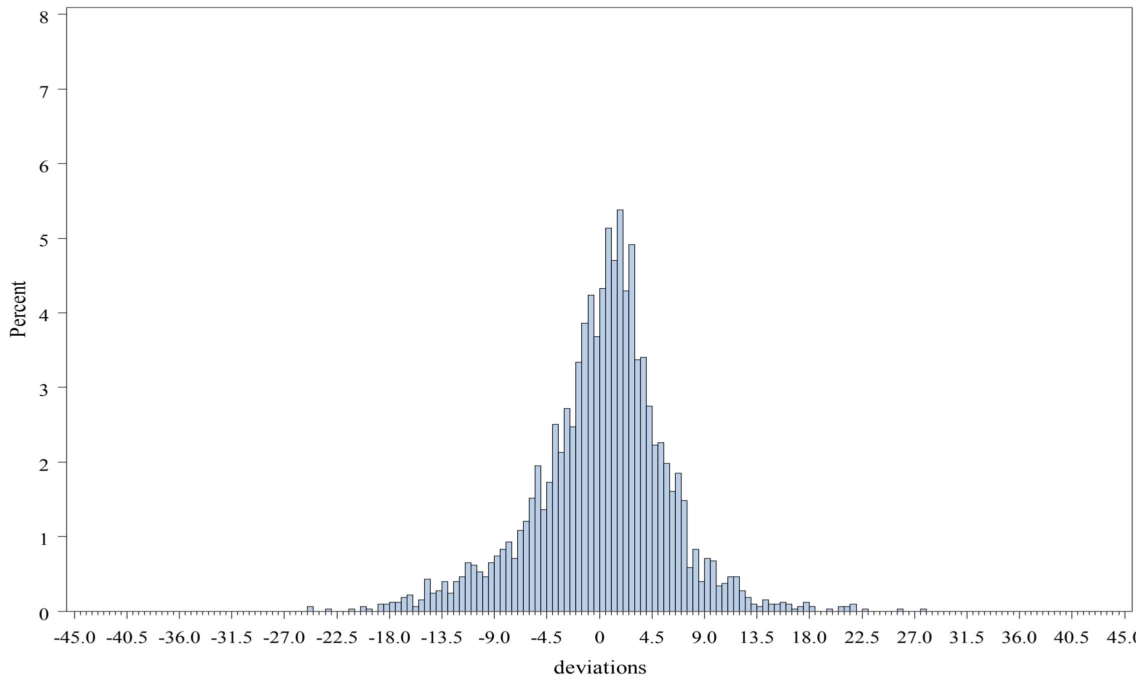

Figure 3.35 Histogram of devRM for Bayou Plaquemine, with a mean of 0.1406 and a median of 0666.

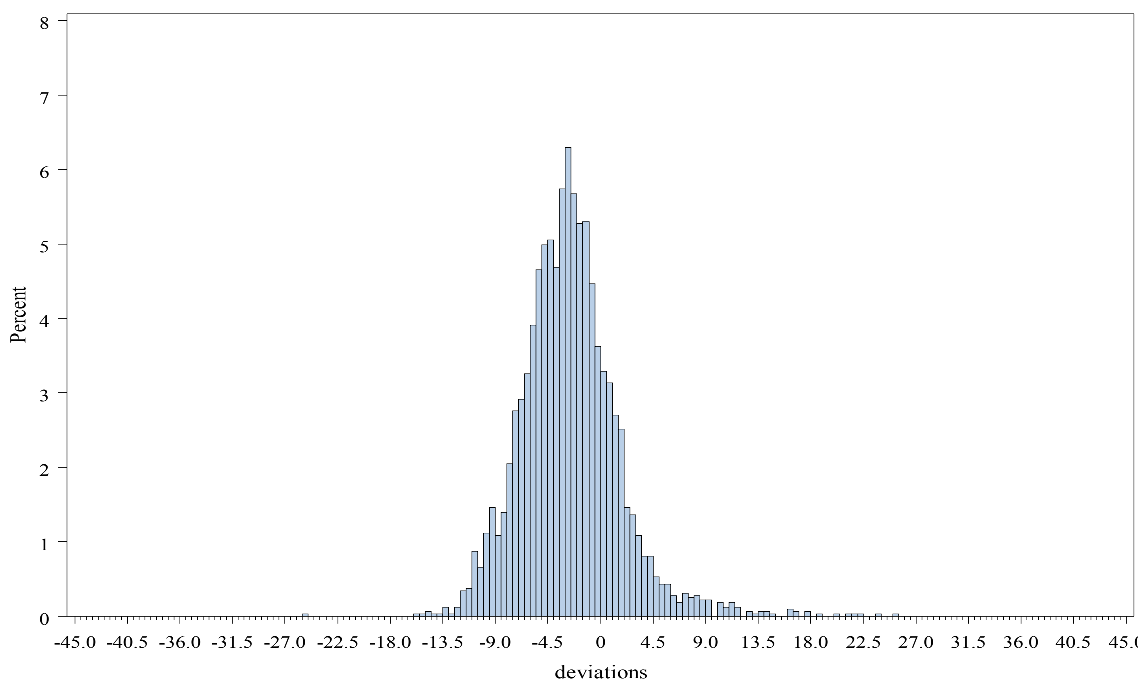

Figure 3.36 Histogram of devRM for Capitol, with a mean of –2.6845 and a median of –2.9.

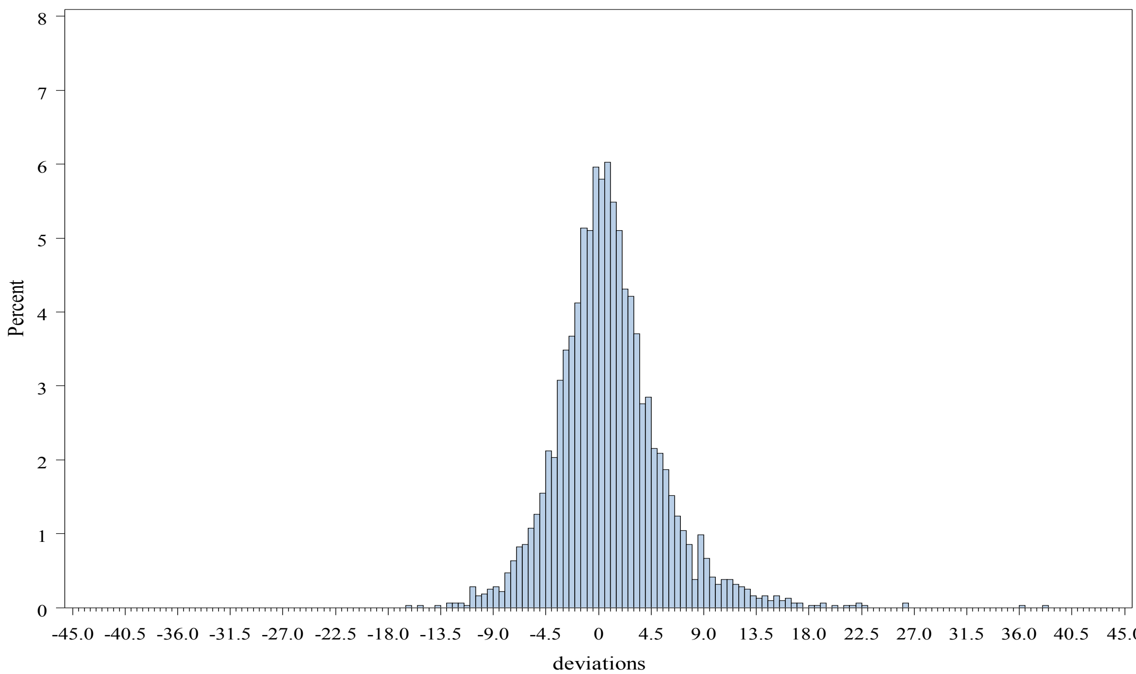

Figure 3.37 Histogram of devRM for Carville, with a mean of .8697 and a median of 0.5.

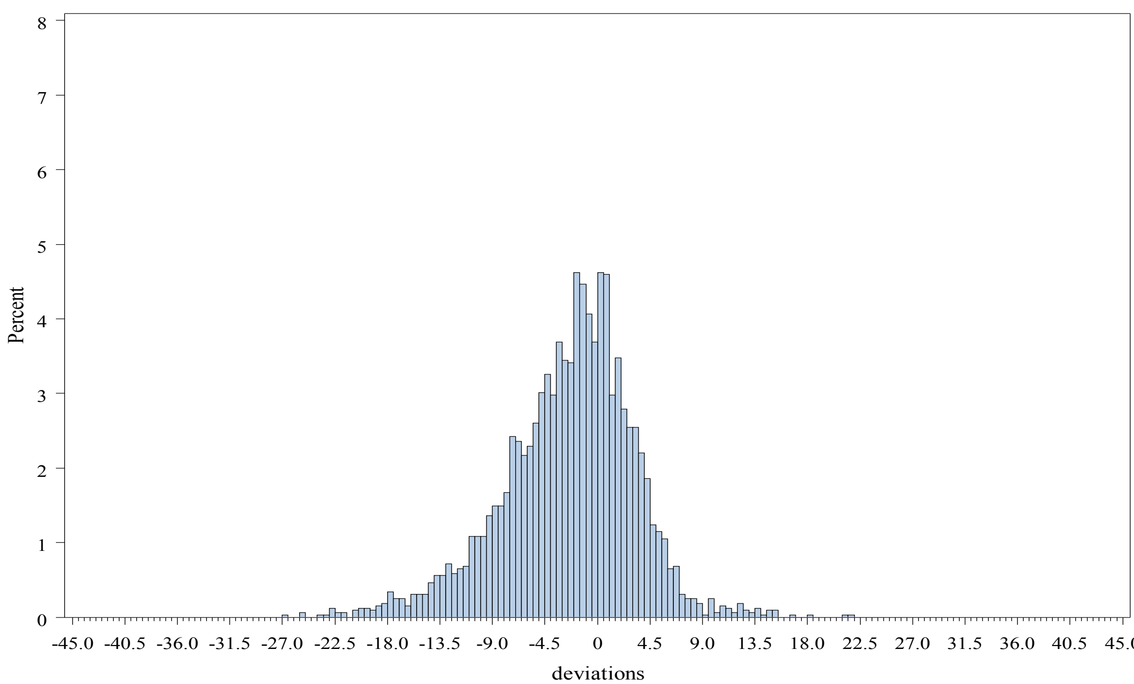

Figure 3.38 Histogram of devRM for Convent, with a mean of –0.2525 and a median of –1.8888.

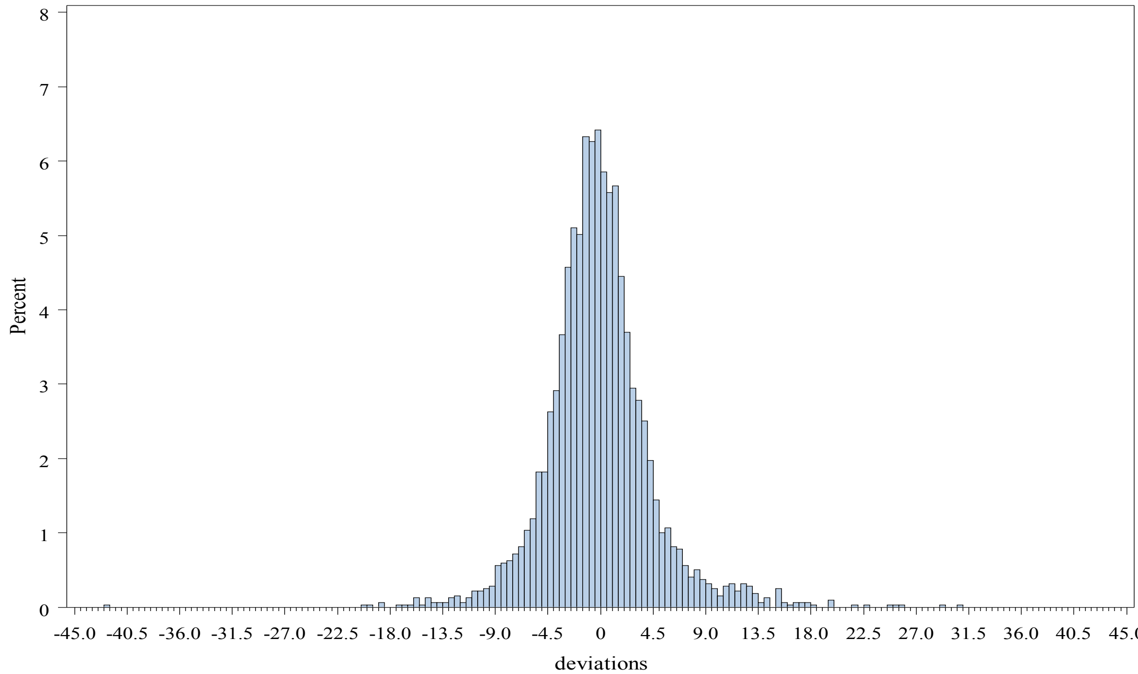

Figure 3.39 Histogram of devRM for Dutchtown, with a mean of –0.1781 and a median of –0.4.

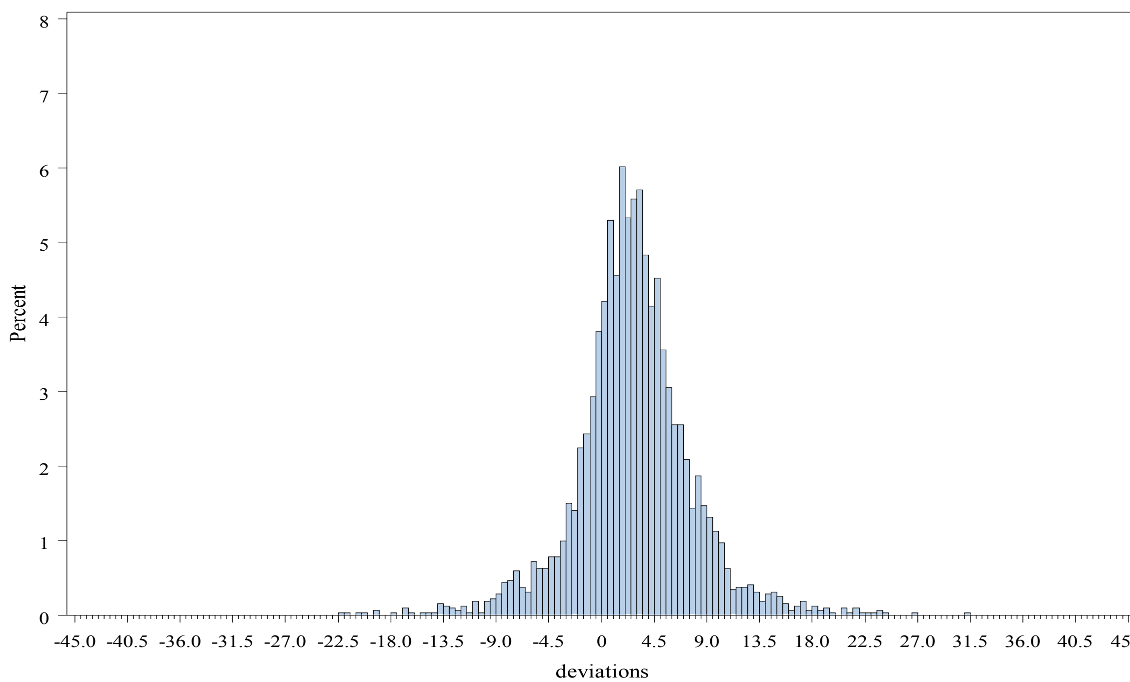

Figure 3.40 Histogram of devRM for French Settlement, with a mean of 2.6991 and a median of 2.6.

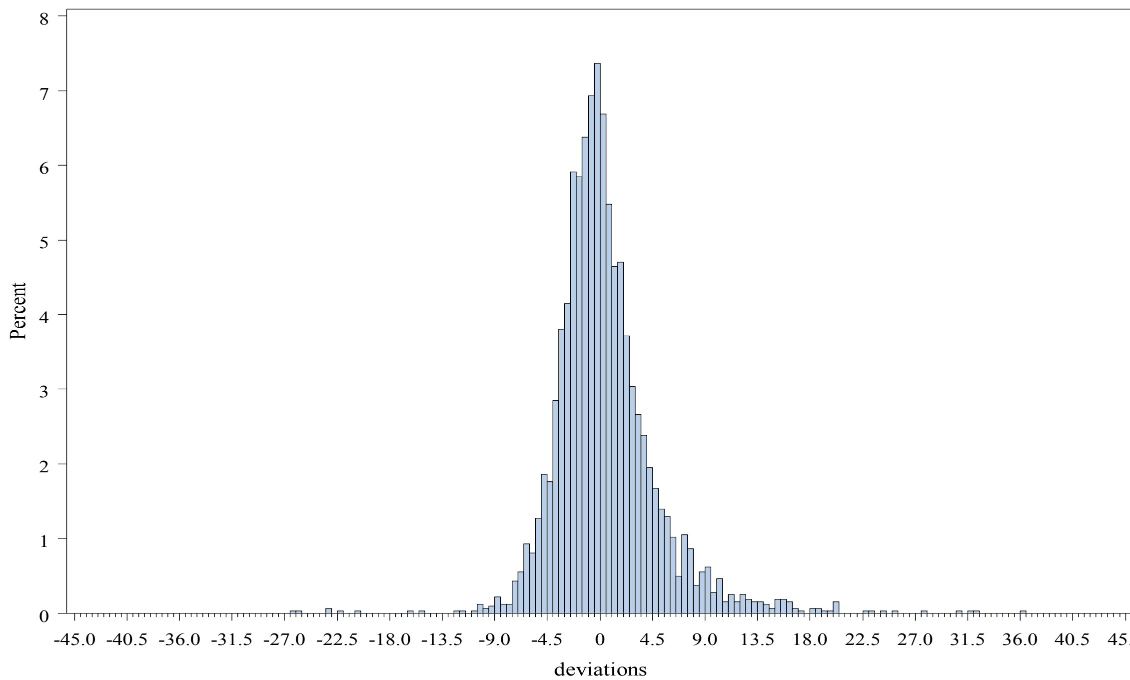

Figure 3.41 Histogram of devRM for LSU, with a mean of 0.4219 and a median of –0.02.

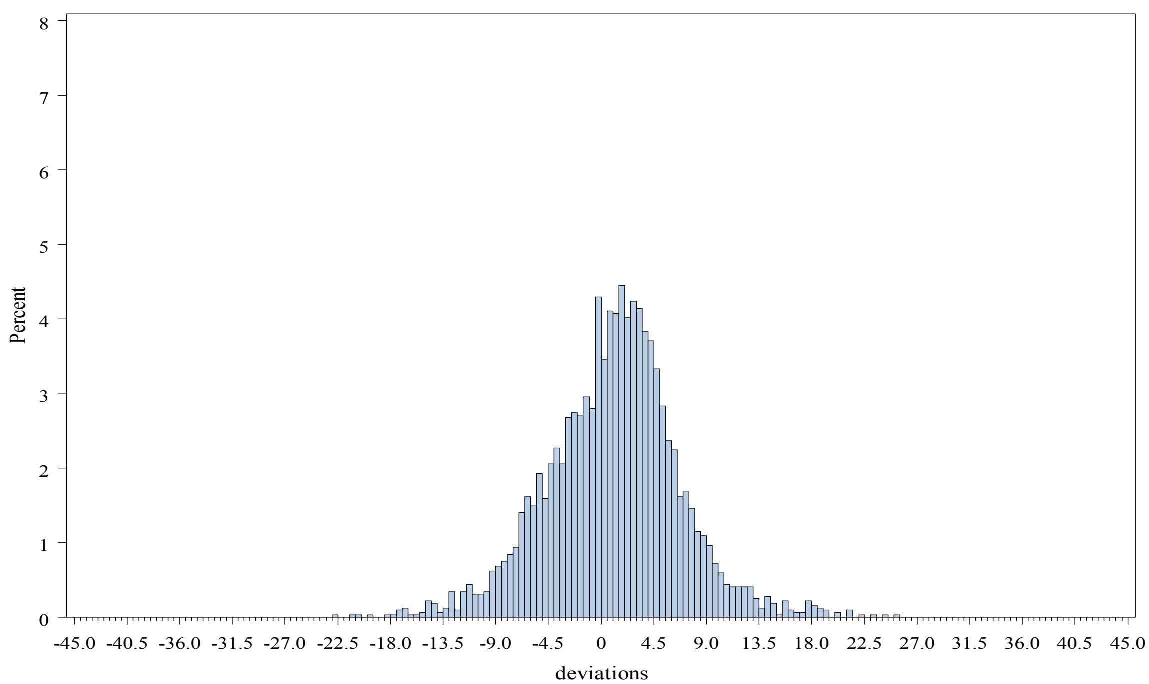

Figure 3.42 Histogram of devRM for New Roads, with a mean of 1.0252 and a median of 1.3.

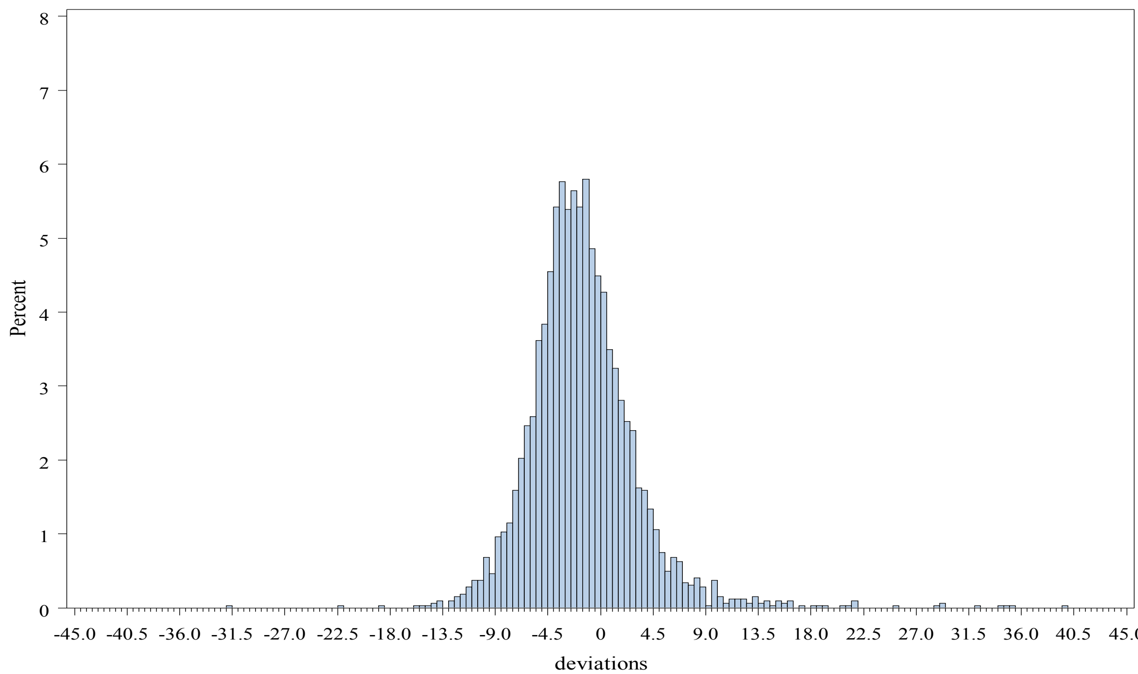

Figure 3.43 Histogram of devRM for Port Allen, with a mean of –1.5617 and a median of –2.0.

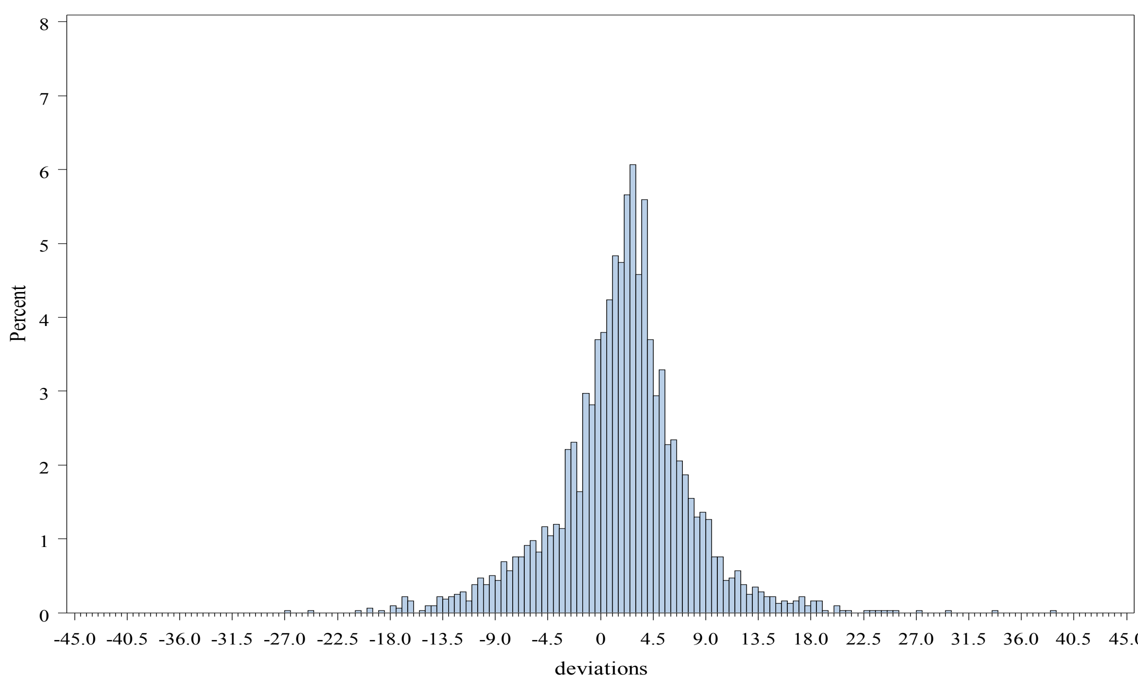

Figure 3.44 Histogram of devRM for Pride, with a mean of 1.8540 and a median of 2.2.

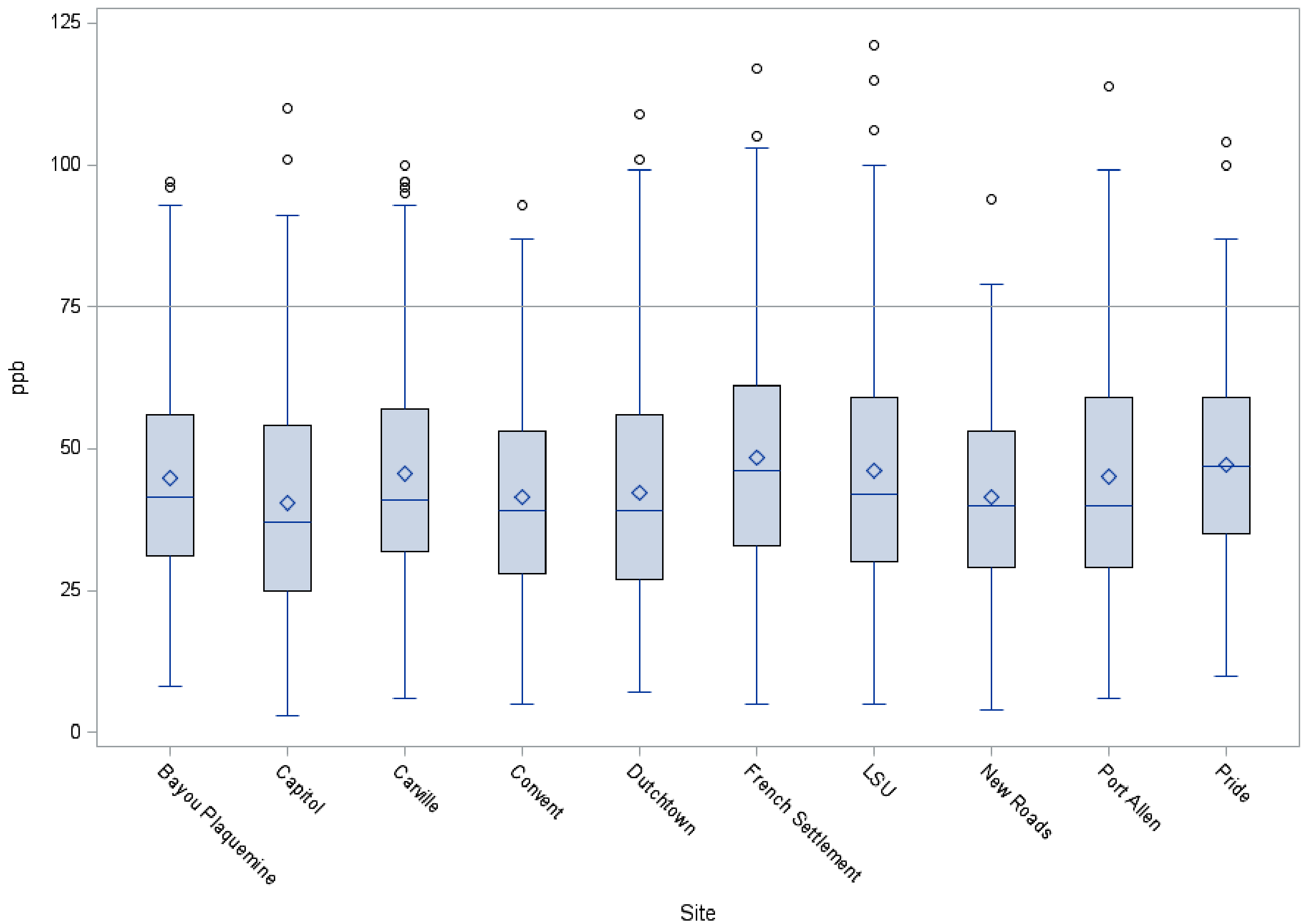

Figure 3.45 Boxplot of DO by site for the year 2000 with reference line at 75 ppb. Whiskers mark the upper and lower fences which are equal to 1.5 times the interquartile range above and below the 3rd and 1st quartiles.

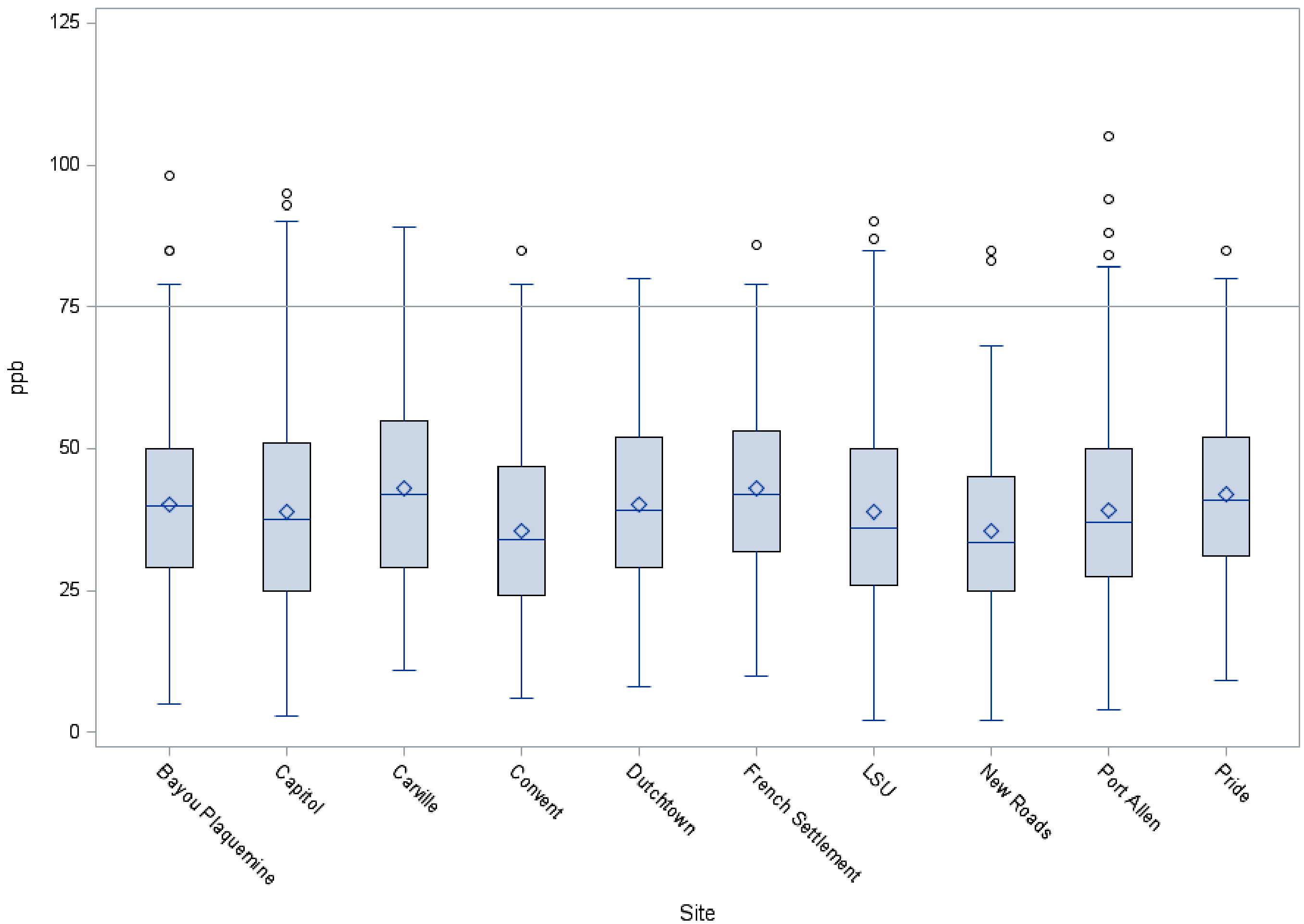

Figure 3.46 Figure 14 Boxplot of DO by site for the year 2001 with reference line at 75 ppb. Whiskers mark the upper and lower fences which are equal to 1.5 times the interquartile range above and below the 3rd and 1st quartiles.

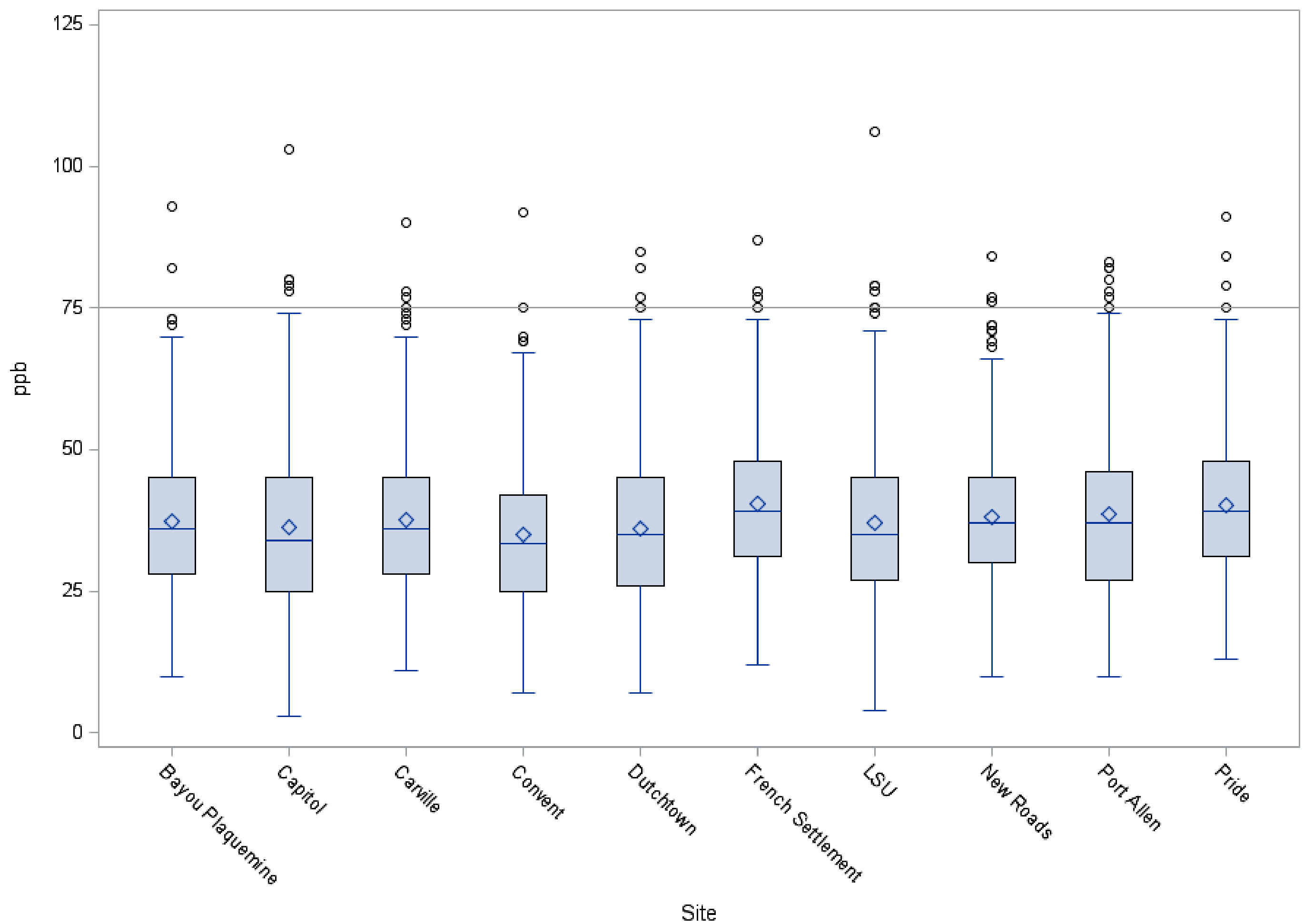

Figure 3.47 Boxplot of DO by site for the year 2002 with reference line at 75 ppb. Whiskers mark the upper and lower fences which are equal to 1.5 times the interquartile range above and below the 3rd and 1st quartiles.

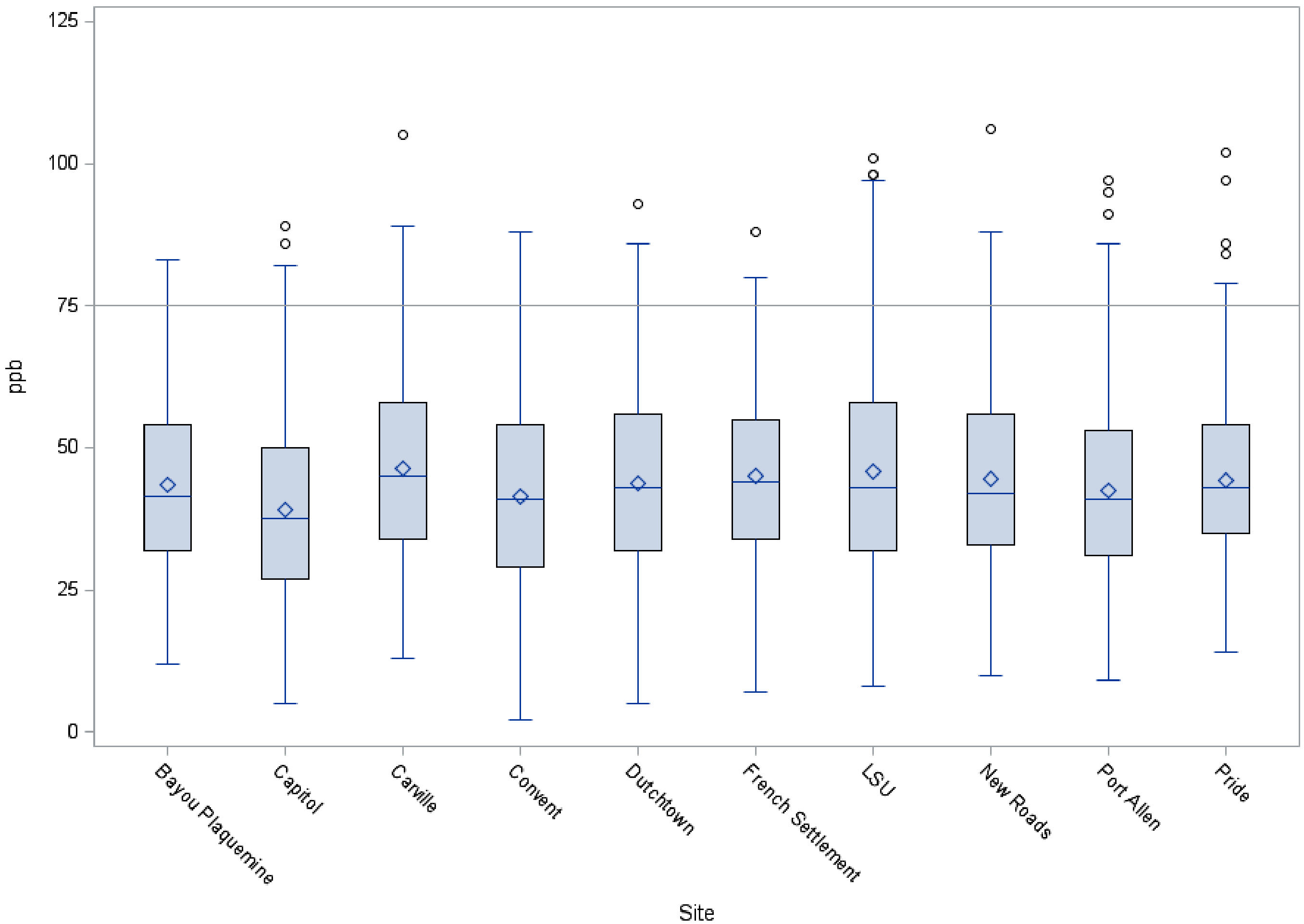

Figure 3.48 Boxplot of DO by site for the year 2005 with reference line at 75 ppb. Whiskers mark the upper and lower fences which are equal to 1.5 times the interquartile range above and below the 3rd and 1st quartiles.

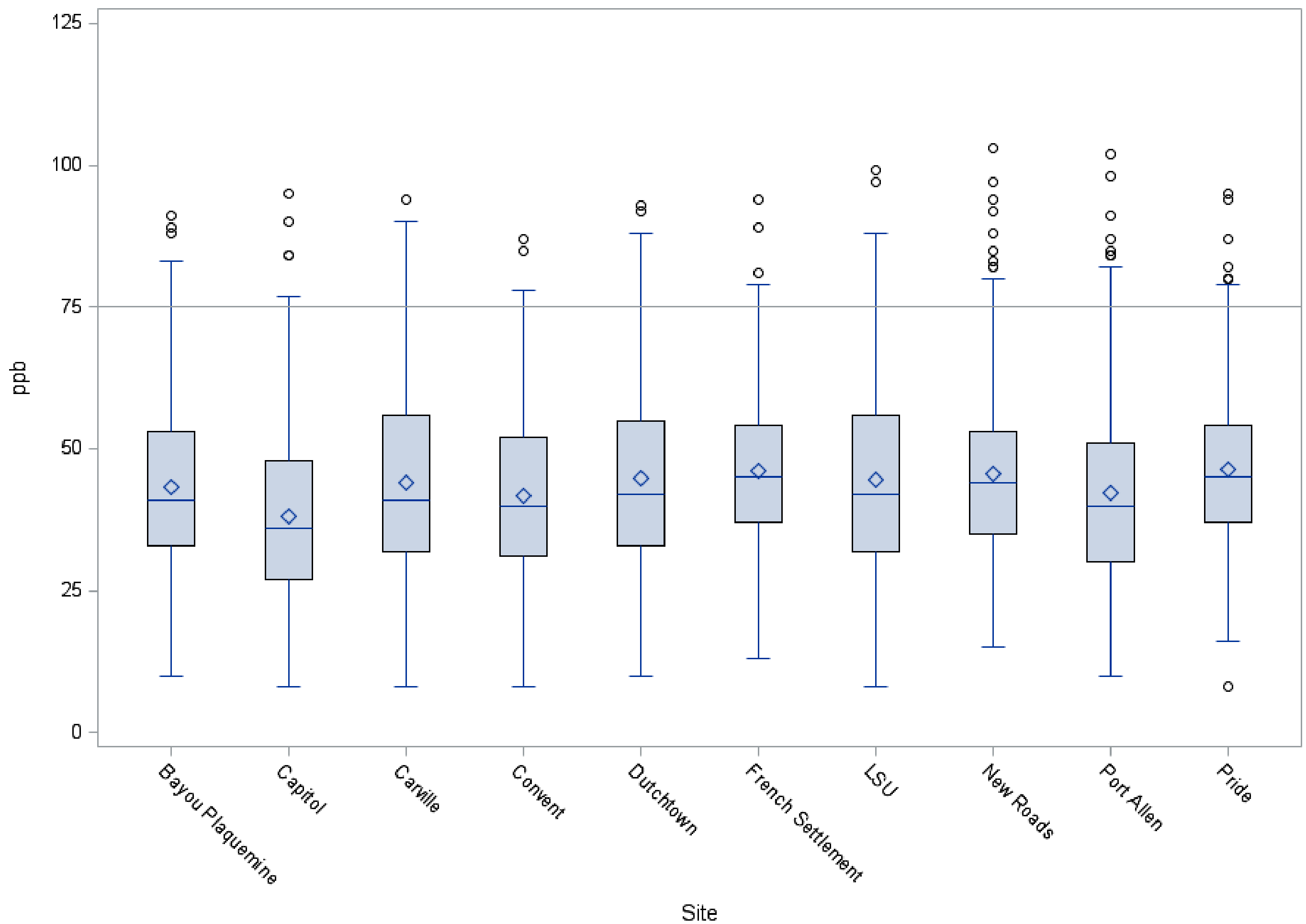

Figure 3.49 Boxplot of DO by site for the year 2006 with reference line at 75 ppb. Whiskers mark the upper and lower fences which are equal to 1.5 times the interquartile range above and below the 3rd and 1st quartiles.

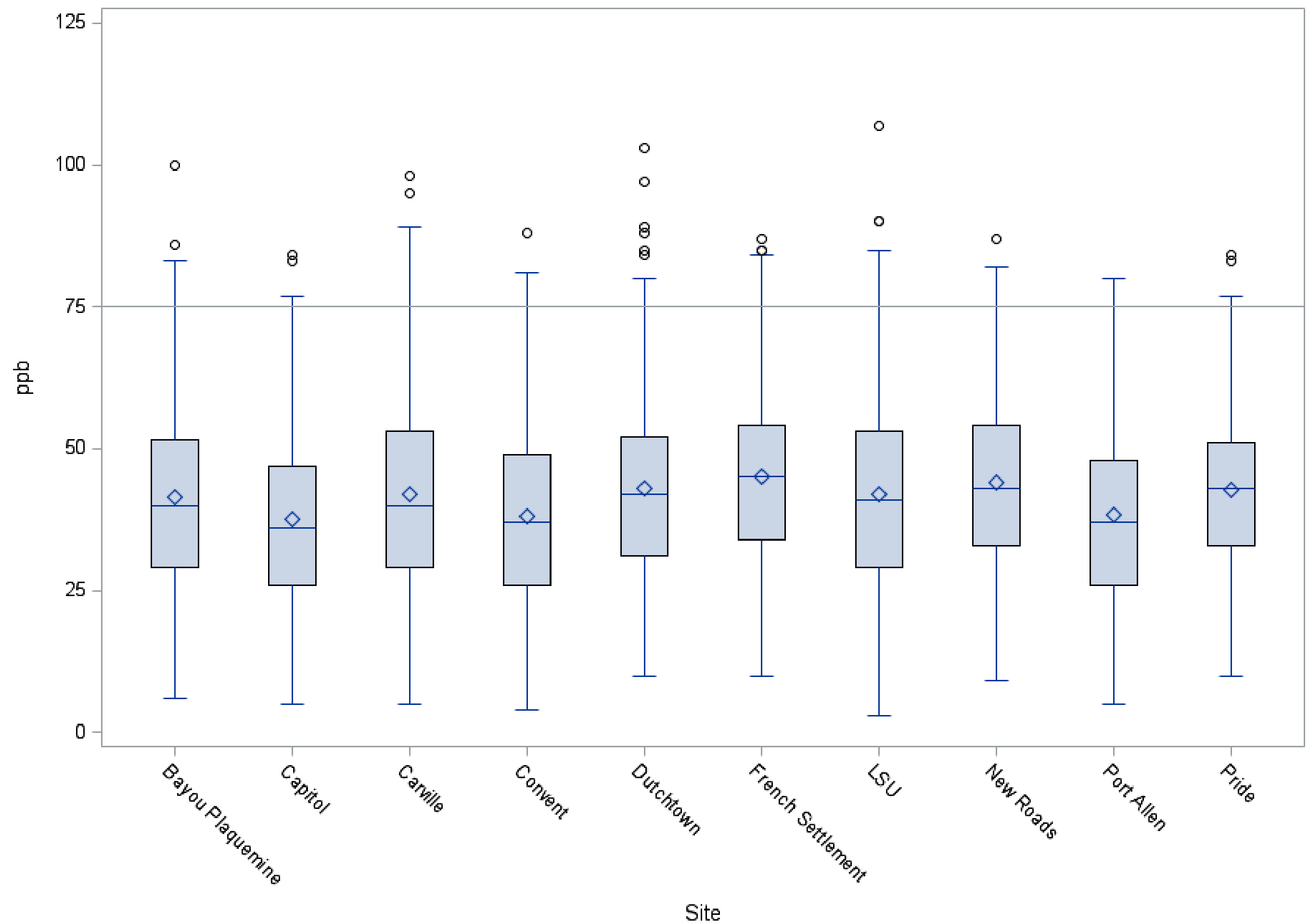

Figure 3.50 Boxplot of DO by site for the year 2007 with reference line at 75 ppb. Whiskers mark the upper and lower fences which are equal to 1.5 times the interquartile range above and below the 3rd and 1st quartiles.

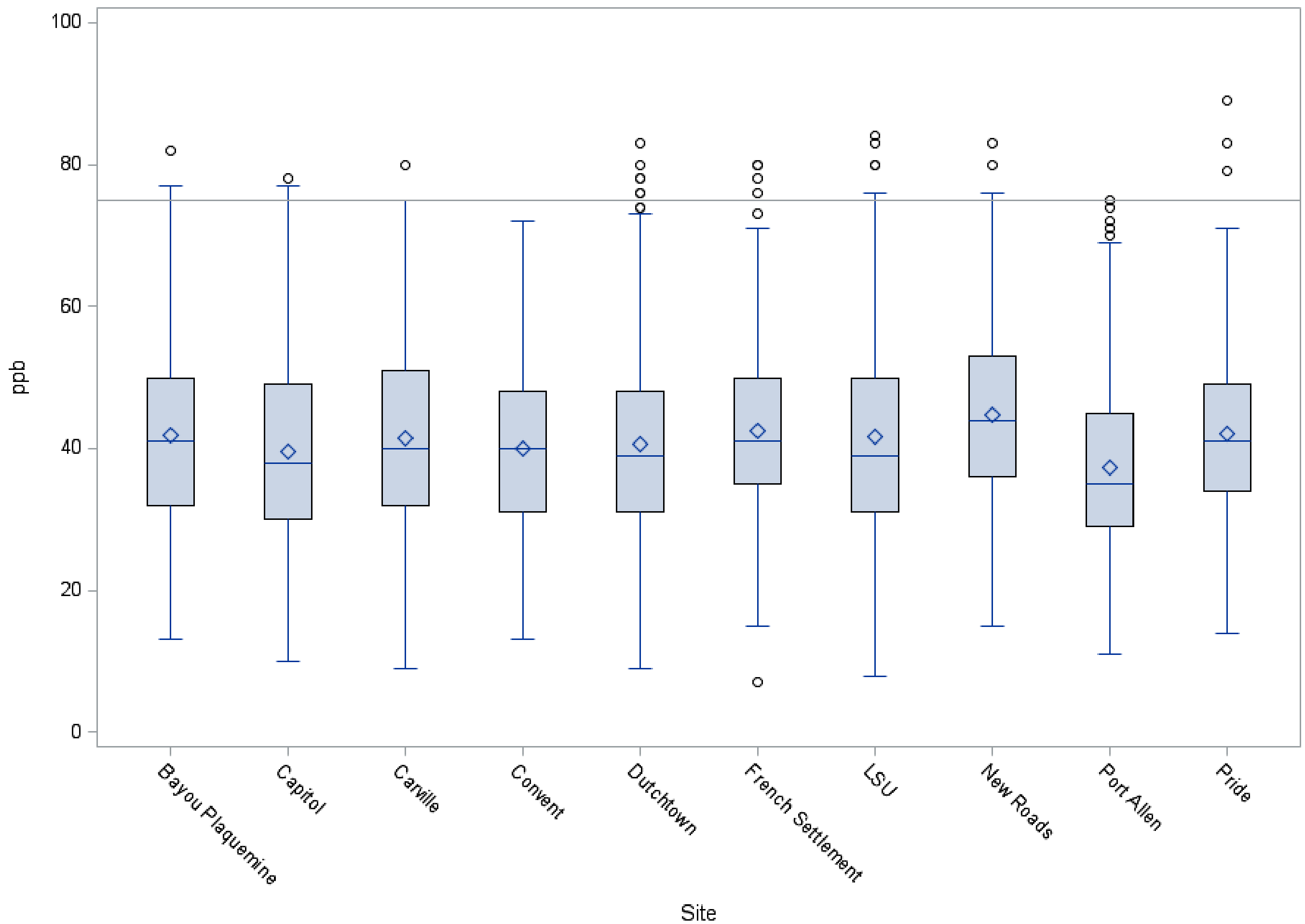

Figure 3.51 Boxplot of DO by site for the year 2010 with reference line at 75 ppb. Whiskers mark the upper and lower fences which are equal to 1.5 times the interquartile range above and below the 3rd and 1st quartiles.

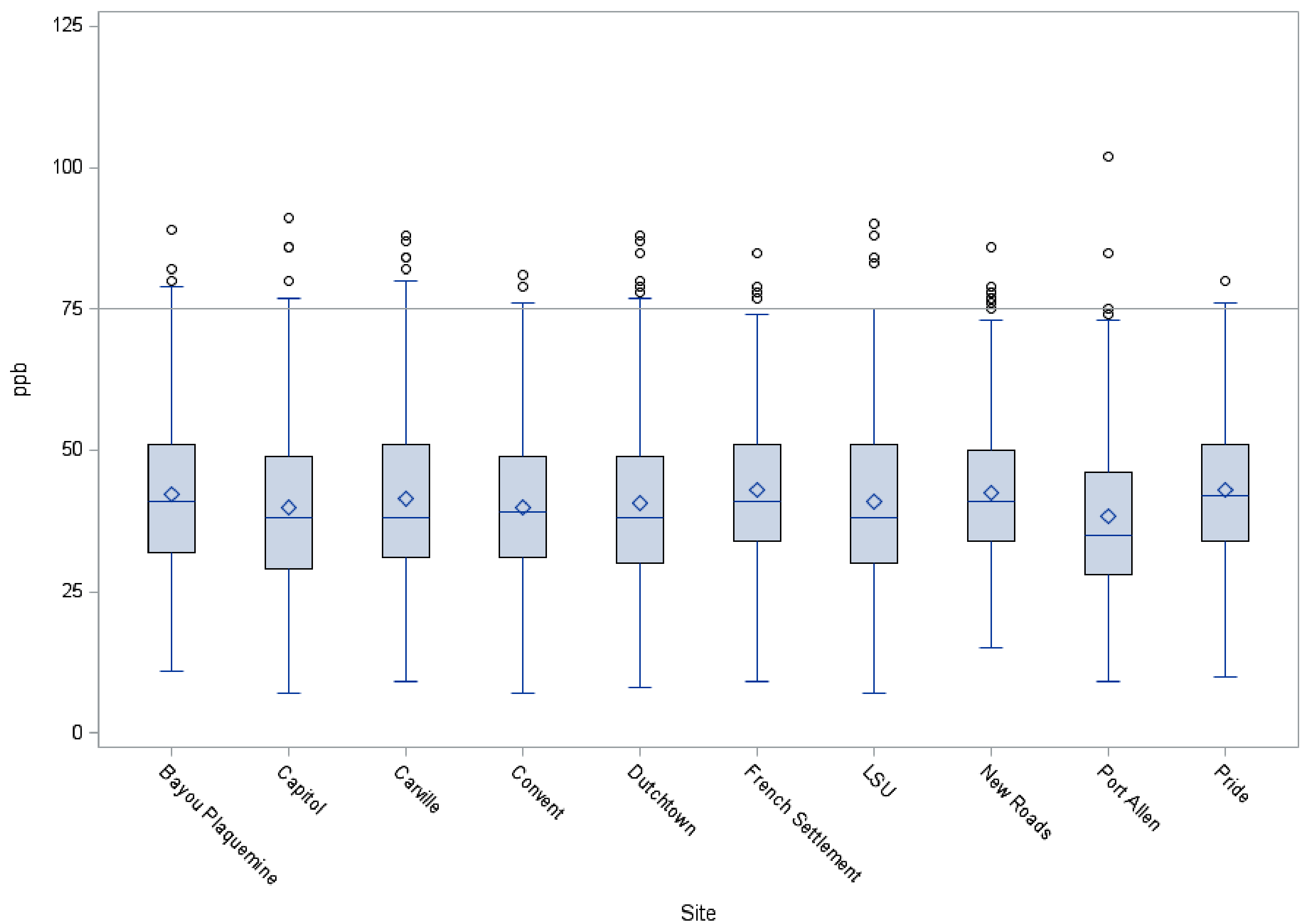

Figure 3.52 Boxplot of DO by site for the year 2011 with reference line at 75 ppb. Whiskers mark the upper and lower fences which are equal to 1.5 times the interquartile range above and below the 3rd and 1st quartiles.

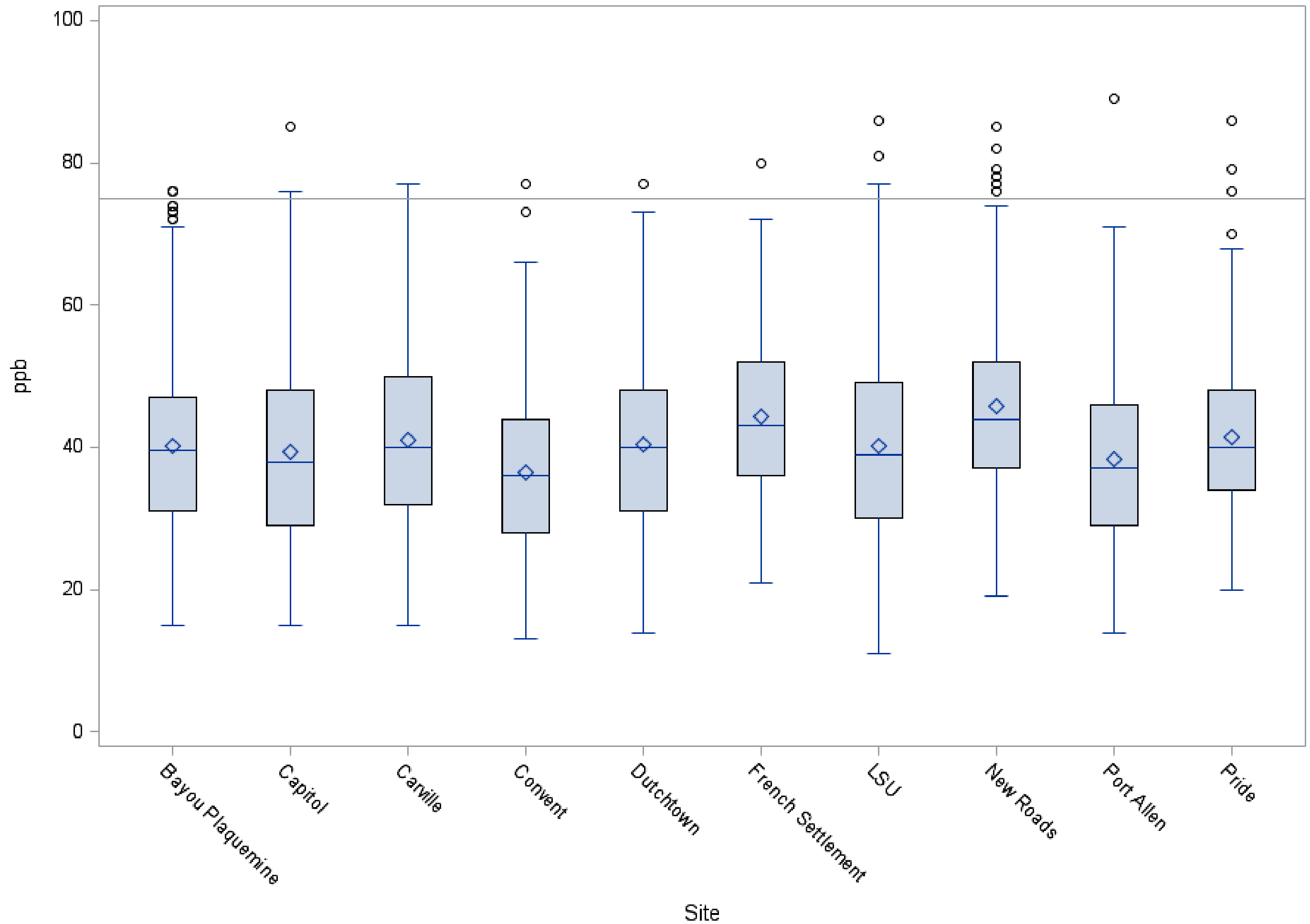

Figure 3.53 Boxplot of DO by site for the year 2012 with reference line at 75 ppb. Whiskers mark the upper and lower fences which are equal to 1.5 times the interquartile range above and below the 3rd and 1st quartiles.

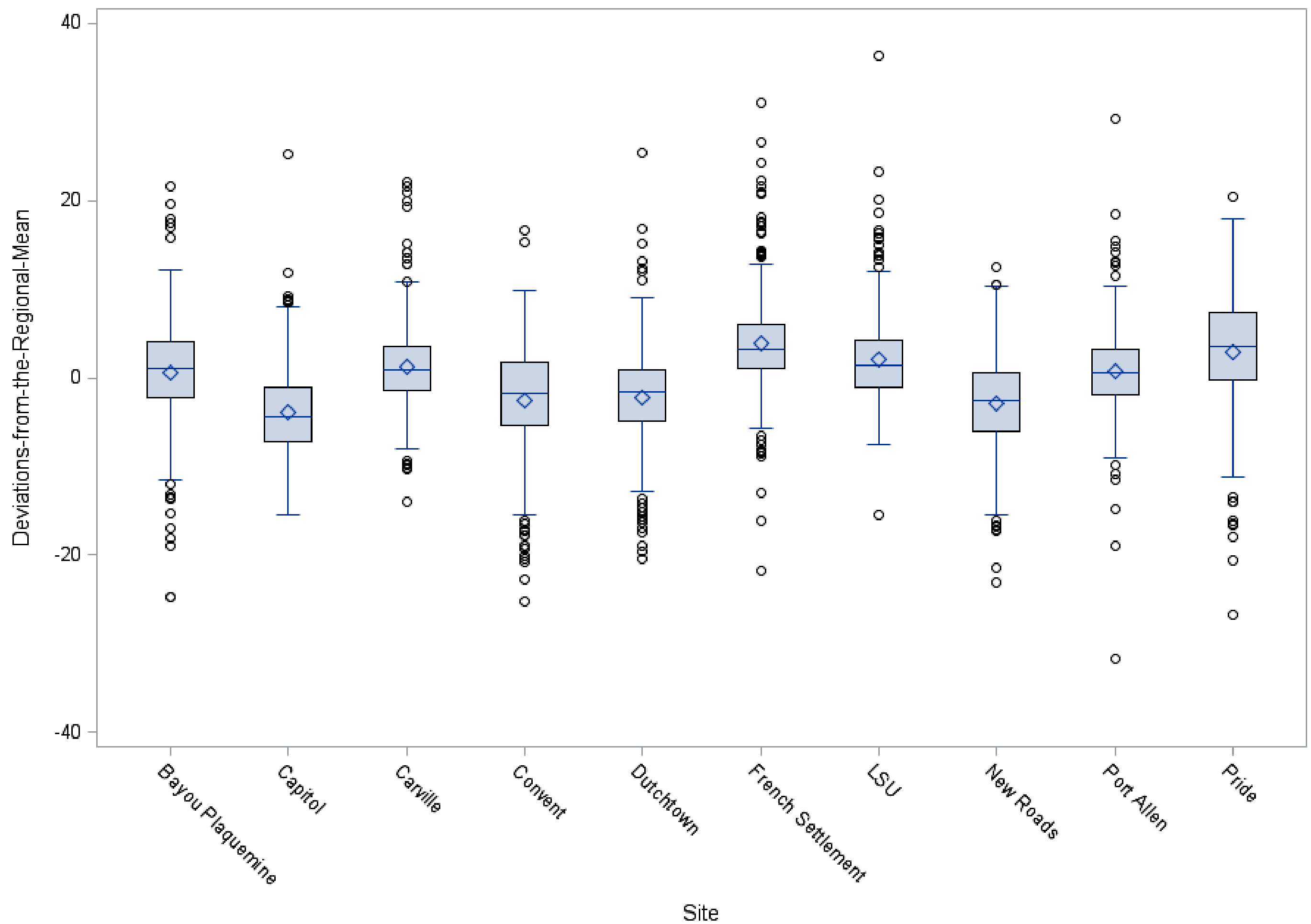

Figure 3.54 Boxplot of devRM by site for the year 2000. Whiskers mark the upper and lower fences which are equal to 1.5 times the interquartile range above and below the 3rd and 1st quartiles.

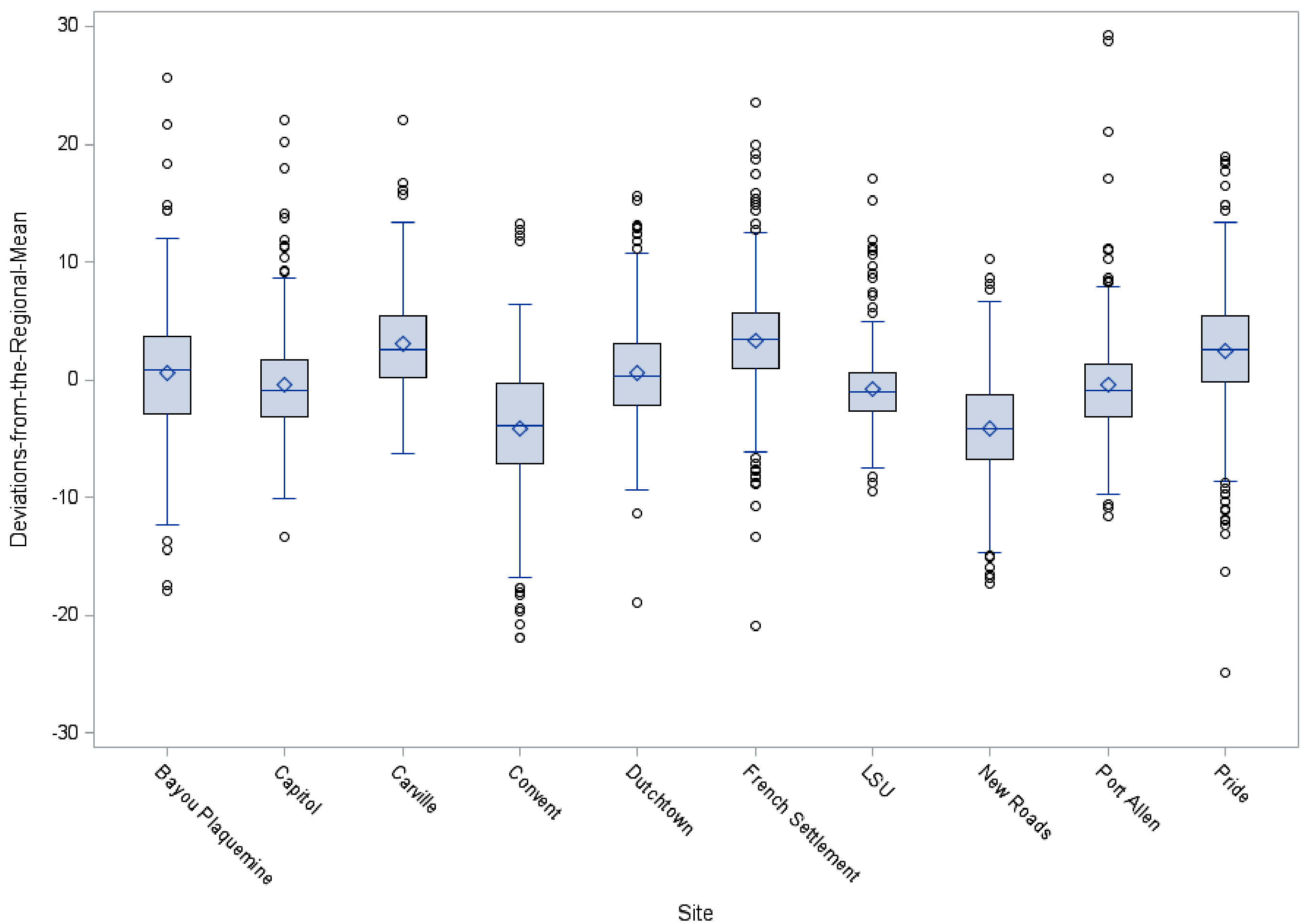

Figure 3.55 Boxplot of devRM by site for the year 2001. Whiskers mark the upper and lower fences which are equal to 1.5 times the interquartile range above and below the 3rd and 1st quartiles.

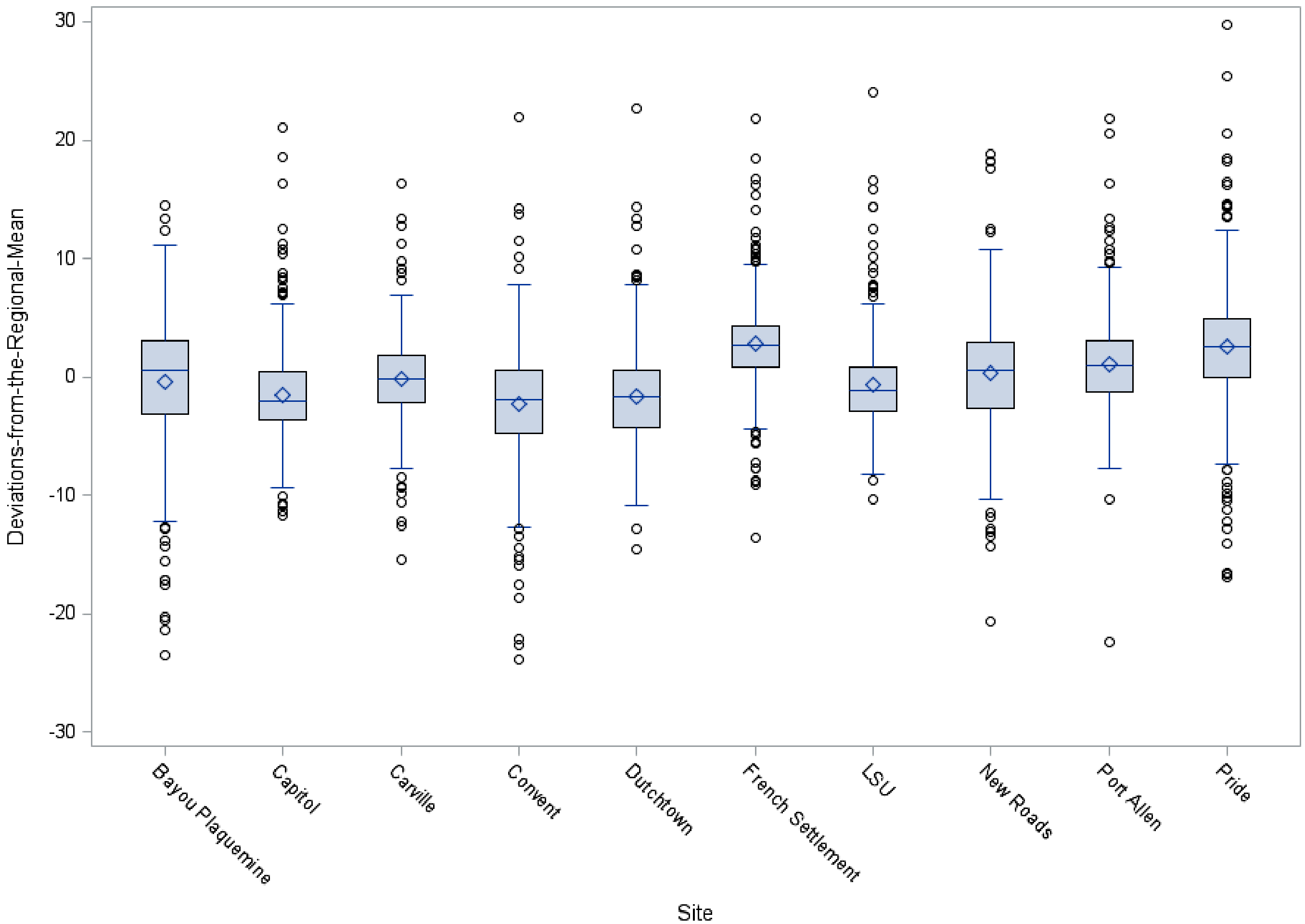

Figure 3.56 Boxplot of devRM by site for the year 2002. Whiskers mark the upper and lower fences which are equal to 1.5 times the interquartile range above and below the 3rd and 1st quartiles.

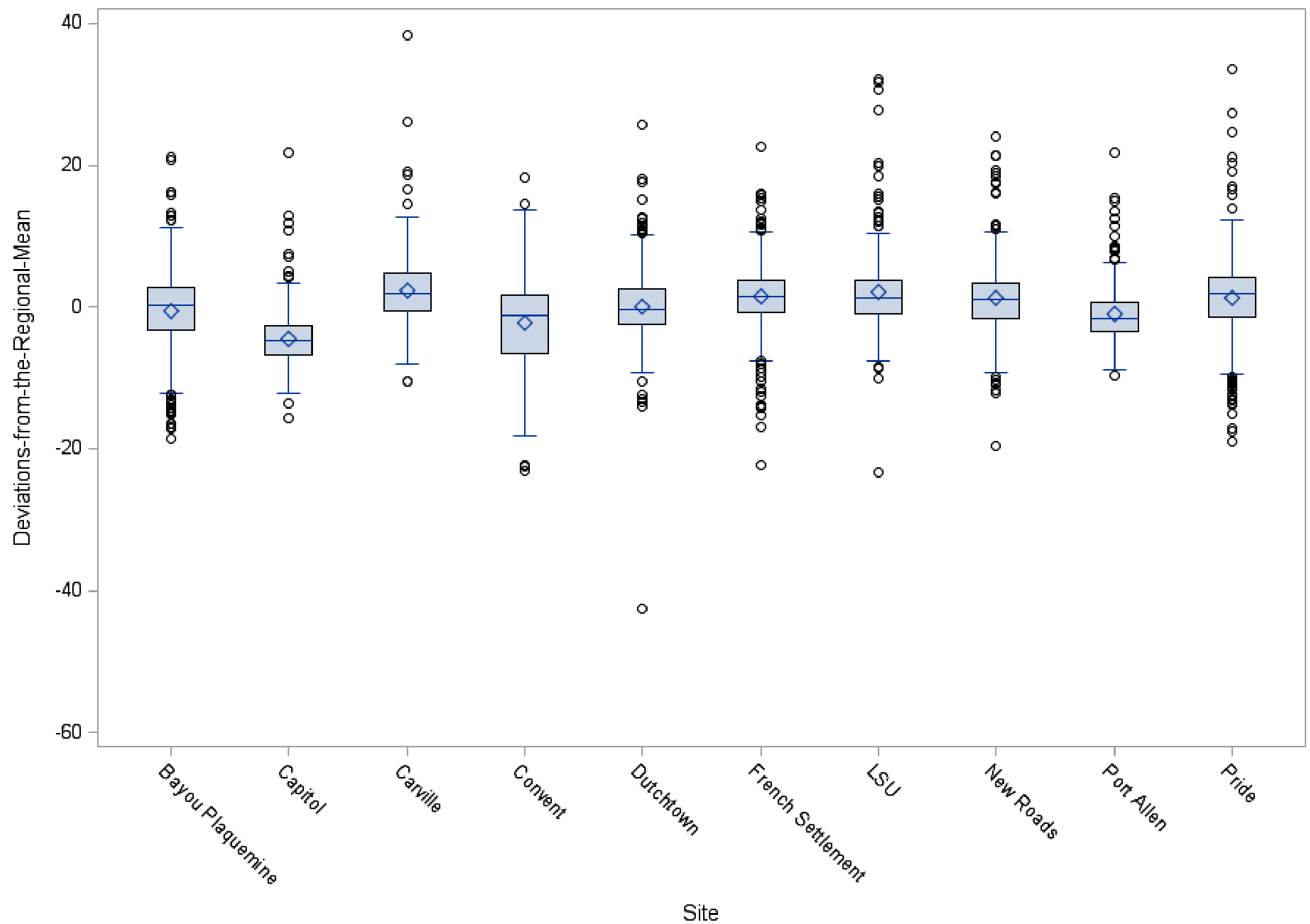

Figure 3.57 Boxplot of devRM by site for the year 2005. Whiskers mark the upper and lower fences which are equal to 1.5 times the interquartile range above and below the 3rd and 1st quartiles.

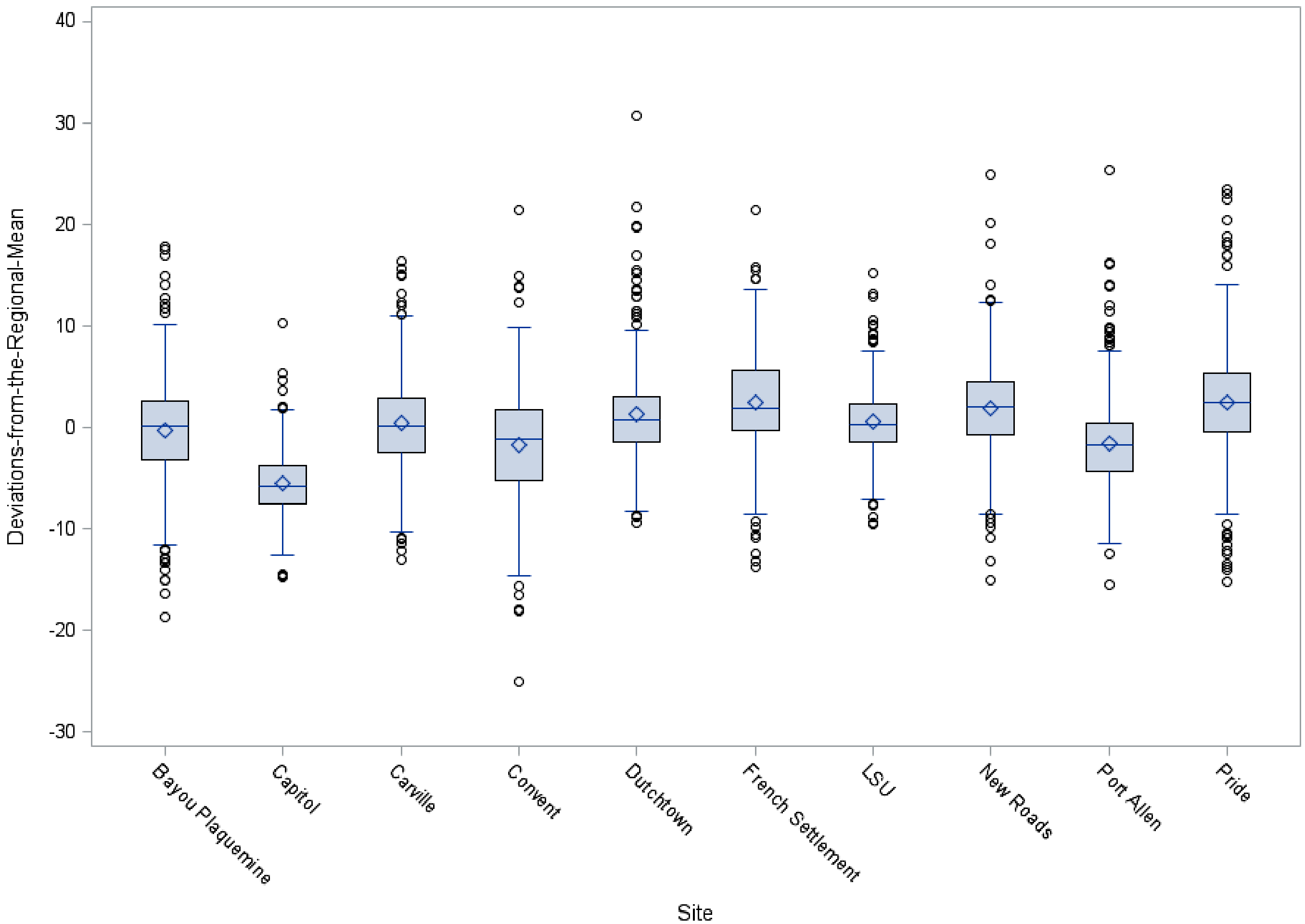

Figure 3.58 Boxplot of devRM by site for the year 2006. Whiskers mark the upper and lower fences which are equal to 1.5 times the interquartile range above and below the 3rd and 1st quartiles.

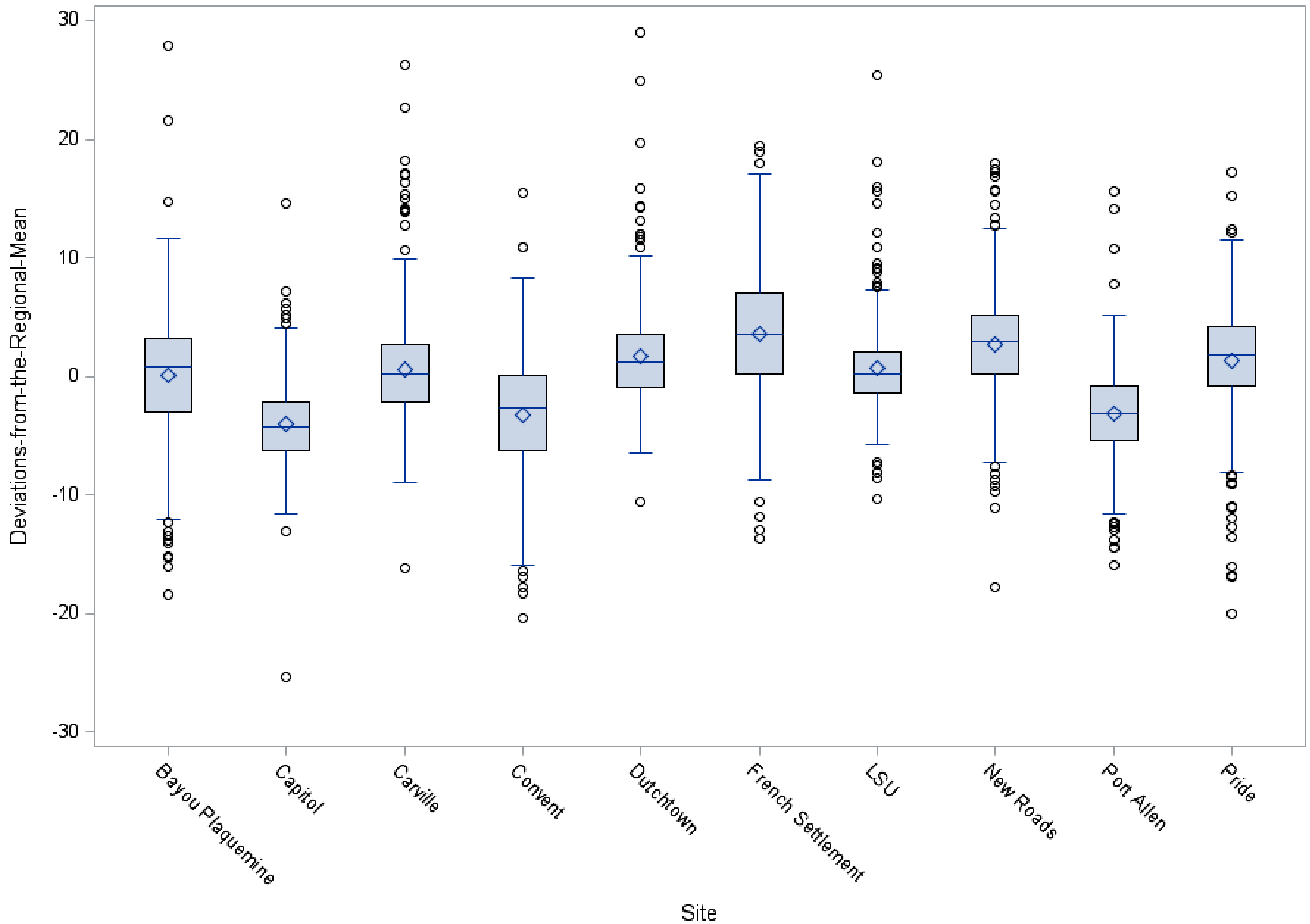

Figure 3.59 Boxplot of devRM by site for the year 2007. Whiskers mark the upper and lower fences which are equal to 1.5 times the interquartile range above and below the 3rd and 1st quartiles.

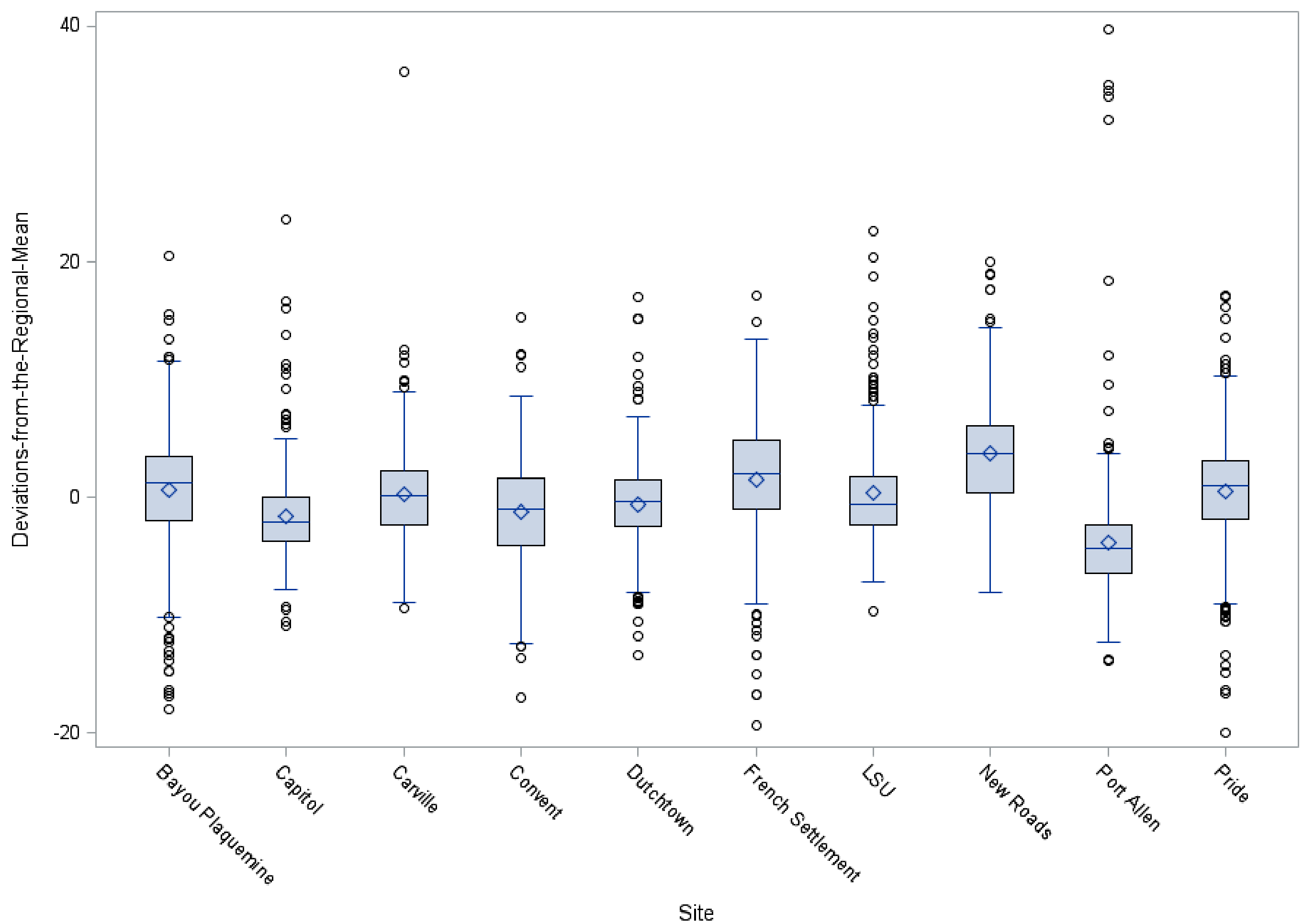

Figure 3.60 Boxplot of devRM by site for the year 2010. Whiskers mark the upper and lower fences which are equal to 1.5 times the interquartile range above and below the 3rd and 1st quartiles.

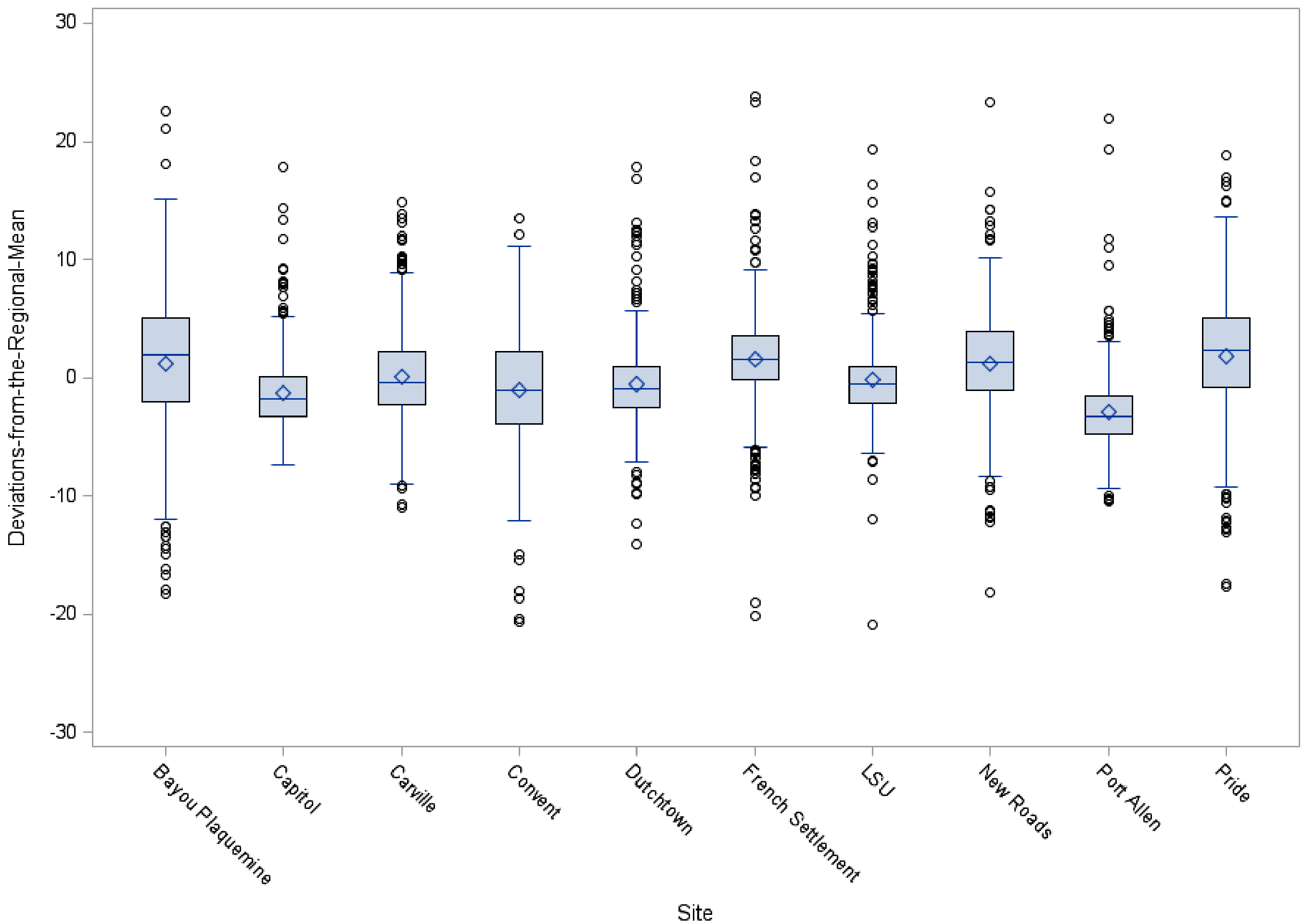

Figure 3.61 Boxplot of devRM by site for the year 2011. Whiskers mark the upper and lower fences which are equal to 1.5 times the interquartile range above and below the 3rd and 1st quartiles.

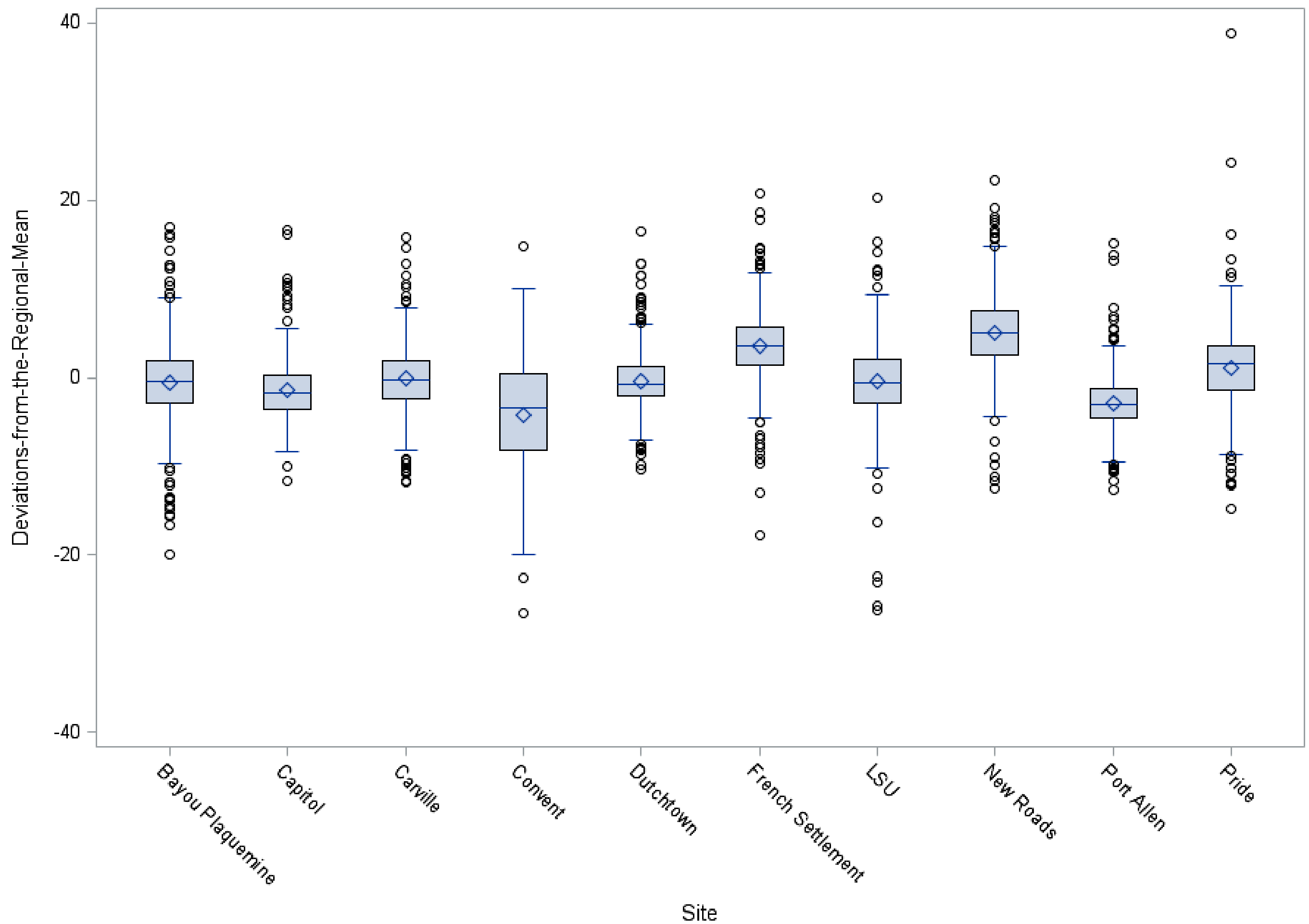

Figure 3.62 Boxplot of devRM by site for the year 2012. Whiskers mark the upper and lower fences which are equal to 1.5 times the interquartile range above and below the 3rd and 1st quartiles.

3.5 Multiple Regression Model Development

LC variables were tested for significance at 95% confidence ($p < 0.05$). The buffer size with the highest adjusted R^2 (Adj R^2) for each LC was identified and entered into the model in a stepwise selection. To enter the model, a predictor must have improved the R^2 value by at least 1%.

The next chapter will detail the results of these analyses.

Chapter 4. Results

4.1 Land Cover Correlation

More predictors are significantly correlated (p-value <0.05) with devRM O_3 data than with DO O_3 data (Figure 4.1), and the overall strength of correlation with LC is greater for devRM data than for DO data. Three temporalities were considered: (A) daily (n=10714), (B) one-year monthly (n=360), and (C) three-year monthly (n=360). Figure 4.2 shows that the longer the averaging period, the greater the overall strength of correlations between LC predictors and O_3.

After removal of the regional mean, each temporality has marked improvement in overall strength of correlations and increase in number of significantly correlated predictors (Figure 4.1 and Figure 4.2). Temporality A increased from 205 significantly correlated predictors to 227; B increased from 111 to 204; and C increased from 110 to 207 significantly correlated predictors. The mean absolute correlation coefficient for A improved from 0.055 to 0.146; B, from 0.133 to 0.286; and C, from 0.132 to 0.306. LC shows greater strength as a predictor for longer averaging periods, indicating again that variables not modeled (e.g. meteorological factors, precursor emissions) are greater contributors than LC to the day-to-day or hour-to-hour fluctuations in O_3 mixing ratios. The performance of LC as predictor variables for B and C, especially the improvement from DO to devRM, suggests that local environments contribute to long-term exposure. Moreover, LC may be impactful perhaps either as a direct emission source or through some indirect relationship such as thermal properties or roughness, both of which may affect the formation and turbulent diffusion of O_3 and/or its precursors.

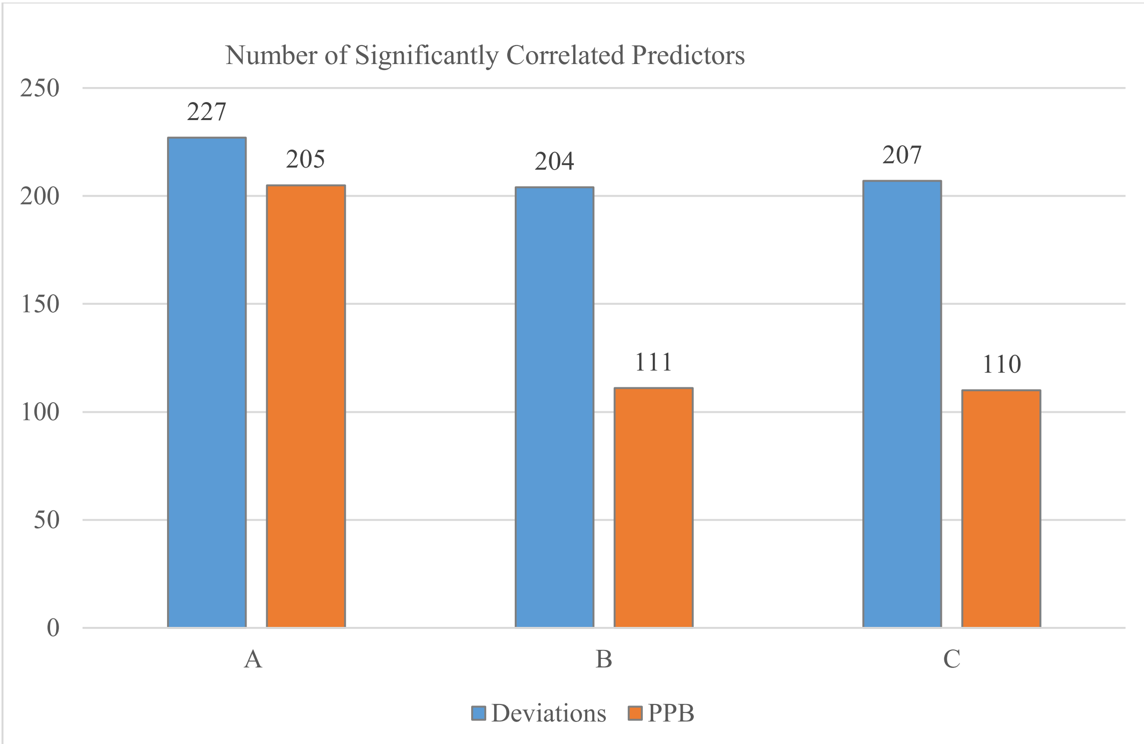

Figure 4.1 Number of correlated candidate predictors for devRM and DO.

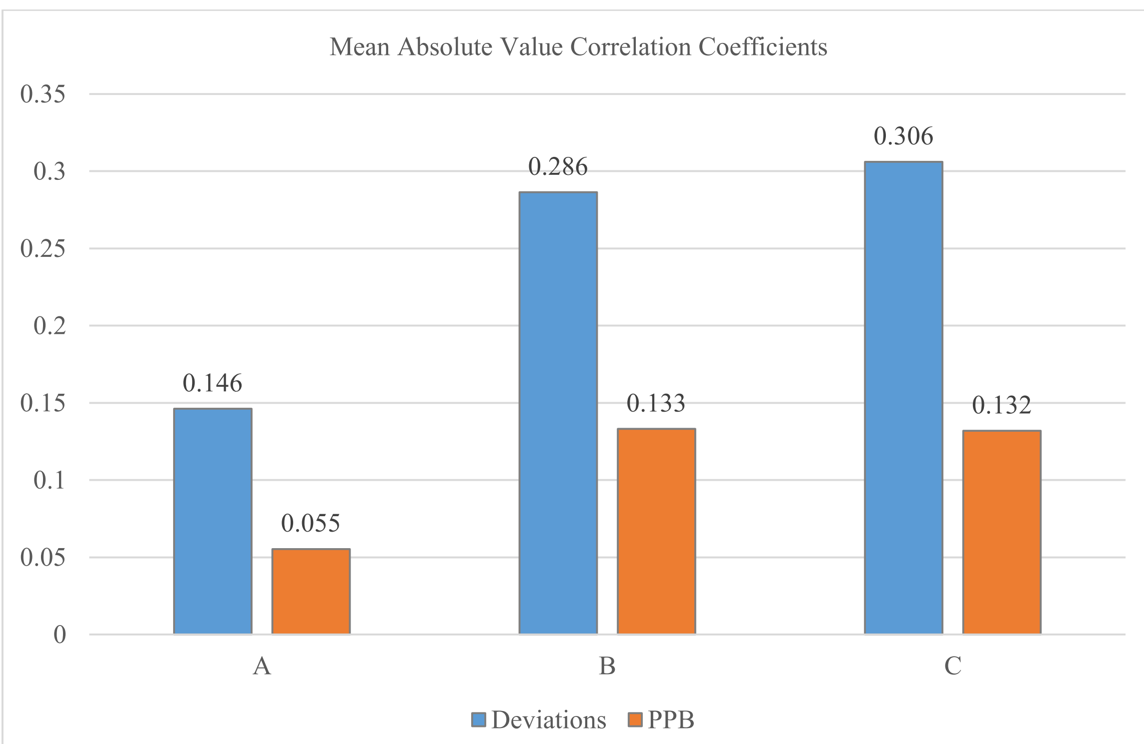

Figure 4.2 Mean absolute values of correlation coefficients for devRM and DO.

Direction of effect – a positive or negative effect on the response variable – was left as a free variable; some studies set a criterion for inclusion in model development requiring that predictors adhere to a predetermined direction based on *a priori* knowledge (Beelen et al. 2013). Direction of effect for correlation coefficients remained consistent for Model B and Model C, and with the exception of grassland/herbaceous (HE), direction did not change among buffer radii within each LC class (Figure 4.3). Generally, biogenic LC classes had positive correlations with devRM while developed classes had negative correlations with devRM (Table 4.1). Because an increase in the density of an LC within a buffer means the exclusion of the other LC types within that buffer, increased density of biogenic classes also means the reduction of developed classes. A change in the NO_x-VOC ratio of direction emissions could follow the change in LC partitioning.

4.2 Regression Analysis

4.2.1 Univariate Regression

A series of univariate regressions reduced the field of candidate predictors to a single buffer for each LC. Table 4.2 shows the buffer size with the greatest Adj R^2 for each LC type for each metric. An "all-in" approach without filtering of candidate predictor variables has the potential for greater explained variance but runs the risk of overfitting the model and of using redundant information when multiple buffers for a LC type enter the model.

The rank of LC types changed little among Metric A, Metric B, and Metric C. Between A and B, crop and open space swapped positions. Hay supplanted herbaceous grassland for the top rank in C with additional changes happening within the shaded groups (Table 4.2). Evergreen (EV) and water WA) were consistently ranked third and fourth while woody wetland (WW),

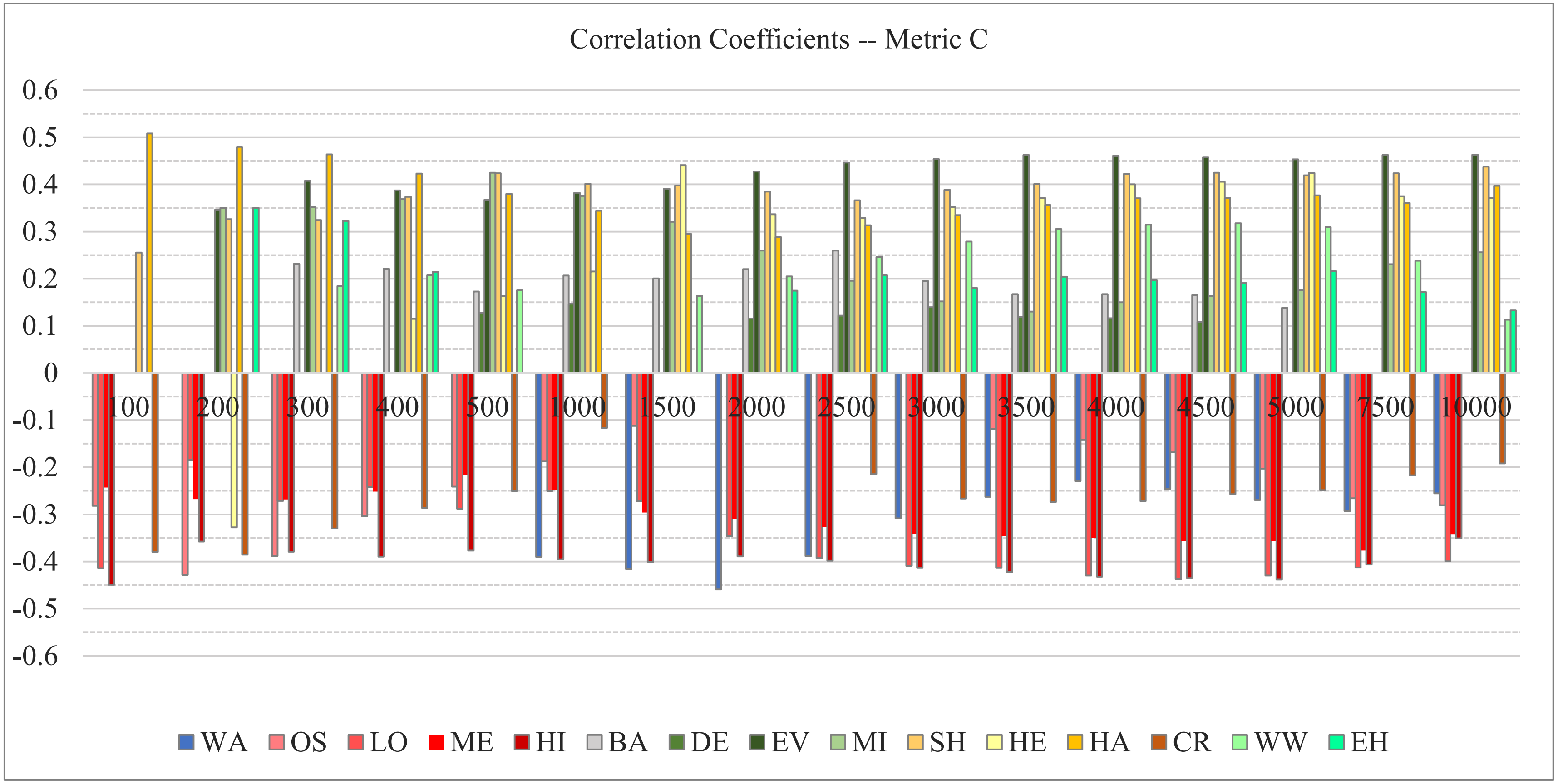

Figure 4.3 Correlation coefficients for LC classes by buffer radius.

Table 4.1 Direction of effect for land cover type.

Code	WA	OS	LO	ME	HI	BA	DE	EV	MI	SH	HE	HA	CR	WW	EH
Direction	(–)	(–)	(–)	(–)	(–)	(+)	(+)	(+)	(+)	(+)	(+)	(+)	(–)	(+)	(+)

Table 4.2 Ranked buffer sizes and land cover types for each response variable.

	A			B			C		
Rank	Adj R^2	LC Type	Buffer	Adj R^2	LC Type	Buffer	Adj R^2	LC Type	Buffer
1	0.0578	HE	1500	0.1835	HE	1500	0.2559	HA	100
2	0.0560	EV	4500	0.1791	EV	4500	0.2122	EV	10000
3	0.0550	WA	2000	0.1779	WA	2000	0.2087	WA	2000
4	0.0544	LO	100	0.1757	LO	100	0.1995	HI	100
5	0.0532	HA	100	0.1725	HE	100	0.1919	HE	1500
6	0.0507	SH	4500	0.1620	SH	4500	0.1895	LO	4500
7	0.0468	HI	100	0.1492	HI	100	0.1894	SH	10000
8	0.0354	ME	7500	0.1131	ME	7500	0.1811	OS	200
9	0.0347	CR	200	0.1122	OS	300	0.1780	MI	500
10	0.0345	OS	300	0.1103	CR	100	0.1463	CR	200
11	0.0336	MI	500	0.1074	MI	500	0.1394	ME	7500
12	0.0290	WW	400	0.0917	WW	400	0.1203	EH	200
13	0.0256	EH	200	0.0836	EH	200	0.0982	WW	4500
14	0.0203	BA	300	0.0629	BA	300	0.0649	BA	2500
15	0.0068	DE	2500	0.0199	DE	2500	0.0189	DE	1000

Ranked buffer size with the highest Adj R^2 per LC type for daily devRM for LC edition years (A), monthly mean of daily devRM for LC edition years (B), and the monthly mean of daily devRM for the three 3-year periods (C).

emergent herbaceous wetland (EH), barren (BA), and deciduous (DE) LCs occupied the bottom four positions. Developed classes and variegated biogenic classes (mixed forest (MI) and shrub/scrub (SH)) remained in the middle of the pack.

4.2.2 Multiple Regression

Results of the univariate regressions informed a stepwise selection. Table 4.3 shows the results of the stepwise selection.

Table 4.3 Stepwise selection regression models.

Model A:	–8.2616 – 61.0504 * he01500 + 74.6579 * ev04500 + 11.7719 * ha00100 – 42.9699 sh04500 – 22.7764 * hi00100 + 66.6467 * me07500 + 6.5643 * cr00200 + 14.1712 * ww00400 + 100.6700 * de02500
Model B:	–2.0950 + 46.3469 * he1500 17.6080 * ev4500 + 2.8860 * ha0100 – 12.8654 * hi100 + 17.2481 * me7500
Model C:	–0.9648 + 3.0209 * ha0100 + 17.9599 * ev10000 – 18.6309 * hi0100 – 14.2063 * lo04500 + 41.3818 * me07500

Predictors in the stepwise selection model, particularly LO, ME, and HI, were correlated (Table 4.4). Variance inflation factors (VIFs) were examined to control for the danger of having too much correlation among predictors, or multicollinearity. A large VIF is often used as a sign of multicollinearity, which can limit the conclusions that can be drawn from the regression coefficients about the contribution of each covariate (Zainodin and Yap 2013) and influence

Table 4.4 Correlation matrix of the predictors Model C.

Pearson Correlation Coefficients, N=360					
	HA00100	EV10000	HI00100	ME07500	LO04500
HA00100	1.0000	0.4762 <.0001	-0.4964 <.0001	-0.7282 <.0001	-0.7991 <.0001
EV10000	0.4762 <.0001	1.0000	-0.2576 <.0001	-0.3921 <.0001	-0.4824 <.0001
HI00100	-0.4964 <.0001	-0.25764 <.0001	1.0000	0.7879 <.0001	0.6444 <.0001
ME07500	-0.7282 <.0001	-0.3921 <.0001	0.7879 <.0001	1.0000	0.9313 <.0001
LO04500	-0.7991 <.0001	-0.4824 <.0001	0.6444 <.0001	0.9313 <.0001	1.0000

predictions that are outside the training data. To reduce model redundancy, any predictor with a VIF greater than 5 was removed, resulting in the elimination of the developed–medium (ME) and shrub/scrub (SH) predictors from Model A. ME was removed from Model B and developed – low (LO) was removed from Model C. Additionally, deciduous forest (DE) was removed from Model A due to non-significance. The final models and parameter estimates are in Table 4.5.

Next, the models were evaluated for normality, and for fit using the Adj R^2, the root mean square error (RMSE), and plots of the residuals. Model C achieved the greatest Adj R^2 value at 0.0.4204, with a RMSE of 1.95618. Model B had an Adj R^2 of 0.2905 and a RMSE of 2.35759. For Model A the Adj R^2 is 0.0956, and a RMSE of 4.90205. Model A did not pass a modified Kolmogorov-Smirnov normality test conducted in SAS 9.4 (Figure 4.4; Table 4.6). For samples with fewer than 2000 observations, SAS 9.4 outputs the Shapiro-Wilk statistic. Models B (Figure 4.5; Table 4.7) and C (Figure 4.6; Table 4.8) passed the Shapiro-Wilk test for normality.

Table 4.5 Final regression models.

Model A:	–0.4433 + 0.4543 * he01500 + 0.189 * ev04500 + 0.0076 * ha00100 – 0.0736 * hi00100 – cr00200 * 0.0179 – 0.0197 * ww00400
Model B:	–1.0184 + 0.3861 * he01500 + 0.1782 * ev04500 + 0.0145 * ha00100 – 0.0631 * hi 00100
Model C:	–1.9325 + 0.0387 * ha00100 + 0.2106 * ev10000 – 0.1576 * hi00100 + 0.2121 * me07500

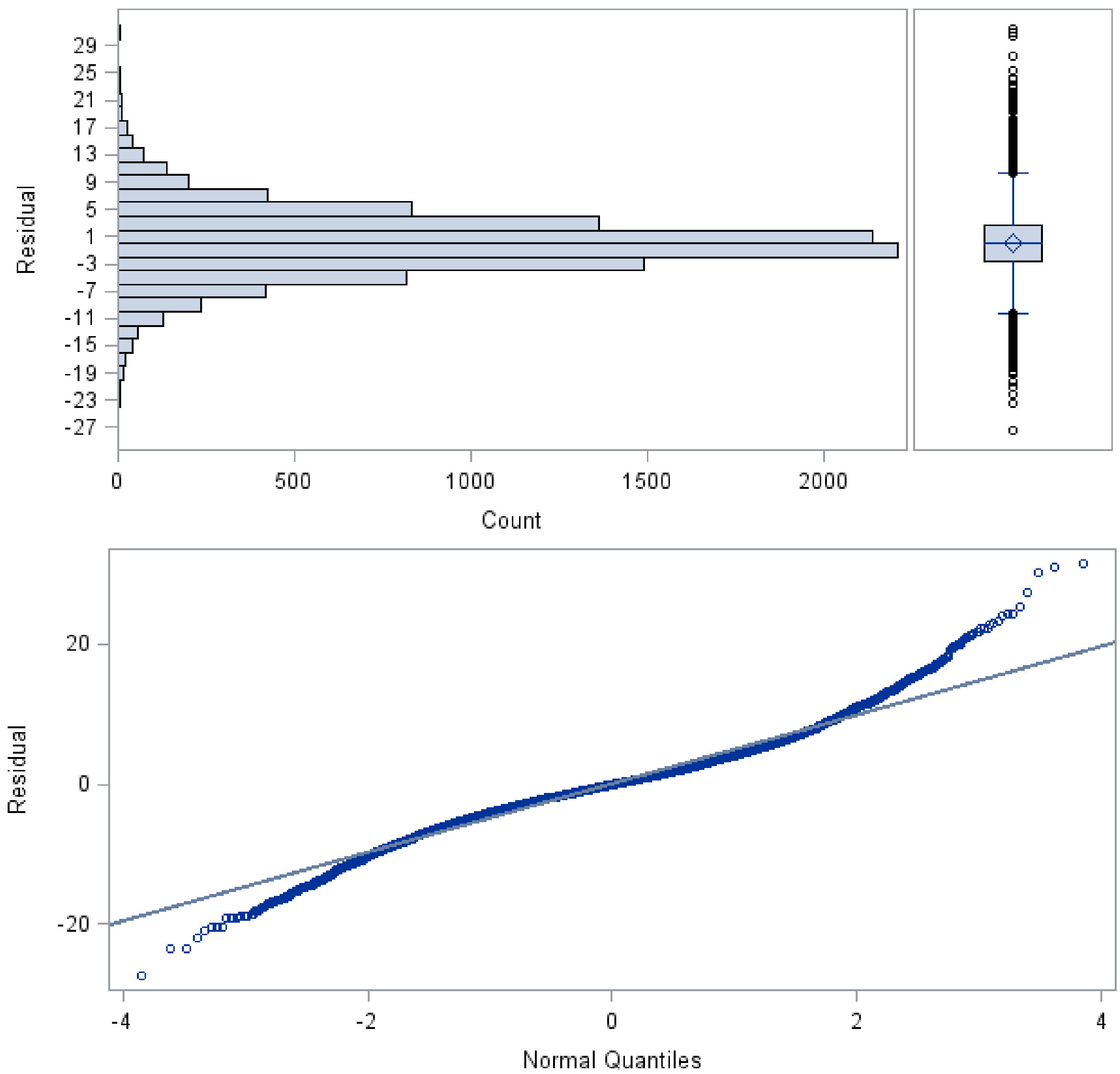

Figure 4.4 Model A fit diagnostics for regression analysis of daily devRM.

Table 4.6 Normality test result for daily O_3 devRM.

Tests for Normality				
Test	Statistic		p Value	
Kolmogorov-Smirnov	D	0.05287	Pr > D	<0.0100

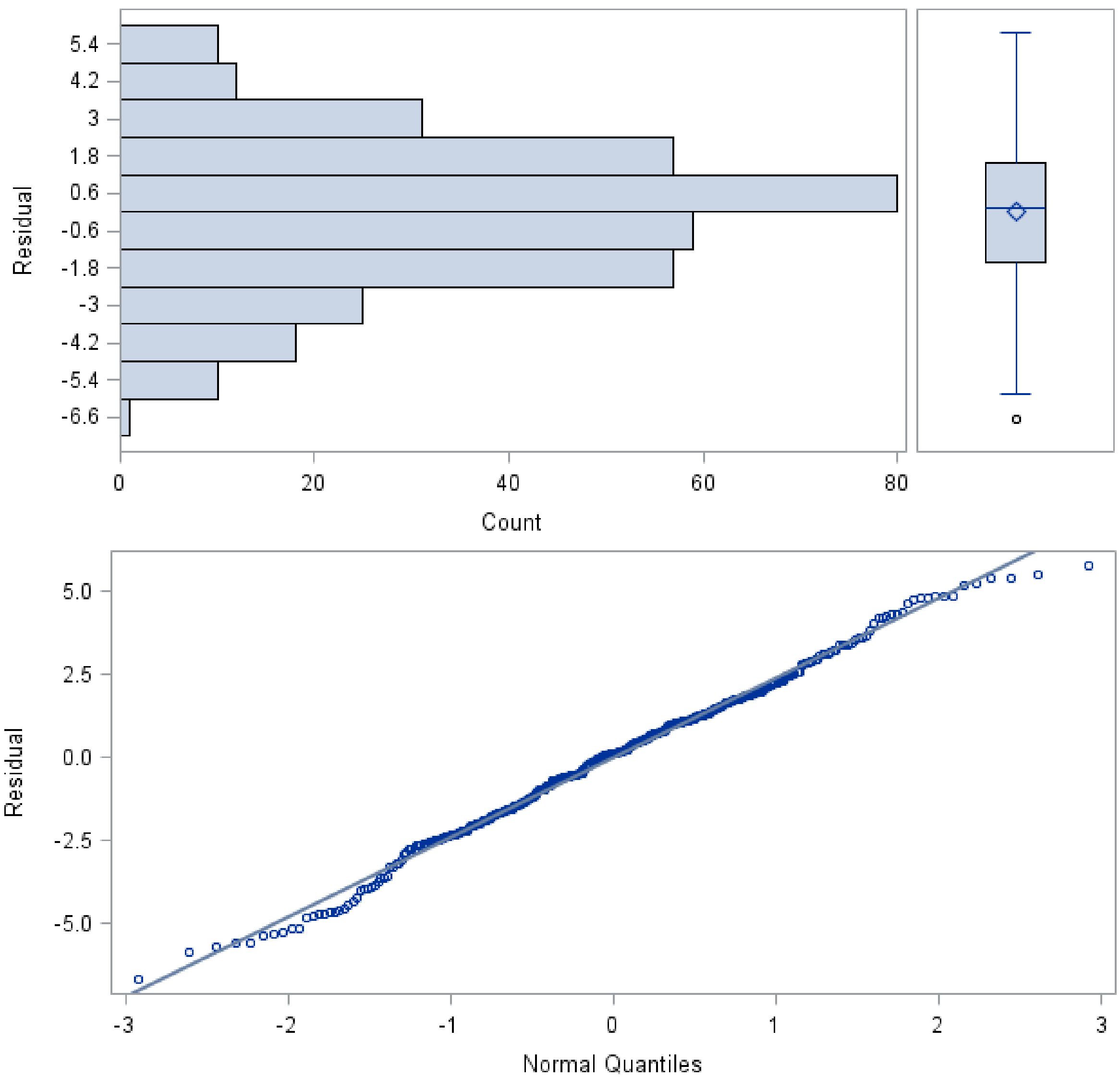

Figure 4.5 Model B fit diagnostics for regression analysis of mean monthly devRM.

Table 4.7 Normality test result for monthly O_3 devRM.

Tests for Normality				
Test	Statistic		p Value	
Shapiro-Wilk	W	0.993877	Pr > W	<0.1555

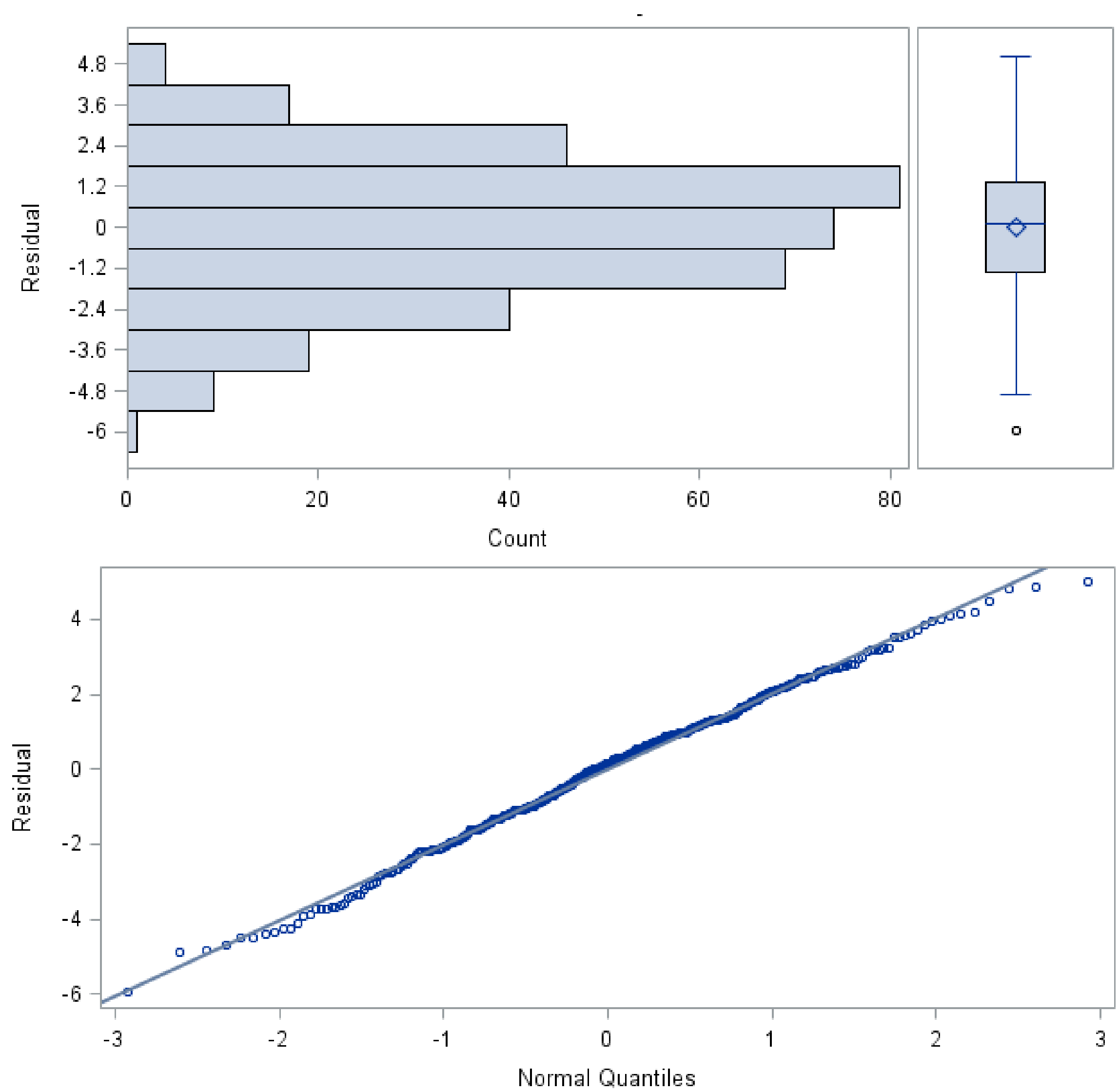

Figure 4.6 Model C fit diagnostics for regression analysis of mean monthly devRM by period.

Table 4.8 Normality test results for period O_3 devRM.

Tests for Normality				
Test	Statistic		p Value	
Shapiro-Wilk	W	0.993094	Pr > W	<0.0971

Given the poor performance and lack of normality in the residuals, Model A was excluded from further analysis. The predictive abilities of the model were also evaluated using the prediction sum of squares (PRESS) statistics, equivalent to "leave one out" cross validation (LOOCV), and RMSEs (Table 4.9). Both models exhibit variance in the tails. Because Model C achieved both a lower RMSE and PRESS than Model B, Model C was used to produce a surface.

Spatial autocorrelation analysis with Moran's I (Wang et al. 2015) and Geary's C (Shaker et al. 2010) revealed no spatial autocorrelation in the residuals of Model C despite the mean devRM having statistically significant spatial autocorrelation by Moran's I and Geary's C indicating that the LC model was able to capture the spatial nature of O_3. Because residuals showed no spatial autocorrelation, a regression-only approach is appropriate.

The 3-year monthly regional mean explains 83.68% of variance in the O_3 data for period C with an RMSE of 2.4293. When summed with the predicted devRM, explained variance increases to 91.25% and the RMSE is 1.7790. For all periods together, the 3-year monthly regional mean explains 88.65% of the variance in the O_3 data with an RMSE of 2.5729. When summed with the predicted devRM the explained variance increases to 93.50% with an RMSE of 1.9479.

Table 4.9 Summary and error statistics for Model B and Model C.

	Adj R^2	PRESS	RMSE
Model B	.2905	2036.2998	2.3596
Model C	.4204	1396.7001	1.9562

4.3 Surface Computation

Model C applied to the study area produces a 30 m resolution grid of estimated devRM. Results for NLCD2011 range from –14.8322 to 9.48497 ppb (Figure 4.7). To this surface may be added the regional mean computed for any day within the 2010–2012 period. Seasonality is captured in the regional mean which was removed and retained.

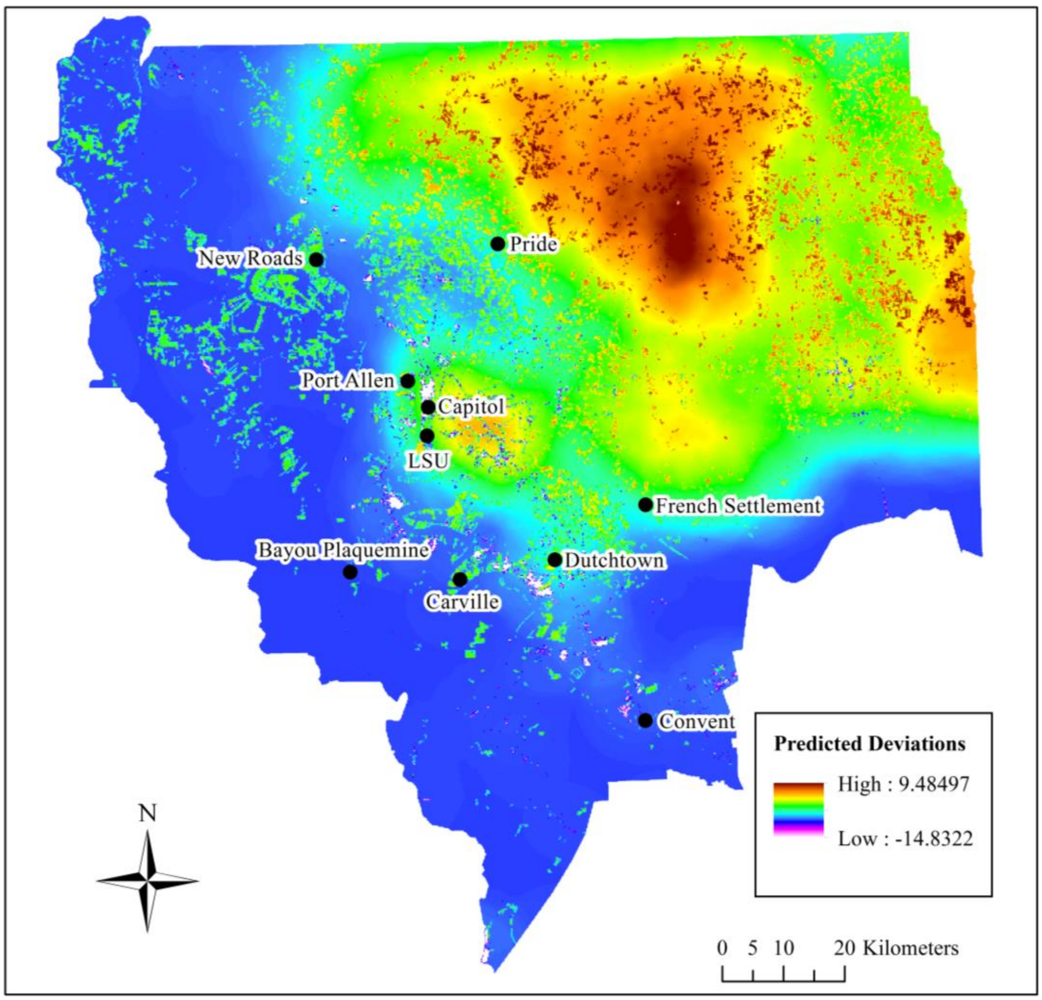

Figure 4.7 Prediction surface generated by Model C.

The regressed surface of devRM values differs from the surface interpolated with IDW (Figure 4.8). The regressed surface's cell resolution is 30 m. The ArcGIS spatial interpolation tool does provide the user the option to define the output cell size for the IDW surface, but the interpolation is limited by the extent of the input data. The default cell size is computed as the shorter of the width and height of the extent of the input features divided by 250. The extent of

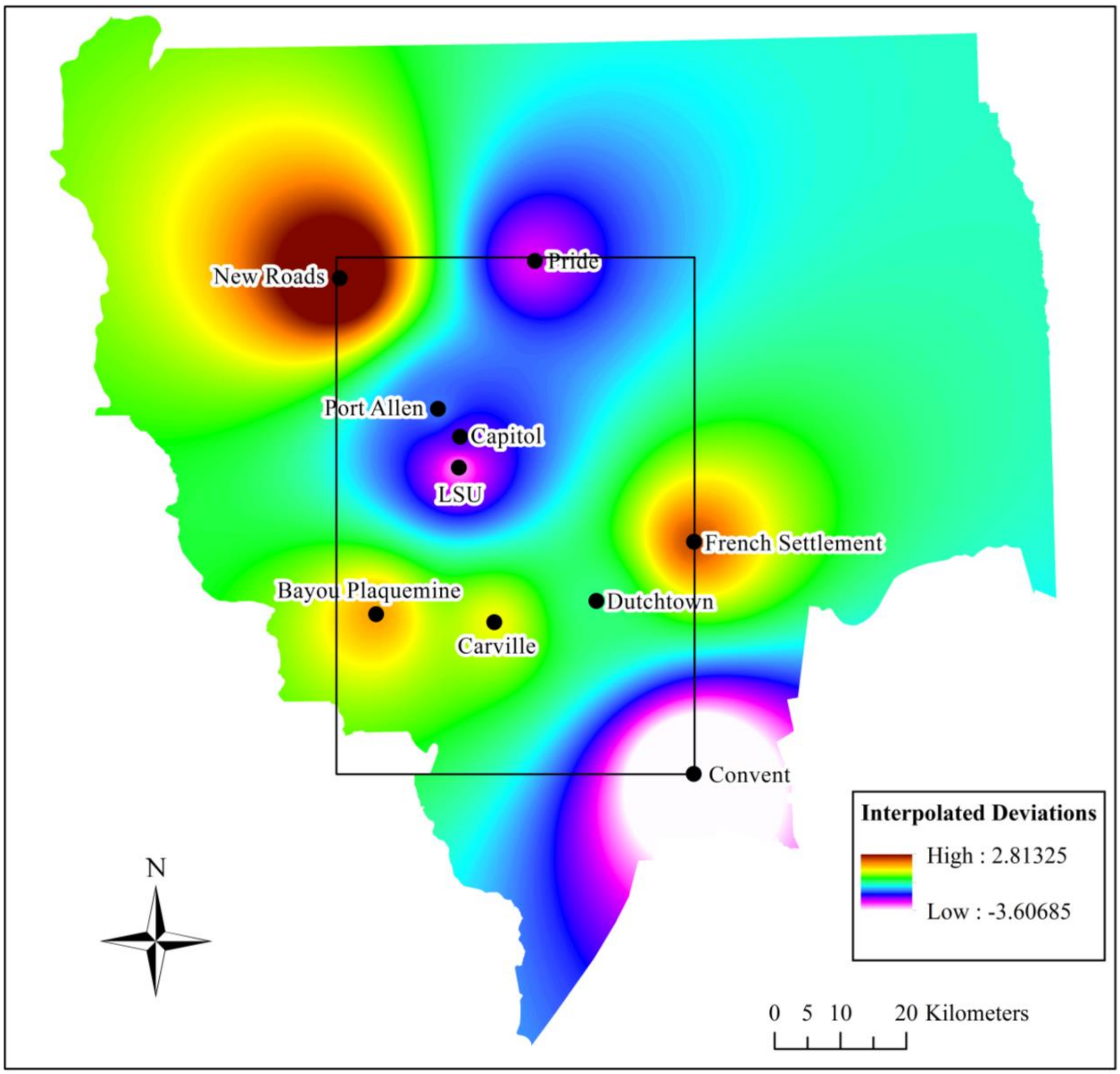

Figure 4.8 IDW interpolated surface.

the data points is delineated by a black box in Figure 4.8. Values outside of this box were extended using ArcGIS and are not interpolated values.

The detail of distribution of highs and lows differs between the two surfaces, and is perhaps the primary advantage of the regressed surface. With IDW, the range of the input determines the range of the output; ridges or valleys cannot be created if not captured in the sampled data. IDW can create bullseyes around data points due to the isotropic influence of an input point. For these reasons, the best results from IDW are obtained with dense sampling. IDW is used frequently despite its shortcomings because it does not make the explicit assumptions about statistical properties of the input data that more advanced interpolation methods do make.

The model was able to downscale the surface spatially, but how does it perform month-to-month? Model C was run on daily data by month and the components of variation graphed (Figure 4.9 and Figure 4.10). The ability of the model to predict the devRM was best in March and worst in August (Figure 4.9). Had the model performed perfectly, Adj R^2 would equal 1, or had it performed equivalently each month, the line would flat.

Clearly there are some temporal factors as play. Figure 4.10 compares the variance in the ppb captured by the regional mean to that of the regional mean summed with the predicted devRM. The greatest improvements in Adj R^2 are seen in the late fall through early spring. Very little improvement is seen in the spring and especially in the summer months. The LC model built on averages lends little to no improvement in these months possibly because the classified images failed to capture pertinent seasonal LC change, that meteorological conditions are a greater determinant of O_3 maxima than LC during these months, or there are important interaction terms to be included in future models.

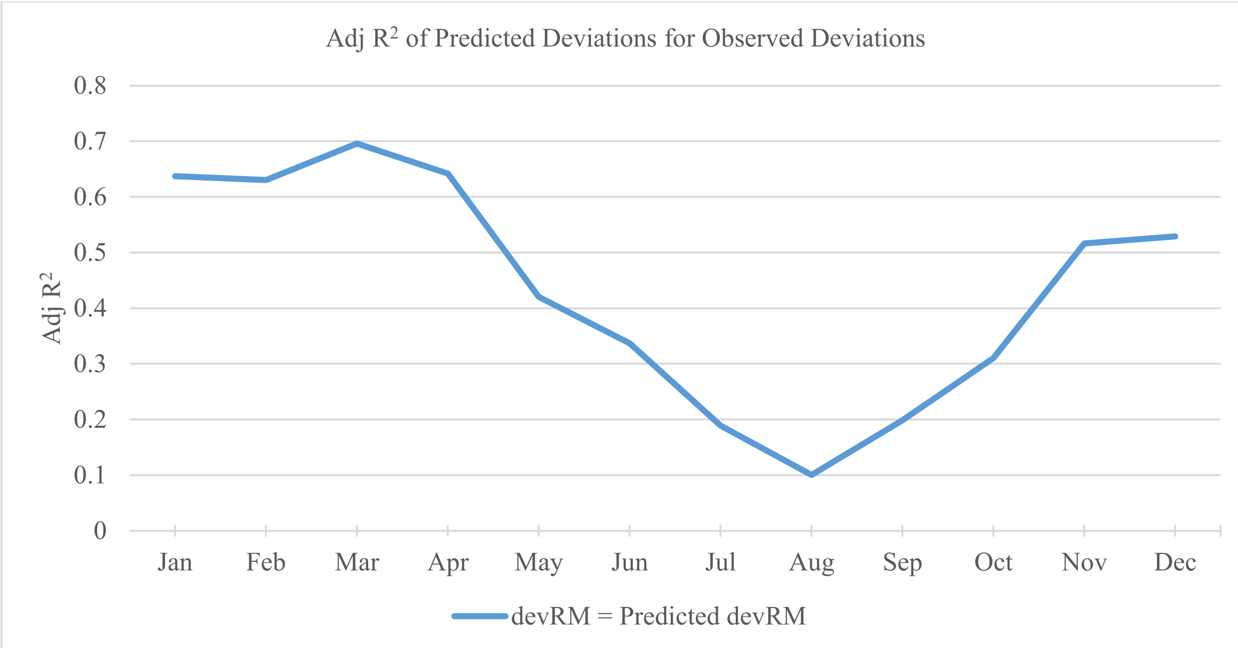

Figure 4.9 The performance of Model C run on daily data by month. Adj R^2 is that of the predicted devRM for the observed devRM. Had the model performed perfectly, Adj R^2 would equal 1, or had it performed equivalently each month, the line would flat.

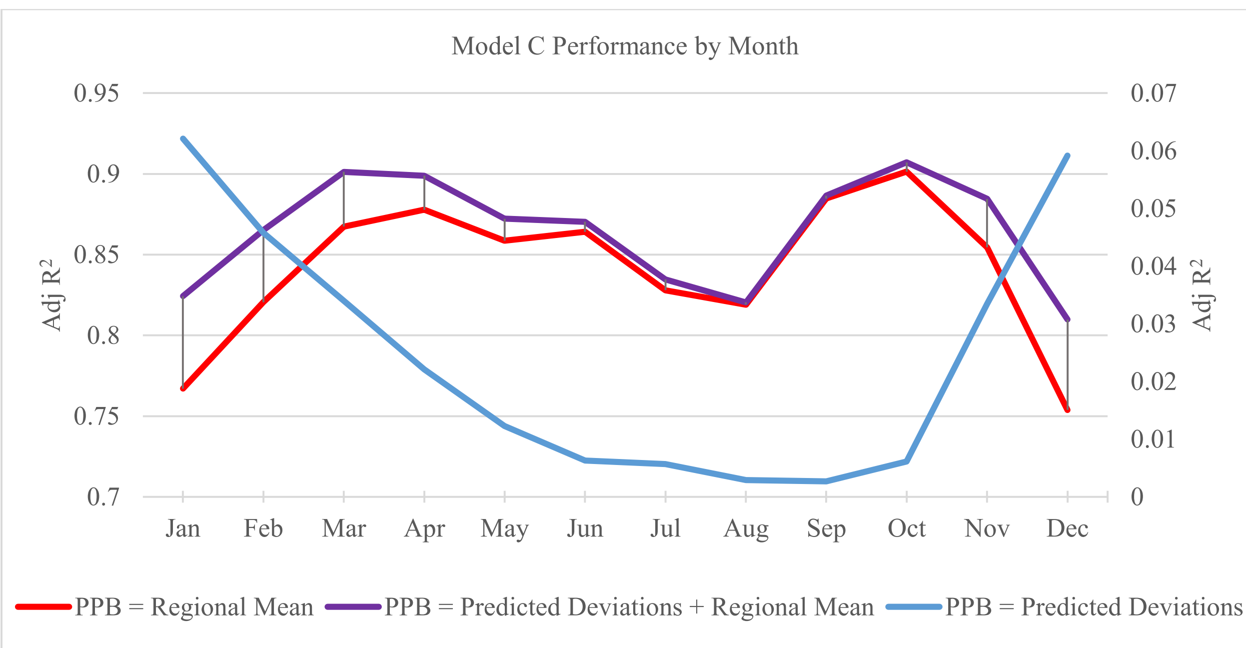

Figure 4.10 Adj R^2 for the regional mean, the predicted deviations, and the sum of the two by month.

Chapter 5. Discussion, Summary, and Conclusions

5.1 Correlation Analysis

Under the assumption that biogenic classes are sources of VOCs and that developed classes are sources of NO_x, the direction of effect observed in the correlation analysis could be explained by the VOC to NO_x ratio, and would fit the observation downtown-to-downwind evolution of an air mass from VOC-sensitivity to NO_x-sensitivity. The strength of correlations among the developed classes revealed by VIFs and correlation analysis, especially between LO and ME (Table 4.5), warrants further examination.

The MRLC (MRLC 2016) defines these classes as “areas with a mixture of constructed material and vegetation . . . These areas most commonly include single-family housing units.” For LO, impervious surfaces account for 20% to 49% of total cover. For ME, impervious surfaces account for 50% to79% of the total cover. For HI, impervious surfaces account for 80 to 100% of the total cover.

Continuous data would eliminate the conflict of these developed land classifications that are based on binned percentages. Beginning with NLCD 2001, the MRLC began producing two continuous datasets in addition to the classified dataset: one measuring the percentage of impervious surfaces and another for the percentage of canopy cover in each 30 m cell. So, developed land indicators will have more dimension (from 4 binned classifications to 1% intervals) by using the percentage of impervious surface raster, and a separate layer characterizing the canopy cover can be added to the analysis.

5.2 Model Performance

Model C accounts for 42.04% of the variance in the 3-year monthly mean devRM, which explains about 11.12% of the DO. In other words, Model C explains about 4.55% of the 3-year monthly mean DO. This suggests that if Model C could capture 100% of the devRM data then 11.12% of the DO would be explained by LC predictors. The regional mean explains 88.65% of the DO. Together, the regional mean and devRM predicted by Model C capture 93.50% of the data.

Model C was also applied to daily observations from 2000–2002, 2005–2007, and 2010–2012. Daily devRM explains 12.22% of the daily DO, and Model C captures 9.93% of the daily devRM, resulting in 1.20% of the daily DO explained by the daily devRM predicted by Model C. The daily regional mean accounts for 87.78% of the daily DO, and when summed with the predicted devRM, explains 88.89% of the daily DO.

Seasonal changes in the LC and the spread of observations in summer months may influence model performance throughout the years. A pitfall of the model is the assumption that LC is constant throughout a year. Obviously, agricultural fields are sometimes in production and sometimes in fallow; and deciduous trees are leaf-on in the summer and spring but leaf-off in the fall and winter. NLCD products do not reflect these changes. The amount of variance in the daily DO data explained by the predicted devRM ranges from 0.27% in September to 6.21% in January (Figure 4.9) Figure 4.10 compares the Adj R^2 for the regional mean, the predicted deviations, and the sum of the two. Models built by month and/or LC data that reflect seasonal changes are possible solutions.

5.3 Predicted Surface

Within the study area, there is an overall spatial trend of negative devRM in the southwest to positive devRM in the northeast, with the greatest negative devRM predicted in urbanized areas. Urban centers typically struggle with exceedances more than rural areas yet in this study the urban areas are predicted to have departures below the regional average (i.e. lower O_3 mixing ratios). The length of the averaging period could explain some of this incongruence between what might be expected based on historic exceedances and the predicted surface. O_3 events occur on the scale of hours and days, not months, and NO_x-loading events such as rush hour traffic may induce rapid O_3 production. Such small-scale variation gets "washed out" when averaged over a month.

On the boxplots in Figure 3.45 to Figure 3.62, the mean is denoted by a diamond and the median is a horizontal line inside a box representing the interquartile range (IQR). The greater the displacement of the mean from the median, the greater the skew. Extreme observations are marked with circles. Consistently, the LSU, Capitol, and Port Allen sites exhibit a large displacement of the mean from the median relative to the other sites and extreme observations above the upper fence, but these sites frequently have the lowest means. In the case of positive skew, extreme observations can pull the mean in the positive direction despite a majority of observations occurring are below the mean value. In a comparison of an urban traffic site, a semi-rural site, and a rural site, Im et al. (2013) observed greater fluctuations throughout the day at the urban site than at the rural site, but a greater monthly mean O_3 mixing ratios at the rural site.

Generally, the smaller statistical means at the LSU, Capitol, and Port Allen sites are maintained, and the IQR is smaller than other stations in the boxplots (Figure 3.45 to Figure 3.62) of the mean daily deviations showing the maxima relative to other stations. This indicates that on most days the maxima monitored by these sites deviates little from the regional mean maximum. This indicates nothing about the severity of extreme observations at the sites considered since on exceedance days the regional mean may be large and only a slight deviation would result in an exceedance. Conversely, large deviations might occur on days where the regional mean is low and thus not exceeding the design value.

5.4 Future Research

The results of this study are best interpreted as the likelihood of chronic exposure to elevated levels of O_3, levels that do not necessarily cause an exceedance. Negative deviations should not be considered a decrease in the O_3 in those areas, but that such areas, on average, experience daily O_3 maxima below that of the region. Predictions say nothing about the relative severity of daily mixing ratios at individual sites. The monthly results of this study could aid epidemiologists investigating health effects (asthma, birth-related, etc.) of long-term exposure.

Future attempts to model O_3 in the Baton Rouge area should include more layers of data, particularly with more temporal resolution and data on land use as well as LC. Synoptic-scale meteorology is captured in the regional mean, but local wind conditions may provide insight on the transport of precursors. Light winds in the Baton Rouge area (NOAA 2011) cause drift rather than dispersion. Winds blowing over NO_x saturated urbanized areas may carry precursors into rural regions that may be rich in VOCs. Traffic patterns could characterize the time of expected NO_x loadings as well as the geography of emissions.

This study focused only on LC and did not account for land use. LC may be able to capture some latent variable related to surface thermal properties, dispersion, and emissions. Land use may be better at characterizing the geography of precursor emissions. For example, a point source such as a petrochemical plant surrounded by agricultural land or forests would not be captured by LC. Due to the resolution of the raster, roadways may not be captured, and for those that are, there is no indication of how much the roadways are trafficked. An interstate corridor is more intensely used than a rural road. Many studies use either roadway classifications or vehicle miles traveled (VMT) as model inputs.

Using auxiliary information in interpolating phenomena helps refine the spatial resolution. Localized spatial character was emphasized but detrending the point-based observations of the regional mean. LC data did not perform well in predicting the daily maximum O_3 but performed moderately well for longer averaging periods. For monthly mean maximum, evergreen and developed classes were important predictors. Evergreen has a positive relationship while developed classes have negative relationships with the devRM. Given the strength of correlations and the importance of these variables in regression, NCLD products containing the percentage of impervious surface and percentage of canopy cover per pixel should be evaluated as potential predictors.

More robust verification of results is desirable, as is the evaluation of the model performance at different sites and by season. The study could be expanded with data from similar climate regions, and the stability of the model tested with data from those regions. Independent sampling at locations between monitoring sites would improve validation statistics. While meteorology was not considered in this study, meteorological conditions at the time that daily O_3 maxima were reached could be evaluated and potentially incorporated as model parameters. Despite the limitations of this study, it serves as a useful first step in the next part of the process of protecting life and property from the hazards of long-term exposure to O_3 – the process of spatially predicting the measured data.

References

Abraham, J. S. & A. C. Comrie (2004) Real-time ozone mapping using a regression-interpolation hybrid approach, applied to Tucson, Arizona. Journal of the Air and Waste Management Association, 54, 914–925.

Aguilera, I., M. Pedersen, R. Garcia-Esteban, F. Ballester, M. Basterrechea, A. Esplugues, A. Fernandez-Somoano, A. Lertxundi, A. Tardon & J. Sunyer (2013) Early-life exposure to outdoor air pollution and respiratory health, ear infections, and eczema in infants from the INMA study. Environmental Health Perspectives, 121, 387–392.

Ahmed, S. & G. De Marsily (1987) Comparison of geostatistical methods for estimating transmissivity using data on transmissivity and specific capacity. Water Resources Research, 23, 1717– 1737.

Alsamamra, H., J. A. Ruiz-Arias, D. Pozo-Vázquez & J. Tovar-Pescador (2009) A comparative study of ordinary and residual kriging techniques for mapping global solar radiation over southern Spain. Agricultural and Forest Meteorology, 149, 1343–1357.

Avnery, S., D. L. Mauzerall, J. Liu & L. W. Horowitz (2011) Global crop yield reductions due to surface ozone exposure: 1. Year 2000 crop production losses and economic damage. Atmospheric Environment, 45, 2284–2296.

Beckett, W. S. (1991) Ozone, air pollution, and respiratory health. The Yale Journal of Biology and Medicine, 64, 167–175.

Beelen, R., G. Hoek, P. Fischer, P. A. van den Brandt & B. Brunekreef (2007) Estimated long-term outdoor air pollution concentrations in a cohort study. Atmospheric Environment, 41, 1343–1358.

Beelen, R., G. Hoek, D. Vienneau, M. Eeftens, D. K., X. Pedeli, M.-Y. Tsai, N. Kunzli, T. Schikowski, A. Marcon, K. T. Eriksen, O. Raaschou-Nielsen, E. Stephanou, E. Patelarou, T. Lanki, T. Yli-Tuomi, C. Declercq, G. Falq, M. Stempfelet, M. Birk, J. Cyrys, S. von Klot, G. Nador, M. J. Varro, A. Dedele, R. Grazuleviciene, A. Molter, S. Lindley, C. Madsen, G. Cesaroni, A. Ranzi, C. Badaloni, B. Hoffmann, M. Nonnemacher, U. Kramer, T. Kuhlbusch, M. Cirach, A. de Nazelle, M. Nieuwenhuijsen, T. Bellander, M. Korek, D. Olsson, M. Stromgren, E. Dons, M. Jerrett, P. Fischer, M. Wang, B. Brunekreef & K. de Hoogh (2013) Development of NO_2 and NO_x land use regression models for estimating air pollution exposure in 36 study areas in Europe -- The ESCAPE Project. Atmospheric Environment, 72, 10–23.

Briggs, D. J., S. Collins, P. Elliott, P. Fischer, S. Kingham, E. Lebret, K. Pryl, H. Van Reeuwijk, K. Smallbone & A. Van Der Veen (1997) Mapping urban air pollution using GIS: a regression-based approach. International Journal of Geographical Information Science, 11, 699–718.

Briggs, D. J., C. de Hoogh, J. Gulliver, J. Wills, P. Elliott, S. Kingham & K. Smallbone (2000) A regression-based method for mapping traffic-related air pollution: application and testing in four contrasting urban environments. Science of the Total Environment, 253, 151–167.

Currie, J., E. A. Hanushek, E. M. Kahn, M. Neidell & S. G. Rivkin (2009) Does pollution increase school absences? The Review of Economics and Statistics, 91, 682–694.

Feng, Z., J. Sun, W. Wan, E. Hu & V. Calatayud (2014) Evidence of widespread ozone-induced visible injury on plants in Beijing, China. Environmental Pollution, 193, 296–301.

Fotheringham, A. S. & C. Brunsdon (1999) Local forms of spatial analysis. Geographical Analysis, 31, 340–358.

Fry, J., G. Xian, S. Jin, J. Dewitz, C. Homer, L. Yang, C. Barnes, N. Herold & J. Wickham (2011) Completion of the 2006 National Land Cover Database for the conterminous United States. Photogrammetric Engineering & Remote Sensing , 77, 858–864.

Fuhrer, J., L. Skärby & M. R. Ashmore (1997) Critical levels for ozone effects on vegetation in Europe. Environmental Pollution, 97, 91–106.

Gilbert, N. L., M. S. Goldberg, B. Beckerman, J. R. Brook & M. Jerrett (2005) Assessing spatial variability of ambient nitrogen dioxide in Montreal, Canada, with a land-use regression model. Journal of the Air & Waste Management Association, 55, 1059–1063.

Gilliland, F. D., K. Berhane, E. B. Rappaport, D. C. Thomas, E. Avol, W. J. Gauderman, S. J. London, H. G. Margolis, R. McConnell, K. T. Islam & J. M. Peters (2001) The effects of ambient air pollution on school absenteeism due to respiratory illnesses. Epidemiology, 12, 43–54.

Goovaerts, P. (1997). Geostatistics for Natural Resources Evaluation. New York: Oxford University Press, 1997.

Goovaerts, P. (1999) Using elevation to aid the geostatistical mapping of rainfall erosivity. Catena, 34, 227–242.

Guenther, A. (1997). Seasonal and spatial variations in natural volatile organic compound emissions. Ecological Society of America, 7, 34–45.

Gulliver, J., K. de Hoogh, D. Fecht, D. Vienneau & D. J. Briggs (2011) Comparative assessment of GIS-based methods and metrics for estimating long-term exposures to air pollution. Atmospheric Environment, 45, 7072–7080.

Hall, J. V., V. Brajer & F. W. Lurmann (2003) Economic valuation of ozone-related school absences in the South Coast Air Basin of California. Contemporary Economic Policy, 21, 407–417.

Henderson, S. B., B. Beckerman, M. Jerrett & M. Brauer (2007) Application of land use regression to estimate long-term concentrations of traffic-related nitrogen oxides and fine particulate matter. Environmental Science &Technology, 41, 2422–2428.

Hengl, T., G. B. M. Heuvelink & D. G. Rossiter (2007) About regression-kriging: From equations to case studies. Computers & Geosciences, 33, 1301–1315.

Hengl, T., G. B. M. Heuvelink & A. Stein (2003) Comparison of kriging with external drift and regression-kriging. Technical note, ITC, 51.

Hoek, G., R. Beelen, K. De Hoogh, D. Vienneau, J. Gulliver, P. Fischer & D. J. Briggs (2008) A review of land-use regression models to assess spatial variation of outdoor air pollution. Atmospheric Environment, 42, 7561–7578.

Homer, C., J. Dewitz, J. Fry, M. Coan, N. Hossain, C. Larson, N. Herold, A. McKerrow, J. N. VanDriel & J. Wickham (2007) Completion of the 2001 National Land Cover Database for the conterminous United States. Photogrammetric Engineering and Remote Sensing, 73, 337–341.

Homer, C. G., J. A. Dewitz, L. Yang, S. Jin, P. Danielson, G. Xian, J. Coulston, N. D. Herold, J. D. Wickham & K. Megown (2015) Completion of the 2011 National Land Cover Database for the conterminous United States-Representing a decade of land cover change information. Photogrammetric Engineering and Remote Sensing, 81, 345–354.

Im, U., S. Incecik, M. Guler, A. Tek, S. Topcu, Y. S. Unal, O. Yenigun, T. Kindap, M. T. Odman & M. Tayanc (2013) Analysis of surface ozone and nitrogen oxides at urban, semi-rural and rural sites in Istanbul, Turkey. Science of the Total Environment, 443, 920–931.

Isebrands, J. G., A. B. Guenther, P. Harley, D. Helmig, L. Klinger, L. Vierling, P. Zimmerman & C. Geron (1999) Volatile organic compound emission rates from mixed deciduous and coniferous forests in northern Wisconsin, USA. Atmospheric Environment, 33, 2527–2536.

Jerrett, M., M. A. Arain, P. Kanaroglou, B. Beckerman, D. Crouse, N. L. Gilbert, J. R. Brook, N. Finkelstein & M. M. Finkelstein (2007) Modeling the intraurban variability of ambient traffic pollution in Toronto, Canada. Journal of Toxicology and Environmental Health. Part A, 70, 200–212.

Jerrett, M., M. A. Arain, P. Kanaroglou, B. Beckerman, D. Potoglou, T. Sahsuvaroglu, J. Morrison & C. Giovis (2005) A review and evaluation of intraurban air pollution exposure models. Journal of Exposure Analysis & Environmental Epidemiology, 15, 185–204.

Kanaroglou, P. S., M. Jerrett, J. Morrison, B. Beckerman, M. A. Arain, N. L. Gilbert & J. R. Brook (2005) Establishing an air pollution monitoring network for intra-urban population exposure assessment: A location-allocation approach. Atmospheric Environment, 39, 2399–2409.

Kaplan, G. G., D. Tanyingoh, E. Dixon, M. Johnson, A. J. Wheeler, R. P. Myers, S. Bertazzon, V. Saini, K. Madsen, S. Ghosh & P. J. Villeneuve (2013) Ambient ozone concentrations and the risk of perforated and nonperforated appendicitis: A multicity case-crossover study. Environmental Health Perspectives, 939–943.

Knotters, M., D. J. Brus & J. H. Oude Voshaar (1995) A comparison of kriging, co-kriging and kriging combined with regression for spatial interpolation of horizon depth with censored observations. Geoderma, 67, 227–246.

Krupa, S. V. & W. J. Manning (1988) Atmospheric ozone: Formation and effects on vegetation. Environmental Pollution, 50, 101–137.

Lee, H., E. K. Kim, S. W. Kang, J. H. Kim, H. J. Hwang & T.-i. Kim (2013) Effects of ozone exposure on the ocular surface. Free Radical Biology and Medicine, 63, 78–89.

Lei, H., D. J. Wuebbles & X.-Z. Liang (2012) Projected risk of high ozone episodes in 2050. Atmospheric Environment, 59, 567–577.

Li, J. & A. D. Heap (2011) A review of comparative studies of spatial interpolation methods in environmental sciences: Performance and impact factors. Ecological Informatics, 6, 228–241.

Moore, D. K., M. Jerrett, W. J. Mack & N. Kunzli (2007) A land use regression model for predicting ambient fine particulate matter across Los Angeles, CA. Journal of Environmental Monitoring, 9, 246–252.

Morgenstern, V., A. Zutavern, J. Cyrys, I. Brockow, U. Gehring, S. Koletzko, C. P. Bauer, D. Reinhardt, H. E. Wichmann & J. Heinrich (2007) Respiratory health and individual estimated exposure to traffic-related air pollutants in a cohort of young children. Occupational and Environmental Medicine, 64, 8–16.

MRLC (2016) *National Land Cover Database: Product Legend*. http://www.mrlc.gov/nlcd11_leg.php. (last accessed 20 May 2016).

National Emissions Inventory. 2011. Air Emissions Inventory. https://www.epa.gov/air-emissions-inventories. (last accessed 2 April 2016).

NOAA/ National Climatic Data Center (2011) Local climatological data annual summary with comparative data: Baton Rouge, Louisiana (KBTR).

Perara, E. M. & T. Sanford (2011) Climate change and your health: Rising temperatures, worsening ozone pollution. Union of Concerned Scientists.

Romieu, I., M. C. Lugo, S. R. Velasco, S. Sanchez, F. Meneses & M. Hernandez (1992) Air pollution and school absenteeism among children in Mexico City. American Journal of Epidemiology, 136, 1524–1531.

Rosenlund, M., F. Forastiere, M. Stafoggia, D. Porta, M. Perucci, A. Ranzi, F. Nussio & C. A. Perucci (2008) Comparison of regression models with land-use and emissions data to predict the spatial distribution of traffic-related air pollution in Rome. Journal of Exposure Science & Environmental Epidemiology, 18, 192–199.

Ross, Z., M. Jerrett, K. Ito, B. Tempalski & G. D. Thurston (2007) A land use regression for predicting fine particulate matter concentrations in the New York City region. Atmospheric Environment, 41, 2255–2269.

Sahsuvaroglu, T., M. A. Arain, P. Kanaroglou, N. Finkelstein, B. Newbold, M. Jerrett, B. Beckerman, J. R. Brook, M. Finkelstein & N. L. Gilbert (2006) A land use regression model for predicting ambient concentrations of nitrogen dioxide in Hamilton, Ontario, Canada. Journal of the Air & Waste Management Association, 56, 1059–1069.

Shaker, R. R., A. I. Crăciun & I. Grădinaru (2010) Relating land cover and urban patterns to aquatic ecological integrity: A spatial analysis. Geographia Technica, 9, 76–90.

Sillman, S. (1999) The relation between ozone, NO_x and hydrocarbons in urban and polluted rural environments. Atmospheric Environment, 33, 1821–1845.

Staudt, M. & J. Kesselmeier (1999) Biogenic volatile organic compounds (VOC): an overview on emission, physiology and ecology. Journal of Atmospheric Chemistry, 33, 23–88.

Tobler, W. R. (1970) A computer movie simulating urban growth in the Detroit region. Economic Geography, 234–240.

United States Census Bureau.(2010) http://www.census.gov/quickfacts/table/PST045215/00. (last accessed 2 April 2016).

United States Environmental Protection Agency.(2013) Integrated Science Assessment of Ozone and Related Photochemical Oxidants. Washington, DC: U.S. Environmental Protection Agency.

Wagner, P. & W. Kuttler (2014) Biogenic and anthropogenic isoprene in the near-surface urban atmosphere — A case study in Essen, Germany. Science of the Total Environment, 475, 104–115.

Wang, W., Y. Ying, Q. Wu, H. Zhang, D. Ma & W. Xiao (2015) A GIS-based spatial correlation analysis for ambient air pollution and AECOPD hospitalizations in Jinan, China. Respiratory Medicine, 109, 372–378.

Zainodin, H. J. & S. J. Yap (2013) Overcoming multicollinearity in multiple regression using correlation coefficient. AIP Conference Proceedings, 1557, 416–419.

Zivin, J. & M. Neidell (2013) Environment, health, and human capital. Journal of Economic Literature, 51, 689–730.

Zou, X. & Y. Wu (2005) On the relationship between Total Ozone Mapping Spectrometer (TOMS) ozone and hurricanes. Journal of Geophysical Research- Atmospheres, 110, 1–15.

Vita

Mallory Nance Thomas, a native of Sunset, Louisiana, received her Bachelor of Science degree at Louisiana State University in 2013. Eager to conduct research, she entered graduate school in the Department of Geography and Anthropology at Louisiana State University under the direction of Dr. Robert Rohli. She is a candidate to receive her master's degree in August 2016 and hopes for a career in conservation upon graduation.